THE INVESTIGATION OF THE STATIC AND DYNAMIC CRUSHING BEHAVIOR OF AN ENERGY ABSORBING BIOMIMETIC ARMOR

A Thesis Submitted to
The Graduate School of Engineering and Sciences of
İzmir Institute of Technology
in Partial Fulfillment of the Requirements for the Degree of

MASTER OF SCIENCE

in Mechanical Engineering

by
Emine Fulya AKBULUT

July 2017
İZMİR

We approve the thesis of **Emine Fulya AKBULUT**

Examining Committee Members:

Prof. Dr. Alper TAŞDEMİRCİ
Department of Mechanical Engineering, İzmir Institute of Technology

Assoc. Prof. Dr. H. Seçil ARTEM
Department of Mechanical Engineering, İzmir Institute of Technology

Prof. Dr. Buket OKUTAN BABA
Department of Mechanical Engineering, İzmir Katip Çelebi University

21 July 2017

Prof. Dr. Alper TAŞDEMİRCİ
Supervisor, Department of
Mechanical Engineering
İzmir Institute of Technology

Prof. Dr. Mustafa GÜDEN
Co-Supervisor, Department of
Mechanical Engineering
İzmir Institute of Technology

Prof. Dr. Metin TANOĞLU
Head of the Department of
Mechanical Engineering

Prof. Dr. Aysun SOFUOĞLU
Dean of the Graduate School of
Engineering and Sciences

ACKNOWLEDGEMENTS

I would first like to convey my appreciativeness to my advisor Prof. Dr. Alper TAŞDEMİRCİ for his excellent recommendations, generous support, deepest patience, brilliant ideas and guidance throughout the study. Furthermore, this dissertation cannot be completed without his great contributions. I also express my gratefulness to him for changing my career expectation by expanding my vision and providing me with valuable facilities of his research team in Dynamic Testing and Modelling Laboratory.

I also sincerely thank my co-advisor and the rector of Izmir Institute of Technology Prof. Dr. Mustafa GÜDEN for his endless encouragement and contributions to my education.

The Scientific and Technological Research Council of Turkey (TÜBİTAK) deserves obeisance for subsidizing the 214M339 project. Thanks to my entire project mate, Erkan GÜZEL and Fırat TÜZGEL who played a magnificent role in the current study.

I gratefully thank my research team mate Çetin Erkam UYSAL, Semih Berk SEVEN, Mehmet Alper ÇANKAYA, Mustafa Kemal SARIKAYA, Selim ŞAHİN, Atacan YÜCESOY, Ali Kıvanç TURAN, Ali KARA and İsmet Kutlay ODACI for their willingness to help and unceasing friendliness.

My thanks and gratefulness go to my best friend Övül KÖSEOĞLU who always help and keep in touch with me no matter how busy she is.

Especially, I am thankful for my boyfriend, Hayrettin IRMAK, for his endless love during my master, his never-ending steadfastness against my stress and his effort for encouraging me to be even better.

Above all, I am grateful to my father, Ali, who has given me everlasting support without a doubt for following my dreams, to my mother, Münevver, for her love, prays and the perfect wishes of the world on my career, and to my sister, Feride Ferya, for her splendid promotive attitudes in my life.

ABSTRACT

THE INVESTIGATION OF THE STATIC AND DYNAMIC CRUSHING BEHAVIOR OF AN ENERGY ABSORBING BIOMIMETIC ARMOR

In this study, an innovative thin-walled energy absorbing structure was manufactured following by biomimicry rules and produced from AISI 304L stainless steel sheet material by deep drawing method. Manufacturing process was modelled in two stages to produce the numerical specimen containing residual stress/strain and thickness distribution using commercial software LS-DYNA. The balanus being a sea creature, consisting of an inner core structure and an outer shell structure, is the inspiration of this study. The balanus was compared to the other conventional geometries in terms of the energy absorption capacity and determined as highly advantageous configuration. Quasi-static crushing and drop weight experiments were conducted and modelled numerically. The observations indicated that the carried load by the balanus is greater than the arithmetic total of the carried load by the inner core and the outer shell separately due to the interaction effect. Besides, energy absorbing performance of the balanus improved under dynamic loading since the outer shell confines the inner core during the deformation and developed the energy absorption performance of it while the energy absorbing capacity of the other two decreased. After the end of the experimental studies, the energy absorption partitions between the components of the balanus were studied numerically and it was observed that the energy absorbing capacity of the balanus increases with increasing deformation velocity due to the strain rate sensitivity effect of the material and the differences of energy partition ratio between the two components decreases.

ÖZET

BİYOBENZETİM TABANLI ENERJİ YUTUCU BİR ZIRHIN STATİK VE DİNAMİK EZİLME DAVRANIŞININ İNCELENMESİ

Bu çalışmada, biyomimikri ile özgün ince cidarlı bir enerji absorbe edici bir yapı tasarlanmış ve derin çekme yöntemiyle AISI 304L paslanmaz çelik sac malzemeden imal edilmiştir. Üretim prosesi ticari yazılım LS-DYNA kullanılarak artık stres/gerinim ve kalınlık dağılımı içeren nümerik numuneleri üretmek üzere iki aşamalı olarak modellendi. Bir iç çekirdek yapı ve bir dış kabuk yapıdan oluşan bir deniz canlısı olan balanus, bu çalışmanın ilham kayağıdır. Balanus, enerji absorbe etme kapasitesi açısından diğer konvansiyonel geometrilerle karşılaştırıldı ve oldukça avantajlı bir konfigürasyon olarak tanımlandı. Kuasi-statik ezilme ve düşen ağırlık deneyleri yapıldı ve nümerik olarak modellendi. Gözlemler balanus tarafından taşınan yükün etkileşim etkisi nedeniyle iç çekirdeğin ve dış kabuğun ayrı ayrı taşıdığı yükün aritmetik toplamından daha yüksek olduğunu gösterdi. Ayrıca balanın enerji absorbe etme performansı, diğer ikisinin enerji emme performansı bireysel olarak azalırken dış kabuk iç çekirdeği deformasyon sırasında sınırlandırdığı ve onun enerji absorbe etme performansını geliştirdiği için dinamik yük altında arttı. Deneysel çalışmaların bitmesinin ardından balanın bileşenleri arasındaki enerji emme paylaşımları nümerik olarak incelendi ve malzemenin şekil değiştirme oranı hassasiyet etkisi nedeniyle deformasyon hızının artmasıyla balanın enerji emme kapasitesinin arttığı ve iki bileşen arasındaki enerji paylaşım oranı farklarının azaldığı gözlemlendi.

TABLE OF CONTENTS

LIST OF FIGURES

Figure **Page**

LIST OF TABLES

Tables **Page**

CHAPTER 1

INTRODUCTION

1.1 Energy Absorbing Structures

The utilization of energy absorbing structures in such industries where a collision may cause grave consequences to humans and vehicles started to attract the attention of countries all around the world. The principles of designing of an optimal energy absorbing structure and selection of proper materials depend on a particular purpose and terms which they are to work. To illustrate, vehicles of defense industry are equipped with high-quality steel armor to protect occupants from the attack. When long distance duties were considered, lightweight armor designs have an advantage over the mobility of the vehicles. Moreover, an increase in weight indicates more consumption of fuel. Hence, the excellent armor design as a high energy absorbing structure is significant for both civil and military applications due to the mentioned reasons above. Although the proper design and selection of material can vary from one implementation to another, the main aim in all cases is to dissipate kinetic energy by using a maximally deformable material to absorb energy at a prespecified rate. To understand of energy absorption of structures is important in a view to determine the damage which is known as a process of irreversible phase transition from initial kinetic energy to damaged state by plastic deformation. When the converting initial kinetic energy to elastic strain energy of the structures is completed, elastic deformation is reached its maximum level. In the event of crushing, this elastic strain energy is released and lead damage to the person to be protected. After this phase transition is determined, required structural parameters are specified. These structural parameters are the shape of protective construction and the choice of materials. Composite and metals with a special absorbing filler material are widely used in lightweight armor design. In contrast to metallic materials, composite materials are stiff materials with low density. When it comes to energy absorption, cellular materials consisting of formed cells such as honeycomb and corrugated structural types have particular interest in many materials.

There are many energy absorbing structures used in the event of crushing. However, the thin-walled structure is a commonly used type due to its superior crashworthiness. Energy absorption characterizations of thin-walled structures depend on the structure geometries, its material properties and the load the material are exposed to. There are numerous studies conducted on thin-walled structures in literature since the using same material in different geometries causes the different energy absorption capacity. The well-known conventional thin-walled geometries are square, cylinder, hexagonal, conical and spherical ones. Thickness distribution is another factor which influences the deformation history significantly. The crushing histories and modes of deformation are a function of their geometrical properties such as cone angle, height, wall thickness and radius. Thanks to desirable crashworthiness of the conventional thin-walled core geometries, sandwich structures mostly used as energy absorber armor in defense and automotive industry.

In order to avoid damage and injury by dissipating the energy during an accident both absorbed energy and mean crushing force values are essential magnitudes. The axial loading of the cylinder was investigated as an energy absorber in the 1960s (Alexander, 1960). In another study, box columns and cylindrical tubes were examined under quasi-static and dynamic loadings experimentally and theoretically to determine the crushing behavior of the structures. Furthermore, the progressive folding of thin-walled structures was described as structural response of the crushing process for energy absorbing (A. Abramowicz & Wierzbicki, 1983). An experimental study was conducted so as to determine the axial crushing behavior of steel square tubes under quasi-static loading. The observations showed that specimens absorbed more energy with further plastic deformation based on the fold formation (DiPaolo & Tom, 2006).

Nia and Parsapour conducted a comparative study in terms of energy absorbing capacity of simple and multi-cell thin-walled tubes, Figure 1.1. The specimens were manufactured using aluminum material having triangular, square, hexagonal and octagonal cross-sections. The energy absorption efficiencies of these structures were investigated under quasi-static loads both experimentally and numerically. An increase in the absorbed energy was observed with the use of multi-cell tubes rather than simple section tubes. The results also showed that hexagonal and octagonal sections among all multi-cell section thin-walled tubes were the most efficient configurations in terms of energy absorbing per unit of mass. Moreover, the first type of multi-cell with inner

blades attached from the midpoint of the edges were the more efficient than the second type of multi-cell with inner blades attached from the corners (Nia & Parsapour, 2014).

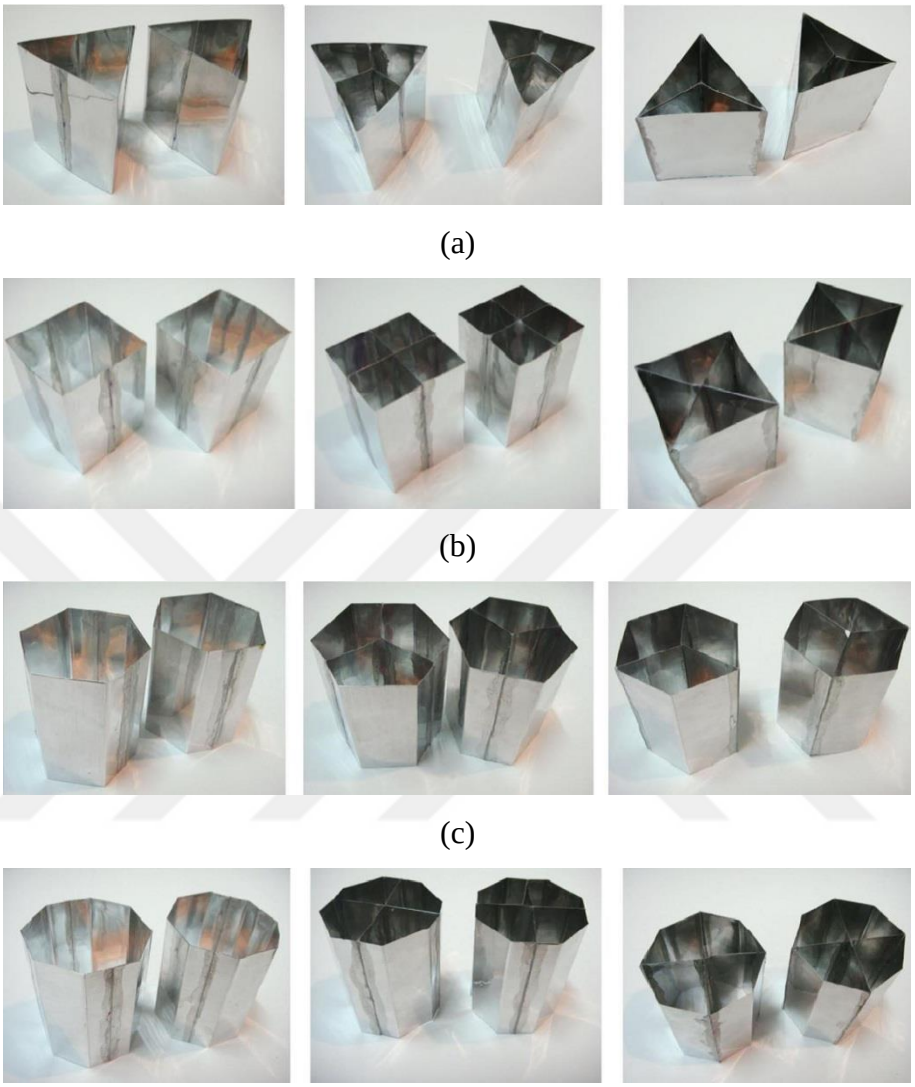

(a)

(b)

(c)

(d)

Figure 1.1. Produced simple section, the first type multi-section specimens and the second type multi-section specimens; (a) triangle, (b) square, (c) hexagonal and (d) octagonal (Source: Nia & Parsapour, 2014).

Several authors investigated axial crushing behaviors of thin-walled tubes with various cross-sections. However, the interest of some scientists tended to polyurethane foam filled tubes to research the performances of the energy absorbing. Thus, rectangular and square tubes were produced from steel material having different thickness in a study and experiments were conducted under both quasi-static and dynamic loads. Specimens were tested as empty and polyurethane foam-filled. When

the experimental results were considered, it was found that foam filled tubes absorbed more energy than empty tubes not only because of its strength but also an interaction between the foam material and the specimen surface during crushing. Additionally, specific absorbed energy capacities of polyurethane foam filled materials found much more than empty ones. It was observed at the end of the study that foam filled materials can be preferable to increasing the wall thickness so as to improve the energy absorption capacity of tubes (Reid, Reddy, & Gray, 1986). Besides, Abramowicz and Wierzbicki reported that the interaction between the sheet metal tubes and the polyurethane foam material caused increasing of energy absorption capacity of the column while the interaction resulted in a distinct crushing mode (W. Abramowicz & Wierzbicki, 1988). Zarei and Kröger performed a study on foam filled aluminum square tubes for crush boxes in vehicles in order to find more efficient, lighter and having a high energy absorbing capacity design. Their results showed that foam filled crush boxes absorbed high amount of energy with minimum weight due to the interaction between foam materials and tube surfaces. Moreover, energy absorption increased remarkably when foam density increased. However, they also pointed out that specific absorbed energy must be considered when lightweight materials should be used (Zarei & Kröger, 2008). Furthermore, the interaction between foam material and tube surface and resulting high energy absorbing capacity inspired Goel and he investigated the energy absorbing efficiency of the single, double and multi-wall square and circular cross-sectional tubes as foam-filled and empty. Results showed that all foam filled both square and cylinder tubes reached the maximum energy absorption capacity. Moreover, the circular cross-sectional tubes were much more efficient design as energy absorber than the square cross-sectional tubes (Goel, 2015).

The use of composite materials started to come to the forefront in many fields due to their high stiffness/weight ratio (Mamalis et al., 1997). As a part of engineering applications, composite materials started to replace metal as energy absorbing structures. Due to this, extensive studies were conducted in the literature. Especially, geometrical design of composite materials was investigated in detailed since it influenced the specific absorbed energy significantly. The main investigated geometries are the square tubes (Mamalis, Manolakos, Ioannidis, & Papapostolou, 2004, 2005, 2006), cylindrical tubes (Abosbaia, Mahdi, Hamouda, & Sahari, 2003), (Abosbaia, Mahdi, Hamouda, Sahari, & Mokhtar, 2005), (Li, 2006), (T. Hou, Pearce, Prusty, Kelly,

& Thomson, 2015), (Reuter, Sauerland, & Tröster, 2017), conical tubes (Kathiresan, Manisekar, & Manikandan, 2012), (Kathiresan, Manisekar, & Manikandan, 2014), (Kathiresan & Manisekar, 2016) and elliptical tubes (Alkateb, Mahdi, Hamouda, & Hamdan, 2004), (E. S. Mahdi & El Kadi, 2008). However, both experimental and numerical approaches of the crushing behavior of several types of composite structures were not limited with the widely used geometries. Some geometries were performed comparatively under different loadings in terms of energy absorbing capacity in the literature such as hexagonal tubes, hourglass type tubes, radial corrugated tubes, radial corrugated surrounded by circular tubes, cone-tube-cone systems (E. Mahdi, Hamouda, Sahari, & Khalid, 2003), (Abdewi, Sulaiman, Hamouda, & Mahdi, 2006), (Abdewi, Sulaiman, Hamouda, & Mahdi, 2008), (Palanivelu et al., 2011), (Lau, Said, & Yaakob, 2012), (Milan, Viktor, Sergii, & Vít, 2014). Besides, metal/composite hybrid structures are among the most interesting subjects as thin-walled structures to supply requirements of both lightweight structures and crashworthiness and were investigated as energy absorbers in many fields. (Babbage & Mallick, 2005), (Li, 2007), (Guden, Yüksel, Tasdemirci, & Tanoğlu, 2007), (Zhu, Sun, Liu, Li, & Li, 2017). The energy absorption capability and crushing mode of composite tubes depend on not the only shape of specimens but also they can be influenced by the type of fiber and matrix, wall thickness, ply orientation, loading conditions and technology of production. Among all these factors, the ply orientation and wall thickness influence significantly energy absorbing capacity. In literature, this was reported that the selecting proper ply orientation and wall thickness can result in enhancement of energy absorption performance of the structure (Parvin & Jamwal, 2005), (Li, Maricherla, Singh, Pang, & John, 2006), (Wang, Feng, Wu, & Hu, 2016).

In a study, the energy absorption efficiency of composite hemispherical shells was investigated in terms of structure constitutes and geometry as well. Glass fiber/epoxy and glass fiber/polyester hemispherical shells were manufactured to understand the effects of matrix types, Figure 1.2, whereas carbon fiber/epoxy and glass fiber/epoxy hemispherical shells were produced to determine the effect of fiber reinforcement. The effects of fiber type on load-deformation and energy-deformation relations are given in Figure 1.3. The importance of aspect ratio (R/t) was also investigated to elucidate the effect of geometry under quasi-static axial compressive load. Therefore, hemispherical composite shells were studied with varying aspect ratios.

The effects of aspect ratio on load-deformation and energy-deformation relations are presented in Figure 1.4. It was clarified that a decrease in aspect ratio influenced deformation mode of hemispherical composite structures directly and reinforcement type has the major effect on crashworthiness parameters of the structure (Saleh, Mahdi, Hamouda, & Khalid, 2004).

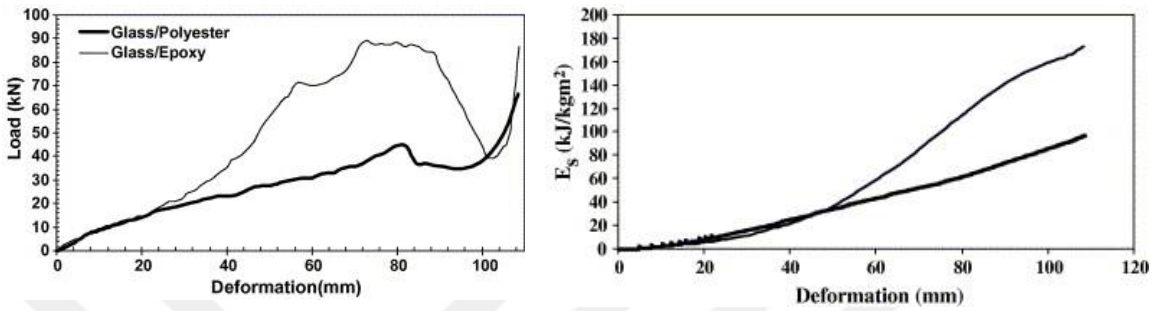

(a) (b)

Figure 1.2. Effect of matrix type; (a) load-deformation and (b) energy-deformation relations (Source: Saleh et al., 2004).

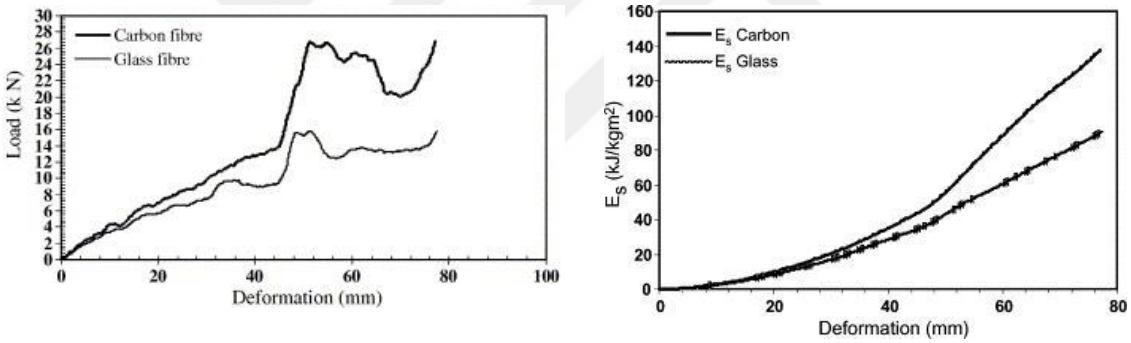

(a) (b)

Figure 1.3. Effect of fiber type; (a) load-deformation and (b) energy-deformation relations (Source: Saleh et al., 2004).

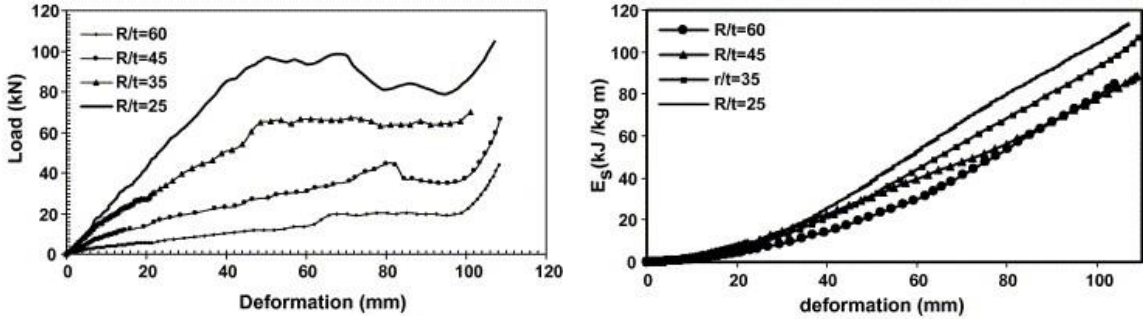

(a) (b)

Figure 1.4. Effect of R/t ratio; (a) load-deformation and (b) energy-deformation relations (Source: Saleh et al., 2004).

An experimental study was performed to investigate the deformation behavior of aluminum closed cell foam-filled composite tube under quasi-static crushing load. It was found that foam material affected the deformation behavior of composite tube and the composite tube was failed due to the confinement effect of foam material. In addition, load carrying capacity of composite/Al hybrid tube was greater than the arithmetical sum of the empty composite structure and empty Al specimen due to the interaction between tubes (Guden et al., 2007).

One of the principle components preferred in lightweight armor design as an energy absorber is sandwich construction, which composes of low density and thick core material between high density and thin face sheet materials due to the ratio of high flexural stiffness to weight, the ratio of high strength to weight and high energy absorption capability. The face sheets are selected among the materials of high resistance to bending and stretching loads. Furthermore, the top face sheet and bottom face sheet can be selected from different materials with different thickness. There is no restriction on whether core material of a sandwich plate is from any material having a wide variety of densities and shear moduli. General types of core materials are foam or solid core, honeycomb core, web core and corrugated or truss core. In most foam-core and honeycomb-core sandwiches, regardless the bending and in-plane loads, faces carry almost all initial loading, while core withstands transverse shear loads. When sandwich structure consists of web-core and truss-core, then one can assume that core material carries a part of the in-plane and bending loads (Vinson, 1999). In order to obtain a sandwich structure, a thin layer adhesive material is used to bond core material and face sheet material each other. A core material which is placed between two face materials can be of different materials and different geometries. Considering the fine mechanical properties of the components, to obtain a sandwich structure as an energy absorber having targeted mechanical properties is an adequate reason to prefer.

Sandwich structures made from metals and composite materials are often used for protection against impact and explosion loads since they absorb a high amount of energy during crushing. Although there are many studies to investigate the optimum core geometries of sandwich structures, mainly investigated cores are in the form of metallic foams, polymeric foams, pyramidal, honeycomb, corrugated and truss.

Many researchers studied the dynamic deformation behaviors of metallic and polymeric foams. In a study, it was reported that aluminum foam core sandwich

structures are more efficient than a foam material without aluminum face sheets in terms of energy absorbing under blast loading. According to the researchers, this resulted from difference and complexity of deformation behavior of the face sheet (Hanssen, Enstock, & Langseth, 2002). In another study, sandwich panels again made of aluminum foam core were subjected to quasi-static and dynamic loads so as to investigate perforation mechanism of the sandwich structures. Foam material more deformed locally under dynamic load due to the inertia effect than that of under quasi-static load and strain hardening effect of the foam material caused an enhancement in the maximum force value before perforation (Zhao, Elnasri, & Girard, 2007). However, energy dissipating performance of sandwich structures made of metallic foam and metallic face sheets materials depends on several factors different from the effects of face sheets and foam materials such as face sheet thickness, impact velocity, projectile shape, density and thickness of foam material. It was presented that as the thickness of face sheets and core increases, energy absorbing capacity and delamination area of sandwich structures increases. Contrary to impact loading, the larger tearing damage was observed on the bottom face of the sandwich when the structure subjected to a quasi-static load. Furthermore, the energy dissipation was remarkably affected by projectile shape and foam density (W. Hou, Zhu, Lu, & Fang, 2010). In order to compare the performances of metallic and polymeric cores under low velocity, sandwich structures consisting of aluminum face sheets were tested. Although yield strengths of aluminum alloy foam and polymeric foam are close to each other, it was revealed that they have different properties regarding energy absorption capacity, penetration force and damage initiation force (Rajaneesh, Sridhar, & Rajendran, 2014).

Mechanical properties of honeycomb materials and honeycomb sandwich structures were investigated to determine the crashworthiness, energy dissipation and force transmission of structures experimentally. Aluminum and Nomex were used as core materials due to their specific absorbed energy and low price properties (Goldsmith & Sackmant, 1992). Even though aluminum or Nomex honeycomb sandwich structures were compared to thick face materials with several combinations in terms of the peak value and energy absorbing characteristic under the same conditions, the significant diversity was seen in the deformation modes. Additionally, a configuration consisting of the aluminum honeycomb core and thin face sheet was determined as the most efficient one (Moriarty & Goldsmith, 1993). In order to demonstrate the superior property of

sandwich structures, square honeycomb core sandwich beams and monolithic solid beams made of stainless steel were investigated under shock loading both experimentally and numerically. It was found that the sandwich beams less compressed than monolithic solid beams when they subjected to high impact load. Nevertheless, sandwich beams were most effective energy absorber structures when they were subjected to lower impact velocity (Rathbun et al., 2006). In another study, super-austenitic stainless steel alloy was selected so as to produce square honeycomb core sandwich structures. Mechanical behavior of sandwich structures under air blast loads were studied both experimentally and numerically and obtained results were compared with the solid plates having approximately the same weight. Explosion distance was constant and the charge weight changed three times during experiments. Therefore, three experiment series occurred. At the end of the research, it was presented that the utilization of honeycomb sandwich structures gained advantages to withstand the air blast loads due to the cell wall buckling during the explosion (Rathbun et al., 2006).

Several types of research proposed opting of the corrugated structures to use where flex and stiff materials are needed and authors conducted a study to stand behind their idea about mechanical properties of corrugated structures. Moreover, a method was developed theoretically on shear stress can be applied to composite materials also (Buannic, Cartraud, & Quesnel, 2003). In the light of this information tensile and flexural experiments of corrugated composite structures were performed, significant mechanical properties in the transverse direction were observed both experimentally and numerically (Yokozeki, Takeda, Ogasawara, & Ishikawa, 2006). In another study, scientists focused on the compressive strength of corrugated and diamond lattice materials manufactured from stainless steel material. Further, they found that the pyramidal and square honeycomb structures more desirable than prismatic corrugated and diamond lattice materials in terms of energy absorbing capacity under compression load (Côté, Deshpande, Fleck, & Evans, 2006). Corrugated sandwich structures with various oriented combinations were discussed as multilayer under both quasi-static and dynamic loads in a paper. In this study, lateral confinement effect of interlayer sheets caused to increase in buckling stress. Furthermore, the micro-inertial effect was observed when the interlayer sheets were absence. However, non-homogeneity in the deformation resulting from interlayer sheets was condoned so as to increase the specific absorbed energy value (Kilicaslan, Guden, Odaci, & Tasdmirci, 2014).

Lattice structures are another widely used core materials for sandwich structures. In a study, they were subjected to quasi-static loads to determine the failure mechanism and then structures were evaluated as strain rate sensitive material. When the structure was under blast loading, the increase in yield stress revealed. Moreover, deformation modes of blast experiments were similar with quasi-static test results (Mckown et al., 2008). A similar study was also conducted on lattice structures with lattice core sandwich structures and resemble results were obtained. It was reported that rate sensitivity is a highly important factor among all inferences (Smith et al., 2011).

In many research fields, scientists inspired from the nature to find the proper solution for their problems. Honeycomb structures are the only one of them. When the high energy absorption capacity and penetration resistance are expected for protection systems, thin walled structures are non-ignorable due to their leading mechanical properties as mentioned above. In the scope of this study, a novel thin-walled geometry consisting of an inner core and outer shell structures was created inspiring from a sea creature to use in defense industry especially. In recent years, a mainstream way to find innovative solutions to complex engineering problems is biomimicry and the biomimetic products should be investigated in detail.

1.2 Biomimetic Products and Balanus Creatures

Biomimicry is an interdisciplinary approach to innovation for the formation of the human-made structures, devices or function of which combines technological and biological systems by emulating nature's strategy. In the last years, it can be obviously seen that especially world's leading countries tend to breakthrough biomimetic based products when research and development projects are considered. Scientists believe that living organisms in nature have optimum designs. In addition, they have survived by means of their own design through natural selection. Biomimetic is a comprehensive study embracing the application of entirely different disciplines to find high-tech materials such as biological science, materials technology and architectural applications.

Biological mimicry of animal forms was seen when Leonardo da Vinci analyzed the birds' flights in detail in the 1400s. He conducted a biomimetic study on anatomy and flying of birds and designed some machines in order to enable human to flight with a flying machine in which he lovingly called "The Great Bird". As a result, he designed

“a flying machine” by mimicking of bird drawings, but never made any successfully. The artificial wings designed by Leonardo da Vinci as shown in Figure 1.5 and it can be seen that the origins of the mimicking nature date back to the 15th century (Kemp, 2006).

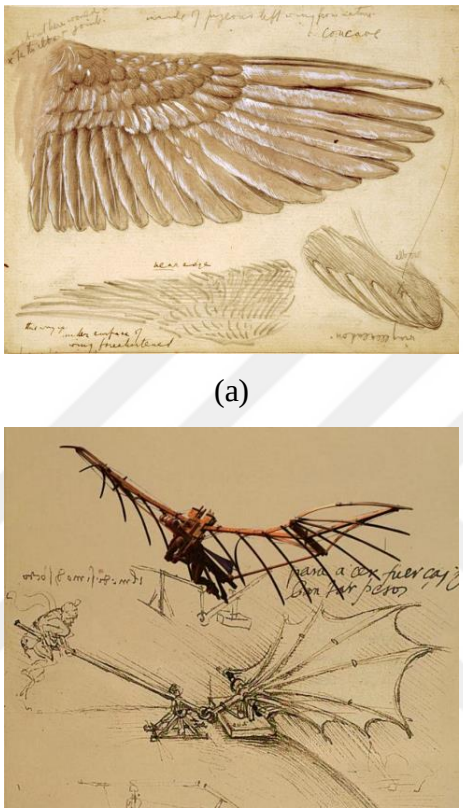

(a)

(b)

Figure 1.5. (a) Leonardo’s study of bird wings illustrating its movement and (b) his flying machine sketch.
(Source: https://f12arch531project.wordpress.com/author/luwanarch/)

Historically, biological approaches to engineering proved even centuries ago; however, biomimetic was first used as the term by Otto Schmitt in the 1950s (Lepora, Verschure & Prescott, 2013).

Biomimetic projects are as popular today as they are in the past. A kingfisher bird consumes fish and it has to be swift while it hunts so as to live on. To make this possible, kingfisher birds have a special head and beak to catch their hunts by limiting water disruption and noise propagation when their hunts are unaware. These features of kingfisher birds inspired the high-speed train. One of the bio-inspired products is a turbine. The invention of turbines is based on inspiration from the ability of fins and a tail of a whale. A whale can move more efficiently at hundreds of meter bellows the sea

using its fins and a tail. In a study conducted on whales, it was discovered that these properties of whales are sufficient to attack under pressure. Furthermore, the efficiencies of not only wind turbines but also cooling fans and airplane wing increased when these properties were replicated from whales. Another recent specific invention is swimsuits. Shark skin inspired swimming costumes and gave advantages for swimmers especially during the 2008 Summer Olympics due to having many overlapping scales called little skin teeth or dermal denticles. Thanks to denticles, the water pass by faster. One of the first examples that come to mind when it comes to bio-inspired structures is a hexagonal honeycomb structure which is commonly used. Increasingly, architects started to observe the nature for a bio-inspired building design. Therefore, the honeycomb configuration inspiration provides structural integrity to maximize strength with less material as possible. The Honeycomb Architecture in South Korea epitomizes the using of honeycomb structure in architecture well. Presented examples above are given in Figure 1.6

(a)

(b)

Figure 1.6. (a) Kingfisher bird and high-speed train (Source: http://biomimicryswitzerland.org), (b) whale flipper and whalepower propeller (Source: https://www.theguardian.com), (c) sharkskin and swimsuit (Source: http://www.mnn.com) and (d) a honeycomb structure and building (Source: https://wiki.ucfilespace.uc.edu).

(cont. on next page)

(c)

(d)

Figure 1.6. (cont.)

Additionally, biomimetic based studies on armor and protection systems were conducted as well. Creatures in nature have developed a system to protect themselves from external factors and this inspired people. The creatures having shell structure can be protected both on land and under water. Undoubtedly, the first things coming to mind are turtles, snails and shellfish (Bar-cohen, 2006). In particular, certain types of mollusks living in the sea have unique, hard and strong shell design in order to preserve themselves against external threats (Raman & Kumar, 2011).

As a result of the preliminary studies carried out, the project was inspired by the design of a sea creature called balanus for the bio-inspired energy absorbing protection system.

Balanus is a small, roughly and conical barnacle and seems like volcano-shaped. There are lots of species living in different coasts and it can be found on almost vertical rough surfaces such as rocks, ships' surfaces, shells, docks and other objects. Despite its appearance, the armor-like wall of balanus is highly strong and it is a close relative of the crustaceans rather than of the oysters.

The life cycle of the balanus consists of three main phases. Balanus is a hermaphrodite creature, a self-fertilised organism. After fertilization, it becomes plankton floating freely in the sea. When it reached the adulthood and proper conditions, it held on a suitable surface. Then, it excretes a material similar to lime,

brings out the outer shells from different layers. After it has formed a protective structure for itself, it becomes an adult balanus. This property makes balanus one of the strong living creatures which are unaffected by the water pressure due to the contribution of confinement effect and these creatures can decelerate the ships when they live on it as colonies. The dimensional measurements of the balanus depend on the species and the ambient conditions they live in. When the geometric forms of balanus creatures were examined, it was found that the bottom diameter varied between 25-30 mm and height ranged from 25 mm to 50 mm (Pope, 1945). The considering these dimension intervals, balanus geometry was manufactured from two thin-walled structures namely the inner core and the outer shell with 25 mm of height, 30 mm of bottom diameter and 75 degree of cone angle. In Figure 1.7, a balanus creature, a balanus colony and a balanus geometry produced from AISI 304L stainless steel are given.

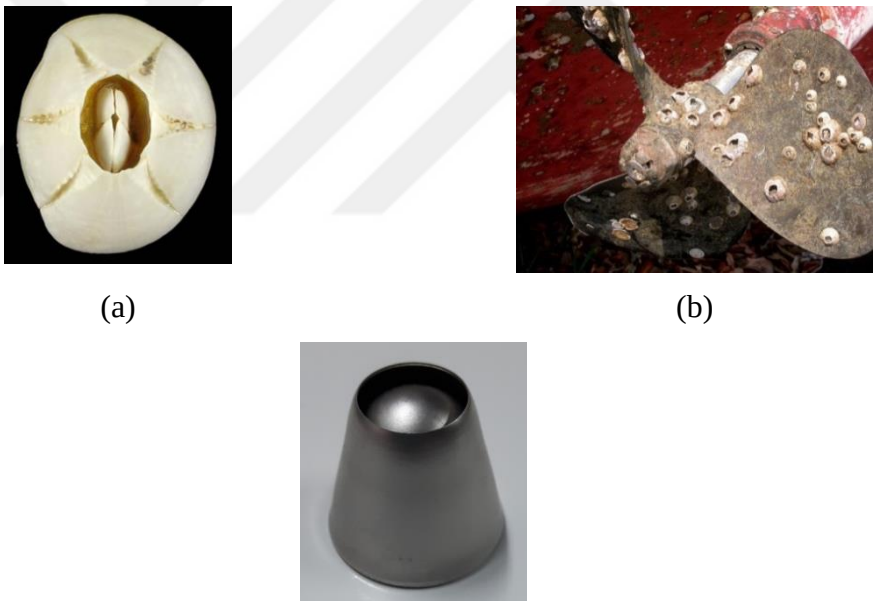

(a) (b)

(c)

Figure 1.7. (a) A balanus creature (Source: http://www.conchology.be), (b) a balanus colony (Source: http://www.mby.com) and (c) balanus geometry inspired from balanus creature.

A numerical balanus specimen was modelled to investigate the advantages of its geometry about the energy absorbing performance. Therefore, a preliminary study was conducted. When the core materials of sandwich structures used as energy absorber are considered, some commonly used conventional geometries can be seen in the form of hexagonal honeycomb, square and cylinder. The aim of the preliminary study was to

compare the crushing behavior of the bio-inspired thin-walled energy absorbing structure with conventional ones. For this purpose, these three conventional geometries and a balanus geometry having the same wall thickness, height and mass exposed to quasi-static loading. In Figure 1.8, absorbed energy-displacement curves of the numerical specimens are given.

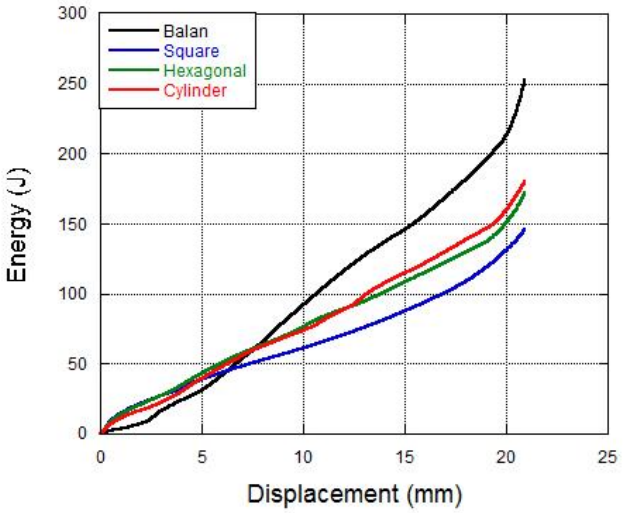

Figure 1.8. Energy absorption capacities of geometries having the same wall thickness, height and mass.

It was seen that proposed bio-inspired energy absorbing geometry has a far superior performance when compared to its alternatives. Balanus geometry absorbs approximately 40 percent more energy than the cylinder which is the most efficient among conventional geometries. As a result of all these preliminary studies, the effectiveness and applicability bio-inspired energy absorbing geometry were proven and it was found to be worth the investigating in detail.

1.3 Aim and Scope of the Study

A growing interest in thin-walled high energy absorbing structures have become popular in many engineering fields due to their desirable mechanical properties. Although biomimetic has a highly significant role in science in the recent years, there are not many studies on energy absorbers. However, this study aimed to design, manufacture and optimize a new bio-inspired energy absorber to contribute to the literature related with crushing behavior of thin-walled structures.

In the current study, the quasi-static and dynamic crushing behavior of the thin-walled bio-inspired structure manufactured from AISI 304L stainless steel were investigated to evaluate the load-carrying efficiency of the structures both experimentally and numerically. The strain rate sensitivity of the material, deformation behavior of the structures, efficiency of the interaction between the components of the balanus, the interface pressure during deformation and the confinement effect of polyurethane foam material are the other topics especially studied in the study at both static and dynamic deformation rates.

In the first chapter, general information about crushing behavior of the energy absorbing structures were mentioned with some examples. Besides, balanus creature was introduced which is a source of inspiration for this study. Furthermore, its advantages were investigated numerically regarding the energy absorption capacity considering the other conventional geometries at the same weight and the results of this preliminary numerical study were presented. In the second chapter, the previous researches in the literature on crushing behaviors of energy absorbing thin-walled structures were presented in detail. In the third chapter, manufacturing of the bio-inspired thin-walled structures, characterization of materials and test methods were given. In the fourth chapter, numerical studies of production and axial compression simulations at quasi-static and dynamic strain rates were briefly explained. Further, material models used in numerical studies and their properties were explained and tabulated. In the fifth chapter, experimental and numerical results of both manufacturing process and crushing analyses at static and dynamic strain rates were interpreted. In the sixth chapter, conclusions obtained from the study were given.

CHAPTER 2

LITERATUR SURVEY

2.1 Thin-Walled Structures

One the most commonly used energy absorber structures is thin-walled structures due to their low production cost, higher energy absorbing capacity and progressive deformation mode. Such structures are mainly used where the protection from dynamic crushing and explosive loading is necessary such as defense industry. The superior crashworthiness performance of thin-walled structures having conventional geometry was introduced briefly in the previous chapter. Besides, the literature survey of thin-walled structures concentrated on the conical structures, combined geometries and bi-tubular structures since balanus geometry resembles to a combination of them.

2.2 Crushing Behavior of Thin-Walled Conical Tubes

The utilization of thin-walled tapered metallic tubes having rectangular cross-section as energy absorber was compared to the straight geometries by Reid and Reddy. Illustrations of the specimens used in the study are given in Figure 2.1. Their deformation behaviors were investigated under both quasi-static and dynamic strain rates. Progressive buckling was observed during quasi-static crushing of both straight and tapered tubes. However, the straight specimens started to fail with increasing cross-sectional dimensions. Therefore, crushing experiments conducted on solely tapered specimens. Deformation behaviors of tapered specimens were determined as steadier than that of the straight one. Further, dynamic tests were performed by drop tower test setup and an increase in energy absorbing capacity was observed due to strain rate sensitivity. The tapered structures deformed in the same mode as is in the case of quasi-static and they initiated to deformation from small end contrary to the straight tubes, which often start to deform from the middle of the length. Due to advantages mentioned

above, tapered tubes can be preferred as energy absorber substituted for the straight tubes (Reid & Reddy, 1986a).

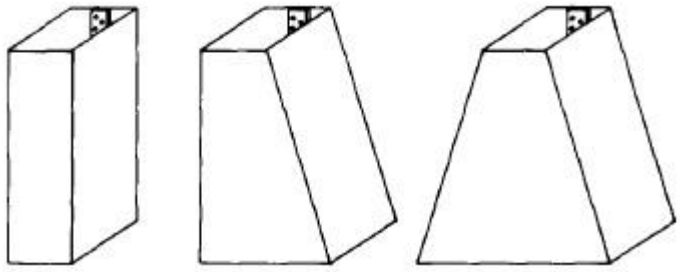

Figure 2.1. Illustration of straight, one side tapered and two sides tapered tubes, respectively (Source: Reid & Reddy, 1986a).

Reid and Reddy studied on the effect of polyurethane foam-filled tapered metal tubes under both quasi-static and dynamic deformation rates experimentally and theoretically. Empty tubes also were investigated to compare the results. They indicated that polyurethane foam-filled tapered thin tubes have greater specific absorbed energy capacity than the others. Moreover, foam material reduced the fluctuations in the crushing force (Reid & Reddy, 1986b).

A similar parametric study on aforementioned structures was conducted at static and dynamic strain rates both numerically and experimentally. When the obtained results are examined in detail, it was found for the empty structures that the increase in the number of tapered edges has a great effect on the initial peak value and causes to decrease. When it comes to foam-filled structures, tapered structures again showed their advantages on the initial peak value and energy absorbing at dynamic strain rates than quasi-static due to strain rate sensitivity. The fact that the mean force value of these structures are higher than the others and this make their desirable crashworthiness more clear (Mirfendereski, Salimi, & Ziaei-Rad, 2008).

Plastic deformation behavior of conical structures having large semi-apical angle was investigated under quasi-static load by Gupta. As a results of experiments conducted with metal tubes it is seen that deformation mode of conical structures having lower semi-apical angle than 30° is diamond. When the angle is between 44° and 65°, the effects of rolling plastic hinge can be observed on the deformed specimen. Nevertheless, if the angle is greater than 65°, reverse bending can occur and this is undesirable deformation mode (N. K. Gupta, Prasad, & Gupta, 1997).

(a) (b)

Figure 2.2. Reverse bending (a) top view and (b) bottom view
(Source: N. K. Gupta et al., 1997).

In an another experimental study, hemispherical and conical structures having different sizes were compared in terms of deformation behavior and energy absorbing characteristics at static and dynamic strain rates since their deformation behaviors are based upon the occurrence of rolling plastic hinges, Figure 2.3 (a). Obtained data showed that deformation behavior of hemispherical structures is rate sensitive. Therefore, deformation mode and force-displacement curve of the conical structures under static and dynamic conditions are similar whereas these properties depend on the critical ratio of radius to thickness for hemispherical structure. Further, the mean crushing force of hemispherical structures is affected positively from an increase in the ratio of radius to thickness. Similarly, the mean crushing force and energy absorbing efficiency of conical structures is influenced positively from an increase in the ratio of thickness to radius. However, revers bending can be observed in crushing of conical structures having semi-apical angle greater than 65°, causing adversely effect on energy absorbing (Easwara Prasad & Gupta, 2006).

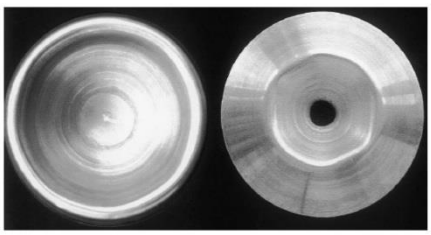

(a)

Figure 2.3. (a) Rolling plastic hinge and (b) deformation behaviors of hemispherical and conical structure under static (S) and dynamic (D) conditions
(Source: Easwara Prasad & Gupta, 2006).

(cont. on next page)

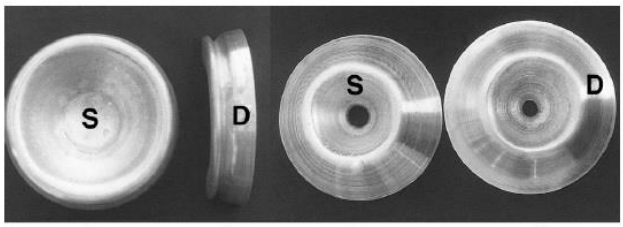

(b)

Figure 2.3. (cont.)

N. K. Gupta *et al*. conducted a study on conical frusta structures made of aluminum and investigated their buckling mode under axial loading. The thickness of specimens varied from 0.7 mm to 1.62 mm and semi-apical angles changed between 16° and 29°. Therefore, forty specimens were prepared for experiments. Deformed shape of conical frusta structures were photographed interrupting at the various displacement of crushing tests to observe the deformation mode and force-displacement data were accumulated. Conical specimens deformed in three different deformation mode, inversion of the cone, concertina mode and diamond mode. It is clarified that specimens having specific geometrical properties, which have the ratio of mean diameter to a thickness less than 87.9, the ratio of height to thickness less than 67.45 and the thickness higher than 1.4 mm, initiated to deform in concertina mode symmetrically up to small deformation and then switched to diamond mode. Further, other specimens having different geometrical properties, which have the ratio of mean diameter to thickness higher than 94.89, the ratio of height to thickness greater than 57.87 and the thickness less than 1.2 mm, asymmetric lobes were observed at the beginning of the plastic deformation. It is possible to predict from tests that multiple lobes are occurred for all thickness values when the ratio of mean diameter to thickness and the ratio of height to thickness less changed between 40 and 218. Numerical models were created in ANSYS since to measure or observe some properties cannot be possible during experimental studies. Four specimens having the same semi-apical angle and different thickness were analyzed numerically and deformation modes were investigated. C21 specimen deformed with concertina mode while C22 specimen deformed in diamond mode. As seen in Figure 2.5, bottom region inversion observed experimentally in specimen C6. This study shows that both load carrying capacity and deformation mode can be controlled arranging the dimensions of conical frusta (N. K. Gupta, Sheriff, & Velmurugan, 2006).

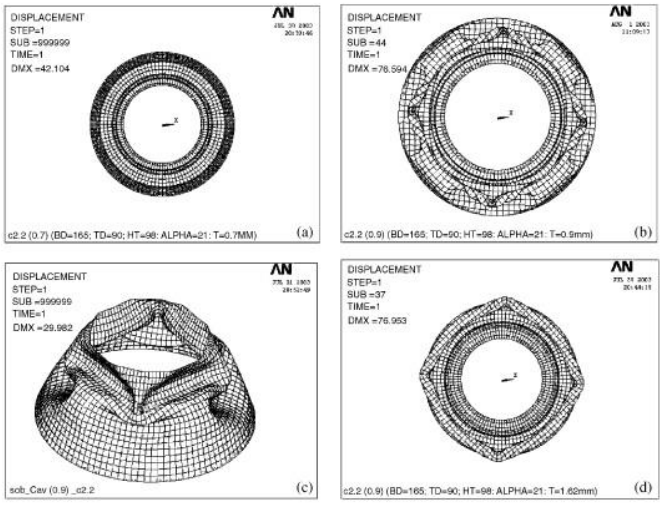

Figure 2.4. Deformation modes of numerically deformed specimens; (a) C21, (b) C22, (c) C23 and (d) C24 (Source: N. K. Gupta et al., 2006).

Figure 2.5. Deformed specimens (Source: N. K. Gupta et al., 2006).

N. K. Gupta and Venkatesh performed a study on aluminum thin-walled frusto-conical shells, having various semi-apical angles and the ratio of mean diameter to thickness, subjected to both axial impact loading with drop weight test setup and quasi-static loading. During impact axial crushing, drop mass was constant whereas impact velocity was changed to detect the effects of deformation rate on energy absorbing capacity. The results showed that as deformation rate increases, energy absorbing capacity and mean crushing force increase than that of quasi-static. Additionally, semi-apical angle highly influenced not only deformation mode but also load carrying capacity of the structures. The structures having less semi-apical angle than 30° were deformed in axisymmetric concertina mode and continued with diamond mode. The other specimens having higher semi-apical angle than 30° deformed in axisymmetric concertina, but deformation proceeded with non-axisymmetric concertina (N. K. Gupta & Venkatesh, 2007).

Mohamed Sheriff *et al*. believed that consideration of the dimensional properties of thin-walled conical structures contribute to enhance the efficiency of energy-

absorbing structures. Therefore, they developed a numerical and an experimental system. To investigate the effectiveness of the structures under dynamic loads, they benefited from drop weight test setup. Their obtained data showed that the most substantial variables are angle and thickness rather than bottom diameter and length of the structures. According to the results, the decreasing semi-apical angle has also massive effect on load-carrying capacity. Thus, the structures deformed more and absorbed high energy (Mohamed Sheriff, Gupta, Velmurugan, & Shanmugapriyan, 2008).

A study was conducted on foam-filled conical tubes subjected to a quasi-static axial crushing load to determine the significant effetcs which affect the deformation mode and energy absorbing capacity of the structures by Ahmad and Thambiratnam. Controlled experiments were conducted to elucidate the effects of density of foam material, wall thickness and semi-apical angle. Further, each factor was also investigated numerically in LS-DYNA. Except for the semi-apical angle, the wall thickness and foam density have higher effects to control the energy absorbing capacity and the mean load of the structures, Figure 2.6. Besides, foam material leads to a slightly increase in the initial peak value. However, variations of density of foam material do not influence the initial peak value as much as foam density (Ahmad & Thambiratnam, 2009a).

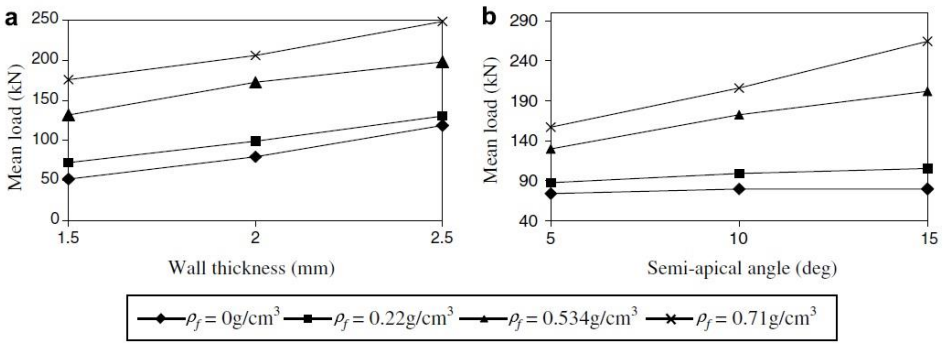

Figure 2.6. Effects on the mean load of; a) wall thickness & density and b) semi-apical angle & density (Source: Ahmad & Thambiratnam, 2009a).

It is also pointed out that increasing wall thickness affects specific absorbed energy positively while increasing semi-apical angle influences SAE value negatively, Figure 2.7 (a). As seen in Figure 2.7 (b), absorbed energy per unit deformed length is increased with increasing both wall thickness and semi-apical angle. Moreover, foam

filled tubes are much more efficient than empty tubes at the same deformation in terms of energy absorbing due to more crushing of foam rather than deformation of the wall (Ahmad & Thambiratnam, 2009a).

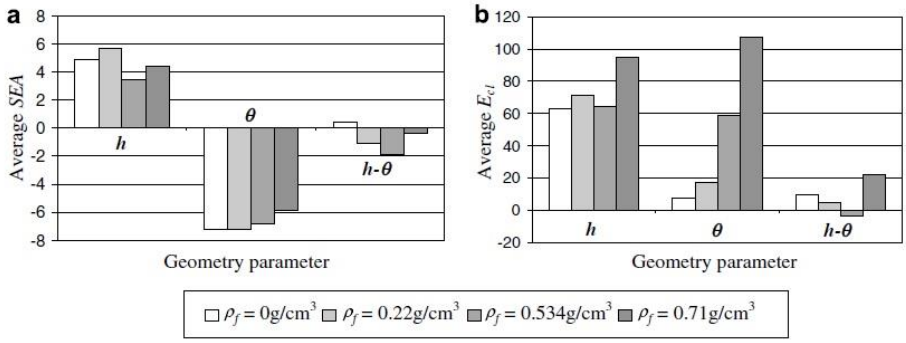

Figure 2.7. Effects of density, wall thickness and semi-apical angle on; (a) SAE and b) absorbed energy per unit deformed length
(Source: Ahmad & Thambiratnam, 2009a).

In Figure 2.8, it is clear that fold formation increased in a foam-filled conical tube having 5° of semi-apical angle. Nevertheless, a number of the fold and fold length in foam-filled conical tube close to empty one having of 15° of semi-apical angle and an increase in mean load can be explained by the effect of foam density. Eventually, the number of fold formation in a foam-filled structure depends on the semi-apical angle, foam density and wall thickness (Ahmad & Thambiratnam, 2009a).

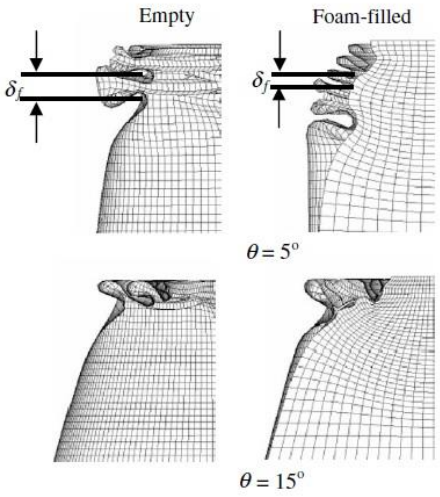

Figure 2.8. Effects of foam material and semi-apical angle on fold formation
(Source: Ahmad & Thambiratnam, 2009a).

Ahmad and Thambiratnam analyzed aforementioned foam-filled conical structures under axial impact load in LS-DYNA. This time, parameters of controlled experiments were expanded and load parameters, impact mass and impact velocity, were added. It is clearly stated that energy absorbing capacity increases under dynamic impact load due to not only foam material but also the interaction between foam material and surface of the conical tube. Further, global buckling does not observe. In addition, the semi-apical angle has a less effect on empty tubes in terms of dynamic energy absorbing and absorbed energy value remains almost stable for a constant wall thickness. However, this situation has a contrast result for foam filled tubes, Figure 2.9 (Ahmad & Thambiratnam, 2009b).

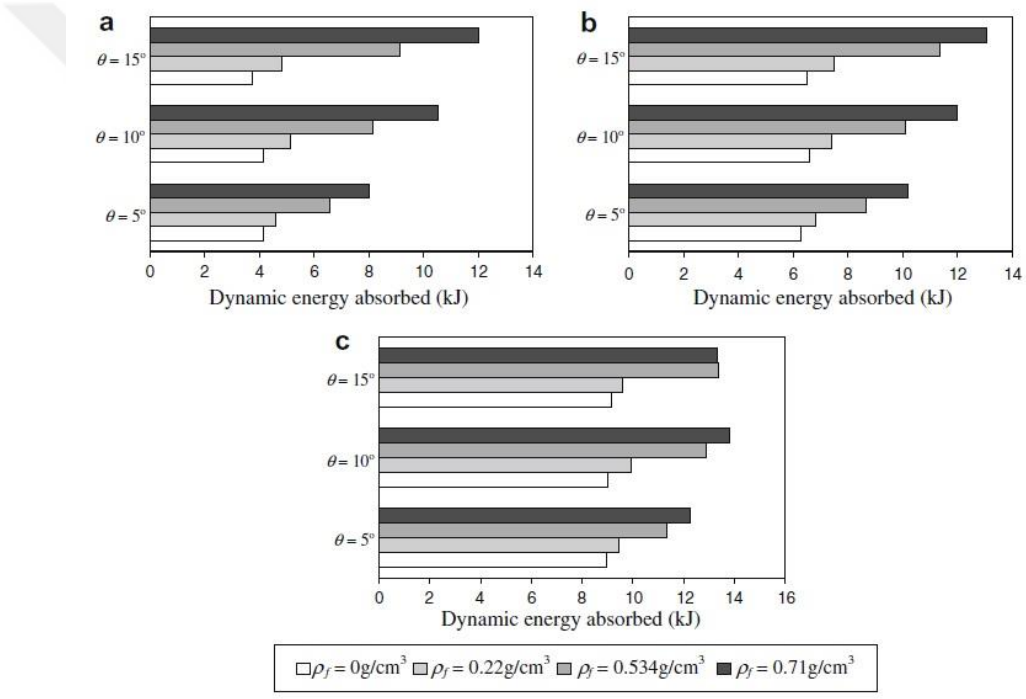

Figure 2.9. The comparison of the efficiency of semi-apical angle and foam density on energy absorbing capacity under dynamic load at a constant collapse with the structures having different wall thickness; (a) 1.5 mm, (b) 2 mm and (c) 2.5 mm (Source: Ahmad & Thambiratnam, 2009b).

The results in Figure 2.10 show that there is no important contribution of impact mass and impact velocity on energy absorbing capacity of empty and foam-filled conical tubes as much as the aforementioned effects.

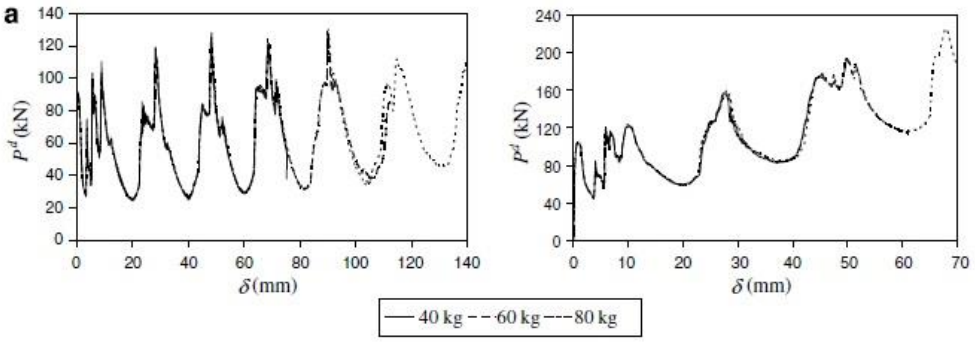

(a)

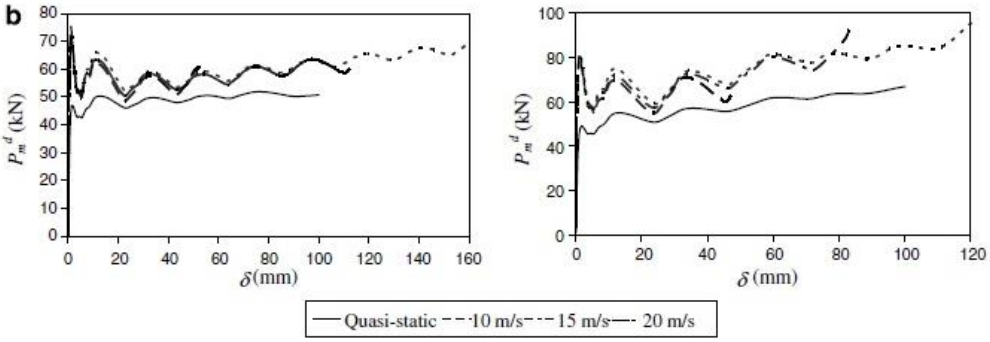

(b)

Figure 2.10. (a) Influence of impact mass and (b) influence of impact velocity on load carrying capacity of empty and foam-filled structures, respectively (Source: Ahmad & Thambiratnam, 2009b).

As seen in Figure 2.11, empty and foam-filled tubes deformed in concertina mode at the beginning of the deformation. At the 20 m/s of impact velocity, it is evident that filler material switched the deformation mode of the empty tube from diamond to concertina. Beyond 20 m/s of impact velocity, each type of tubes deformed with concertina mode and this resulted in an increase of energy absorbing capacity (Ahmad & Thambiratnam, 2009b).

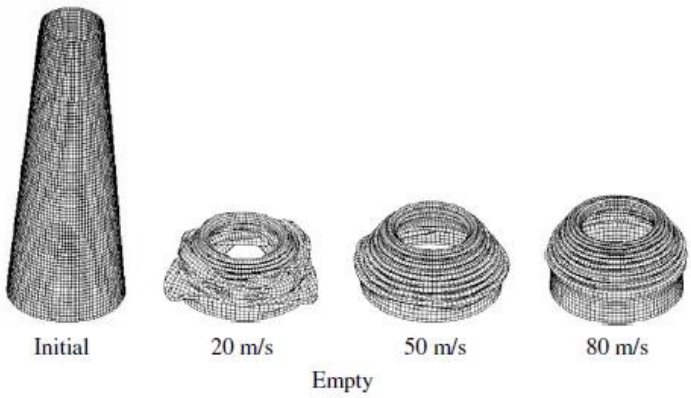

(a)

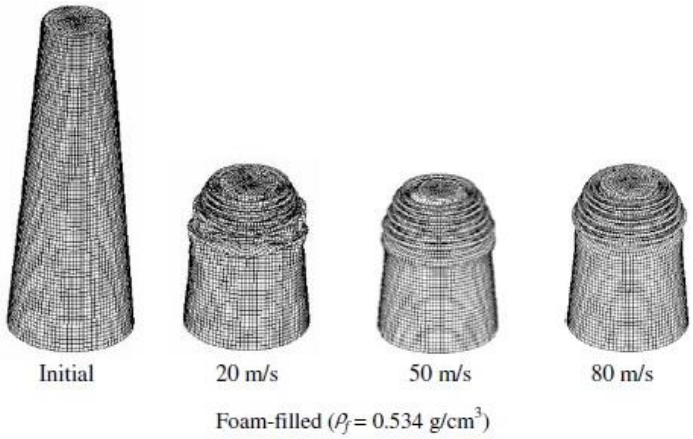

(b)

Figure 2.11. Deformation modes of conical tubes at various impact velocities; (a) empty and (b) foam-filled (Source: Ahmad & Thambiratnam, 2009b).

2.3 Combined and Bi-tubular Geometries

Gupta *et al*. conducted a study on an aluminum thin-walled combined geometry consisting of a conical portion and a hemispherical cap over it in terms of load-carrying capacity and deformation behavior. The structure was investigated under quasi-static and dynamic strain rates both experimentally and numerically. The geometrical parameters and a sectional view of the combined geometry are seen in Figure 2.12 (a) & (b), respectively.

(a) (b)

Figure 2.12. (a) Technical drawing of the combined geometry and (b) its sectional view (Source: N. K. Gupta, Mohamed Sheriff, & Velmurugan, 2008).

The effects of thickness, semi-apical angle of cone, height of each part, top diameter and bottom diameter of cone were investigated in detail. In Figure 2.13, A region and B region represent the crushing of hemispherical part and conical part of S8 specimen, respectively. It is seen clearly from the curves, the only 5° of increase in semi-apical angle influenced the load-carrying capacity of the structure under quasi-static loading and approximately 10 kN increase was observed. The load-deformation curve of S8 (t=1.6 mm) is enough to indicate that the deformation of hemispherical part begins with initial flattening and then continues with the inward dimpling. Further, conical part of the structure deforms progressively and axisymmetric folds occur. Numerically and experimentally deformed view of S8 is given in Figure 2.14. When the Figure 2.13 and Figure 2.14 were examined together, it is seen that relatively high constant thickness is another significant magnitude influencing the not only crushing behavior but also deformation mode.

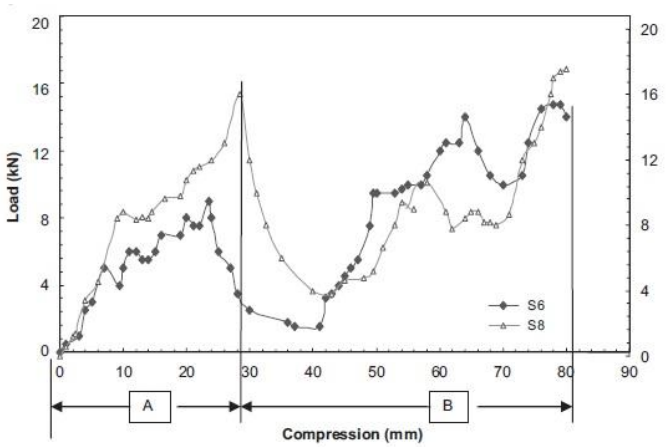

Figure 2.13. The quasi-static force-deformation curves of S6 (t=1.6 mm, α=21°, D_{bottom}=165 mm) and S8 (t=1.6 mm, α=25°, D_{bottom}=165 mm) (Source: N. K. Gupta et al., 2008).

(a) (b)

Figure 2.14. Deformed views of S8 (t=1.6 mm) ;(a) numerical and (b) experimental (Source: N. K. Gupta et al., 2008).

In Figure 2.15, crushing behavior of S8 at different strain rates is given. The curves are enough to explain that load-carrying capacity increased with increasing deformation velocity due to strain rate effect. However, it is obvious when looked carefully at the curves that the conical part has a non-negligible contribution to energy absorbing capacity.

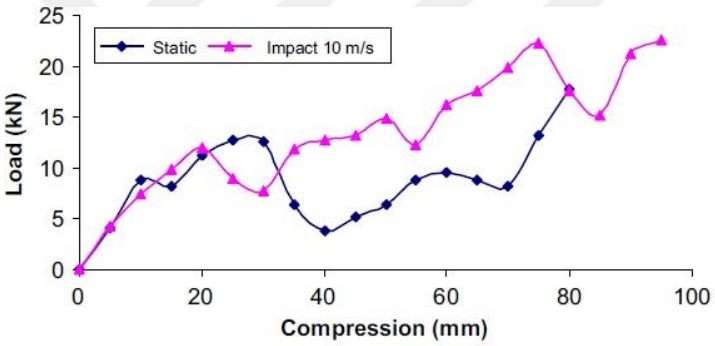

Figure 2.15. Crushing behaviors of S8 under quasi-static and dynamic loadings (Source: N. K. Gupta et al., 2008).

In another study, hemispherical cap geometry was compounded with cylinder and this produced a new combined geometry was investigated under quasi-static and dynamic loading in terms of energy absorbing performance, experimentally and numerically by Tasdemirci *et al.*. Specimens including thickness distribution throughout the section as a consequence of deep drawing process were modelled using LS-DYNA 971. The thickness variations of produced numerical specimens were match well with the experimental thickness measurements. Therefore, it was investigated extensively which component of the combined geometry how affects the energy absorbing performance by simulations. In Figure 2.16, energy partitions between the hemispherical part and the cylindrical part of S2 combined geometry under both quasi-static and dynamic loading are given. S21 represents the quasi-static condition in the

figure while S22 symbolizes the dynamic condition. As is seen in the figure, the most effective part is hemispherical cap at both strain rates up to 35 percent of deformation and absorbed almost all energy. When the deformation of cylindrical part began, both components shared the absorbed energy at about 75 percent of crushing. With further deformation, the fold formation was occurred in cylindrical portion and its energy absorbing performance ascended. Moreover, when the other configurations of specimens were taken in consideration, specific absorbed energy and mean crushing force values of the specimens having the same radius improved depending on the increase in thickness. However, when it comes to an increase in radius value, the only mean crushing force of the specimens having similar thickness distribution showed an increase whereas specific absorbed energy diminished (Tasdemirci, Sahin, Kara, & Turan, 2015).

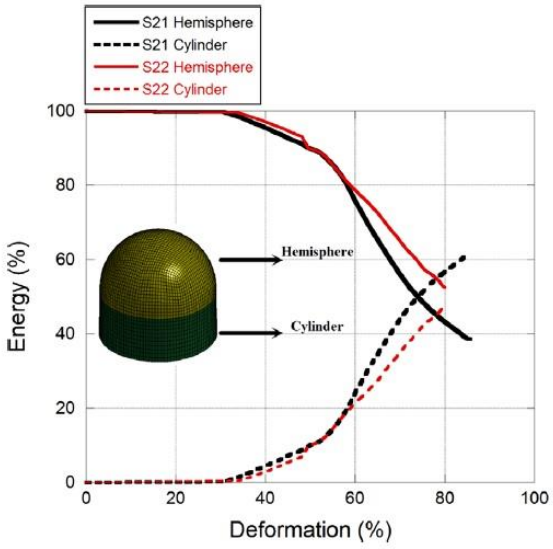

Figure 2.16. Energy partitions between the components of S2 combined geometry under both quasi-static and dynamic loading (Source: Tasdemirci et al., 2015).

The authors also concentrated on strain rate and inertia effects in the paper. As seen in Figure 2.17 (a), energy absorbing capacity of hemispherical portion is higher under dynamic loading than quasi-static loading due to both strain rate sensitivity of the material and inertial effects. Nevertheless, it is obvious that the most influenced part from strain rate and inertia effects is cylindrical part as also is seen its energy absorbing performance. It is also shown in Figure 2.17 (b), increase in crushing force greatly influenced from inertia effect after 100 m/s of impact loads (Tasdemirci et al., 2015).

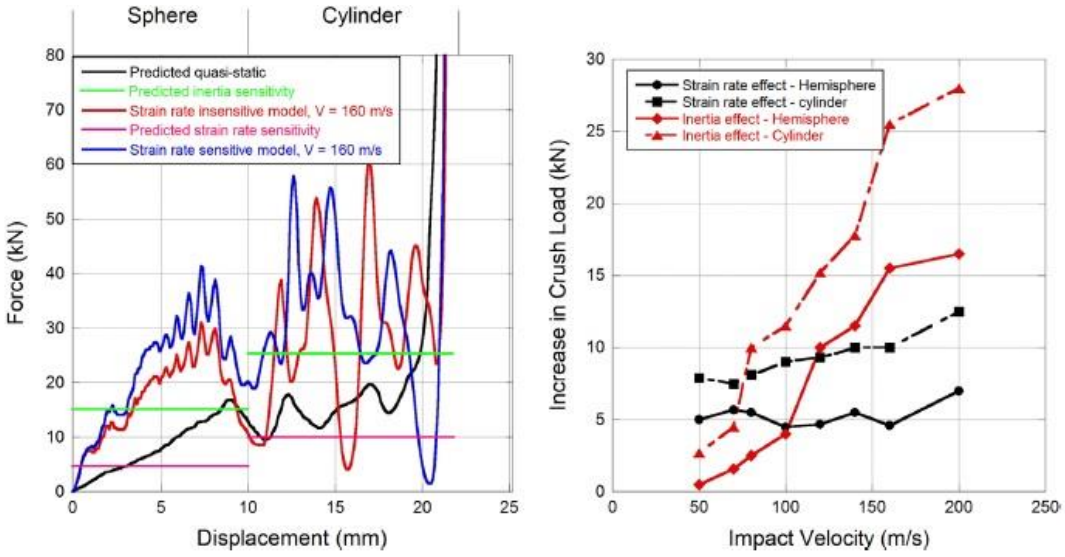

(a) (b)

Figure 2.17. (a) Strain rate and inertia effects at 160 m/s impact velocity and (b) increase in crush load vs. impact velocity
(Source: Tasdemirci et al., 2015).

Gupta carried out a study on thin-walled combined structure consisting of a dome portion and a cone part at quasi-static strain rates. The specimens were manufactured from the sheet metal having 3 mm, 3.5 mm and 4 mm of thickness. Deformation modes and energy absorbing capacity of the aluminum shell structures were investigated in scope of the study, experimentally and computationally (P. K. Gupta, 2017).

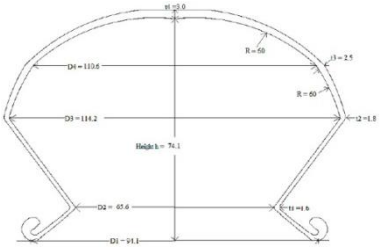

(a)

(b)

Figure 2.18. (a) Illustrations of combined geometry, (b) experimentally deformed specimen and (c) computed view of deformed specimen
(Source: P. K. Gupta, 2017).

(cont. on next page)

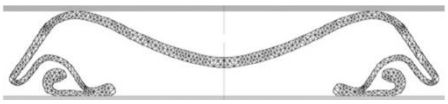

(c)

Figure 2.18. (cont.)

Combined geometry deformed in axisymmetric mode and this explained with the effects of compression, bending and fold formation. These effects are also examined in three plastic regions and four stage compression, Figure 2.19. The structure is interact with the top crushing plate and points p1, p2, p3 and p4 fall in zone I. With further deformation, zone II moves outwards. The structure adjoins to the join of each cone in zone III. In zone IV, the structure falls in joining to the bottom rigid plate (P. K. Gupta, 2017).

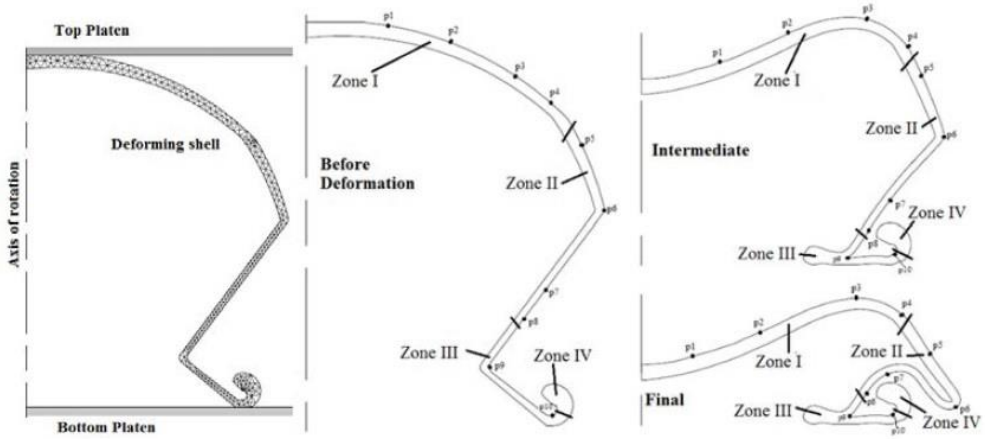

(a) (b)

Figure 2.19. (a) Computational model of axisymmetric deformation and (b) demarcation of zones (Source: P. K. Gupta, 2017).

The comparison of experimental and computational load carrying capacity and energy absorbing performance of the structure is given in Figure 2.20.

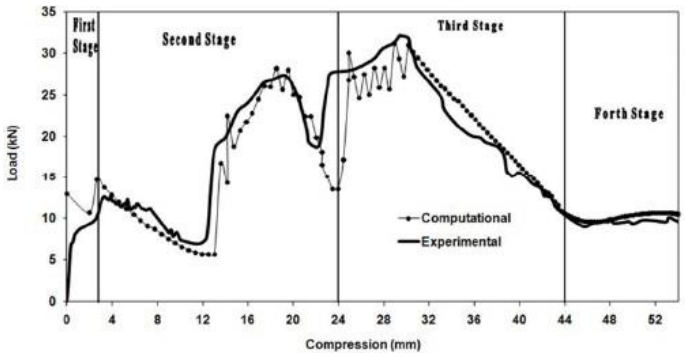

(a)

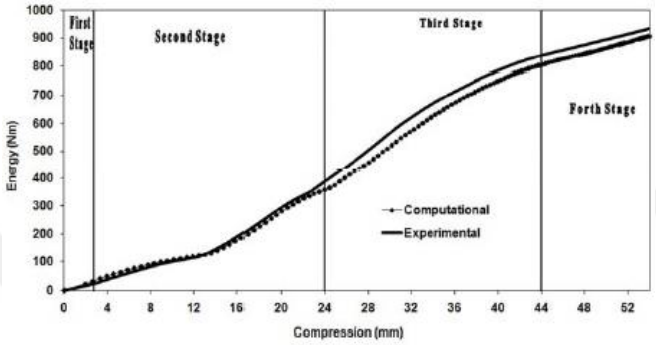

(b)

Figure 2.20. Computational and experimental curves; (a) load-deformation and (b) energy-deformation (Source: P. K. Gupta, 2017).

In order to develop the crushing performance of thin-walled structures, experimental and numerical study was carried out on bitubular square tubes as energy absorber having various arrangements. Bitubular structures have two different configurations consist of parallel and diamond arrangements in the study, Figure 2.21 (a). Firstly, load carrying capacity of single tubes was determined. After the quasi-static compression tests of bitubular tubes were performed, the force-displacement curves of inner tube and outer tube summed up arithmetically. Due to the interaction effect between the constituents of bitubular structure, bitubular specimen carried greater force than that of the sum of its components, Figure 2.21 (b) (Kashani, Alavijeh, Akbarshahi, & Shakeri, 2013).

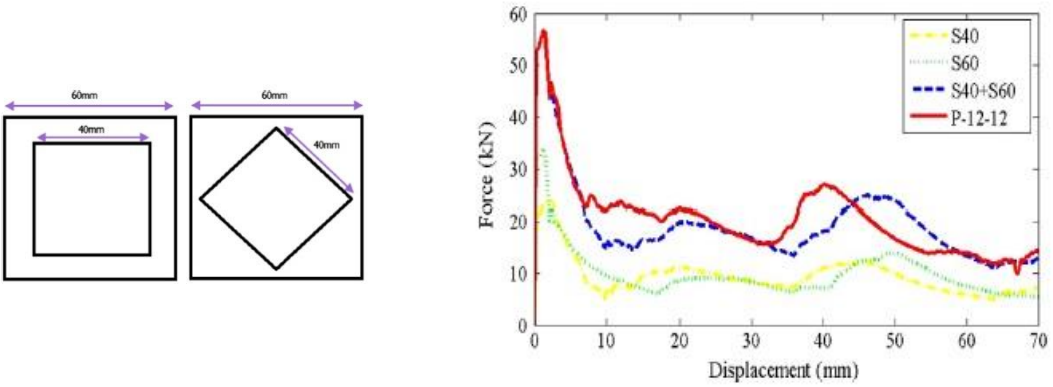

(a) (b)

Figure 2.21. (a) Specimens having parallel and diamond arrangements and (b) comparison of load carrying capacities of parallel arrangement tubes (Source: Kashani et al., 2013).

Xiang and Du conducted a distinct study on thin-walled honeycomb structures. This eccentrical study is based upon the inspiring from ladybeetle. Figure 2.22 shows the source of inspiration and one of designed configurations.

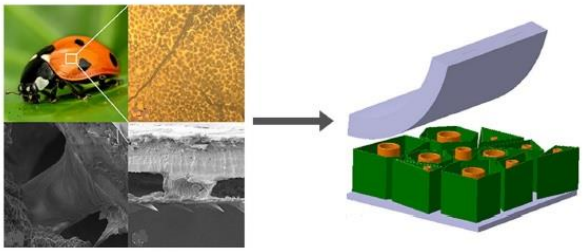

(a) (b)

Figure 2.22. (a) Source of inspiration and (b) designed structure (Source: Xiang & Du, 2017).

Then they arranged more their design and filled the aluminum honeycomb material with columns in two various configurations, Figure 2.23.

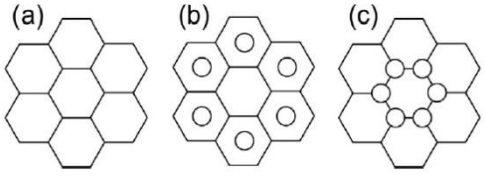

Figure 2.23. (a) Bionic honeycomb structures (BHS), (b) BHTS-1 (tubes between the walls) and (c) BHTS-2 (tubes on the walls) (Source: Xiang & Du, 2017).

Experiments were performed under axial impact load using drop weight test setup and numerical models were prepared using LS-DYNA. Both load carrying capacities and energy absorbing performances of each bionic honeycomb structure were investigated, Figure 2.24. In order to improve the deformation of the BHTS, some parameters such as column diameter, thickness and number of columns are also considered. The obtained results showed that BHTS-2 having 6 tubes on the wall and having 8 mm of diameter is the most efficient configuration (Xiang & Du, 2017).

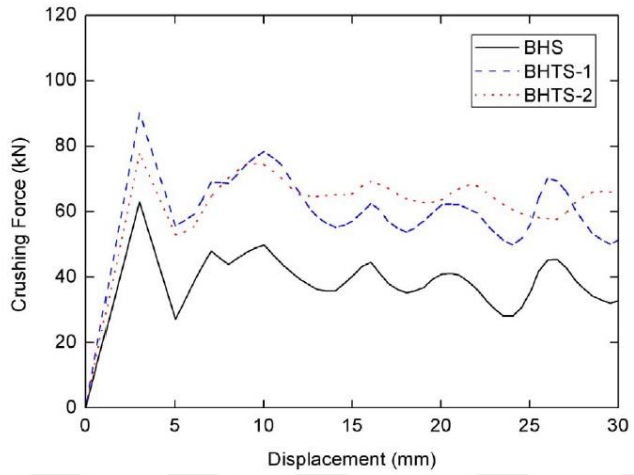

(a)

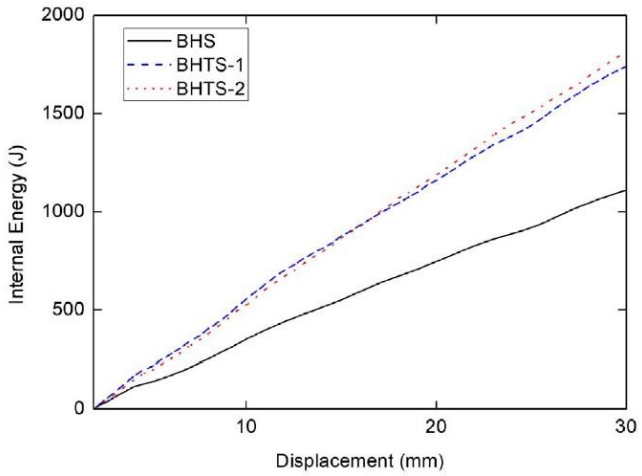

(b)

Figure 2.24. (a) Load-carrying capacity and (b) energy absorbing performance of various bionic honeycomb structures under impact lading (v=10 m/s, m=500 kg) (Source: Xiang & Du, 2017).

Azimi and Asgari presented a unique system having high energy absorbing and load-carrying capacity under both axial and oblique loadings. The new thin-walled system consisting of an inner conical structure and an outer cylinder was tested as foam-filled also. The illustration of new geometry is seen in Figure 2.25. As seen from the figure, the structure has proper geometry can be filled with a filler material.

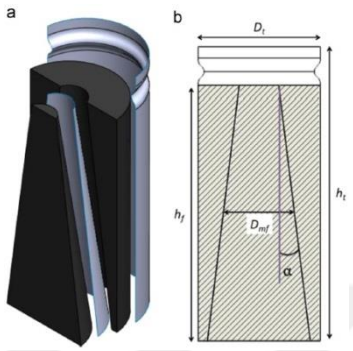

Figure 2.25. Proposed new geometry (Source: Azimi & Asgari, 2016).

Figure 2.26 indicates the effect of interaction between the outer cylinder, the inner conical tube and foam material during deformation.

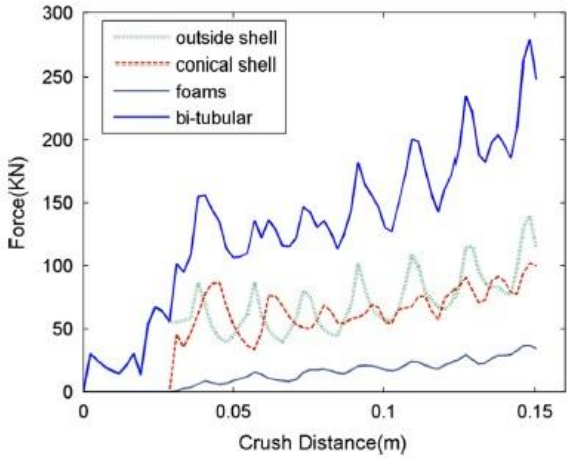

Figure 2.26. Force-displacement curves of the constituents of the structures (Source: Azimi & Asgari, 2016).

The efficiency of bi-tubular structure was compared to other conventional thin-walled crush boxed to cognize the capabilities of the new geometry. In the Figure 2.27 (a), it is noted that the foam-filled structures may not always lead to higher crashworthiness performance and may induce lower specific absorbed energy value. Based on the obtained results from the numerical models of ACE (empty aluminum

circular tube), ACF (foam-filled aluminum circular tube), SFE (empty steel frusta), SFF (foam-filled steel frusta), BTE (empty bi-tubular) and BTF (foam-filled bitubular), the proposed geometry showed desirable specific energy absorbing performance. Figure 2.27 (b) shows that energy absorbing capacity can be improved using bi-tubular structure under oblique loadings also (Azimi & Asgari, 2016).

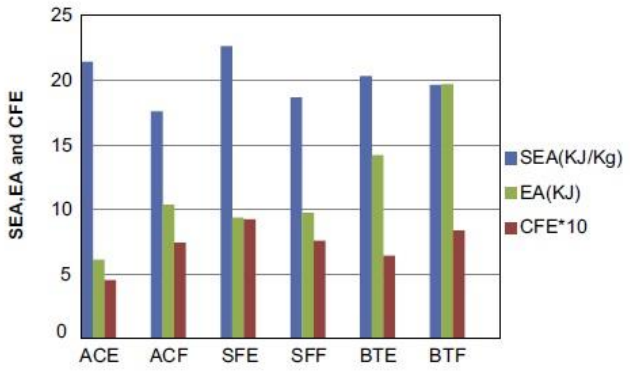

(a)

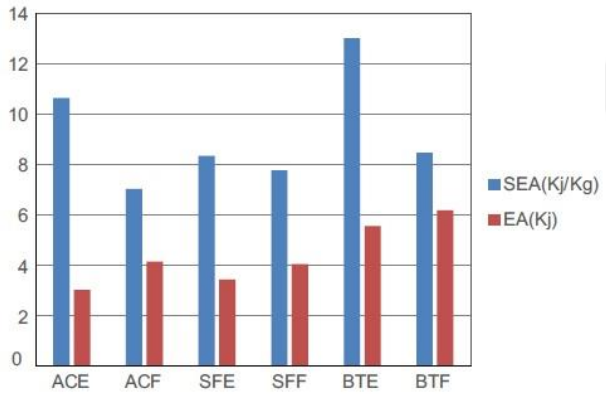

(b)

Figure 2.27. Comparison of the proposed bi-tubular model with other conventional geometries in terms of specific energy absorbed, energy absorption and crushing force efficiency; (a) impact loading (v=20 m/s and m= 200 kg) and (b) oblique loading (impact angle= 30°)
(Source: Azimi & Asgari, 2016).

CHAPTER 3

MANUFACTURING, CHARACTERIZATION AND TESTING

3.1 Design and Manufacturing of Thin-Walled Structures

Bio-inspired thin walled balanus is composed of frusto-conical shell and hemispherical cap core structures. The deep drawing method was preferred to produce the components of the balanus and the sheet metal underwent deformation plastically. The most suitable sheet metals for deep drawing are stainless steel sheets, aluminum, copper, brass etc. with high ductility and low deformation hardening. Among these, stainless steel is the most widely used one due to its strain rate sensitivity effect. Therefore, balanus geometry was manufactured by deep drawing method from AISI 304L stainless steel sheet material with a thickness of 0.5 mm.

3.1.1 Deep Drawing Processes

Deep drawing method is extensively used to transform metallic sheet into different shaped objects used in various industries such as steel pressure vessels, car bodies, aluminum cans and kitchen sinks. As seen in Figure 3.1, an undeformed metallic sheet, called the blank, is placed over the opening of a die and is pushed into the die cavity using a punch. In order to obtain a symmetrically shaped specimen, the blank must be in the middle of the die opening. However, a stainless steel blank material is subjected to irreversible plastic deformation during the process and wrinkling may appear. Therefore, the blank holder is used to apply a force to the outer section of the blank material in order to prevent the blank from flowing freely into the die cavity. The other force is provided for forming of the sheet metal by the punch until it achieves to desired depth in the cavity. Hence, consequently the principal tools required in deep drawing process can be listed as a punch, a die and a blank holder as seen in Figure 3.1.

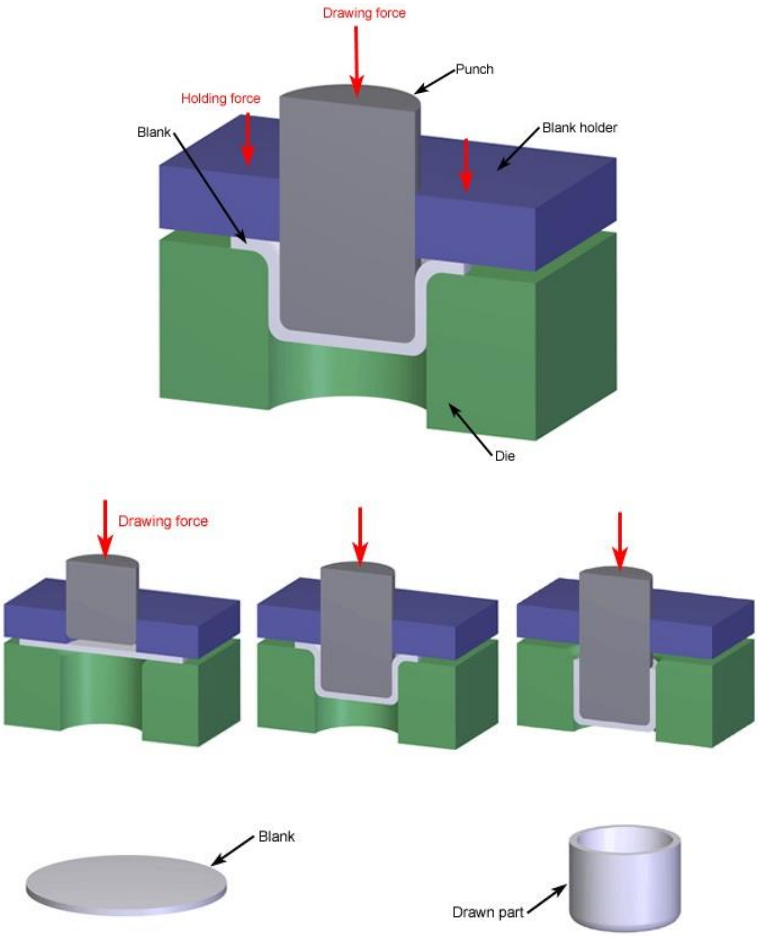

Figure 3.1. Illustration of deep drawing sequence of a circular blank material (Source: www.custompartnet.com).

The form of a deep-drawn part is not limited to the only circle, but also more complex geometries are possible to produce. It is obvious that seamless parts can be produced by deep drawing method and this method has a remarkable role in the manufacturing fields all around the world. Even if several deep drawing methods have been proposed in the last years, development of the methods would not have mean to overcome the problems corresponding to the process. The reason of these problems is caused by the occurrence of plastic deformation. To put it simply, plastic deformation stemmed from huge design and control efforts has an irreversible influence on the mechanical properties of the material. This irreversible effect causes the formation of a high-level strain hardening and residual stress in the structure. It is evident that changes in thickness and strain/stress values throughout the specimen section during deep drawing have a direct impact on the mechanical behavior of the material.

During the forming at ambient temperature, some factors affect the material deformation adversely. Some of these factors are a punch to die clearance, die cavity

depth, punch and die corner radii, blank shape, blank holder force, the coefficient of friction between deep drawing parts and properties of the workpiece material.

The most common damages caused by the factors mentioned above are wrinkling and fracture, Figure 3.2. Wrinkling of the blank material mostly appears if the sheet material is not clamped properly or blank holder force is insufficient. Implementation of appropriate blank holder force is significant criteria for not only wrinkling but also fracture. Normal stress in the thickness direction increases with the high blank holder force, and thus excessive thinning of sheet metal is observed which can results in fracture at the wall of drawn part. Thus, it can be obviously indicated that it is important to provide appropriate force during deep drawing to obtain undamaged parts.

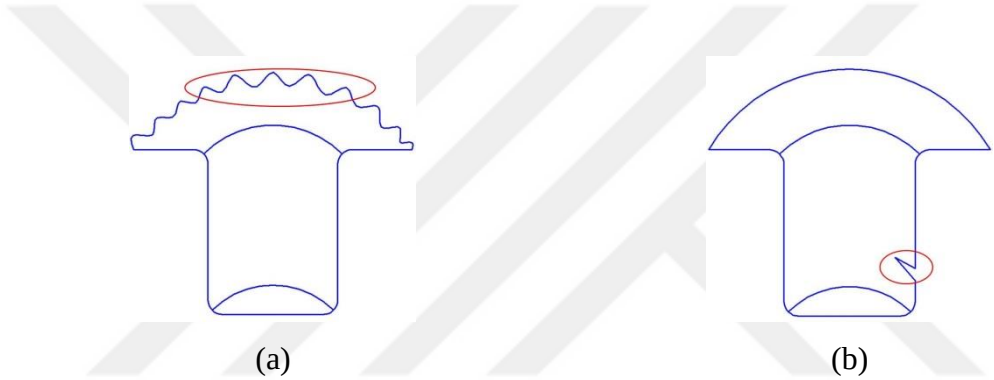

Figure 3.2. Illustration of the most popular failure modes; (a) wrinkling and (b) fracture.

Another preferred method for preventing damage arising from the deep drawing is multi-stage deep drawing method. The main idea of this process is that forming parts are used to shape the blank material progressively. In a typical multi-step process, the drawn length of the blank material in the first stage is less than original length. That is to say, the workpiece obtained at last of the first stage of deep drawing can be redrawn in the subsequent deep drawing process to give final form. Moreover, annealing at last of each stage of deep drawing can help to recover the material for redrawing. Hereby, damages occurred at early stages of drawing process can be obviated by using more than one operation.

In the current study, the thin walled interactive structures were manufactured by two stages deep drawing operation and one trimming operation. The first stage deep drawing model used to obtain the inner core specimen is given in Figure 3.3. The forming molds of inner core and outer shell structures are shown in Figure 3.4 in the

sequence of the first stage deep drawing, the second stage deep drawing and the trimming operation.

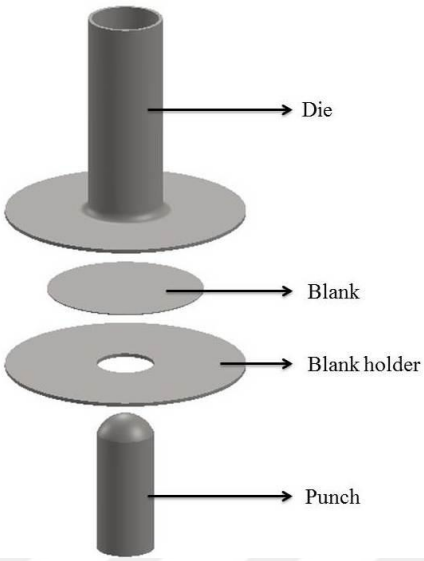

Figure 3.3. Deep drawing model.

(a)

(b)

Figure 3.4. Deep drawing molds; (a) the inner core and (b) the outer shell.

The technical drawings of the geometries are shown in Figure 3.5.

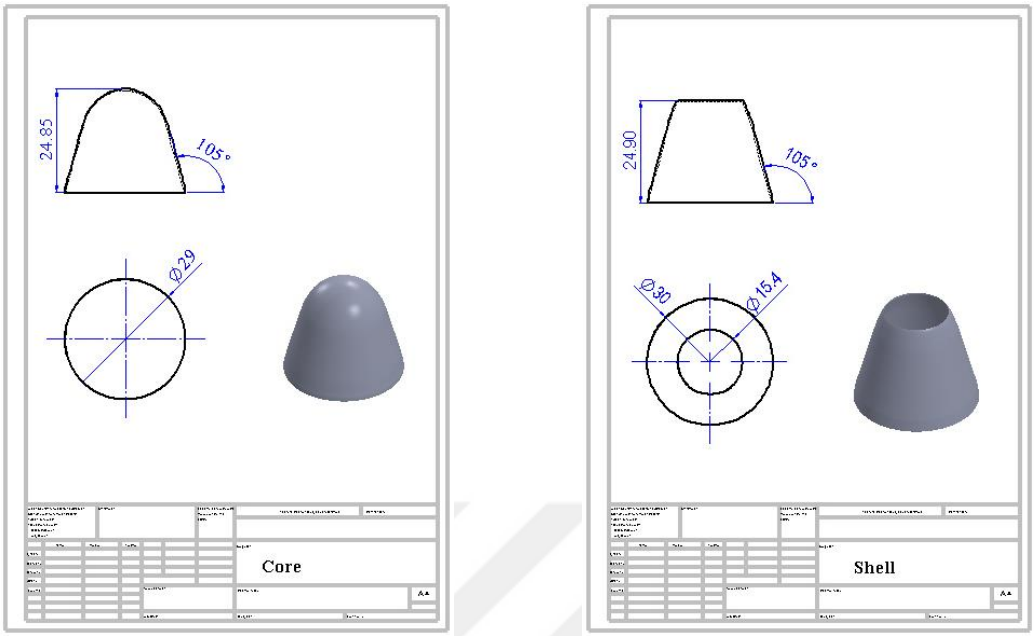

Figure 3.5. Technical drawings (mm) of (a) the inner core and (b) the outer shell.

The lower parts of both components were trimmed by the trimming tool since inhomogeneous elongation occurred in the skirt region of the geometries. The trimming operation was also performed for the upper region of the outer shell geometry. Final states of inner core and outer shell structures at the end of each operation are as shown in Figure 3.6 and Figure 3.7.

(a) (b) (c)

Figure 3.6. Deep drawn stages of the inner core; (a) first, (b) second and (c) cutting.

(a) (b) (c)

Figure 3.7. Deep drawn stages of the outer shell; (a) first, (b) second and (c) cutting.

As seen in the figures above, a hemispherical portion of the inner core and the flat-top portion of the outer shell were formed in the first stage deep drawing process. In the second stage deep drawing, to obtain desired dimensions of the conical portions was aimed. Hence, the amount of plastic deformation in the first stage was limited since a lot of plastic deformation induced in the blank material cannot exceed failure strain.

Plastic deformation value in the specimen varies during the deep drawing. Due to the strain hardening high levels of plastic deformation occur in some regions of the specimen. As a result of the plastic deformation, the increase in the material strength values arises from strain hardening. This leads to high energy absorbing capacity for the thin walled structure.

As seen in Figure 3.8, nonlinear thickness distribution in the structures is observed throughout the length of a material due to the deep drawing. Thickness distribution measurement values were obtained from two randomly selected specimens and were measured using the Mitutoyo CMM (Coordinate Measuring Machine) device installed in CMS Jant Sanayii A.Ş. Geometrical measurements were made on the entire structures and thickness variations were determined. The resulting point cloud was modeled in three dimensions using a computer aided design (CAD) program. The top of the specimen was taken as a reference (0 mm) to calculate the distance of the points. The red lines in the graphs indicate the thickness of sheet metal, the blue lines point out the thickness distribution of the first randomly selected specimen, and the black lines show the second one. Thickness at the bottom of the inner core reached approximately 0.49 mm whereas this quantity throughout the end of the hemispherical cap of the inner core thinned about 0.35 mm. A similar situation applies to the outer shell. Measurement at the top of the frusto-conical shell was 0.25 mm while thickness value was about 0.5 mm at the bottom of this geometry. As seen in the figures below, the thickness distribution of the first specimens of inner core and outer shell geometries are quite compatible with the second specimens.

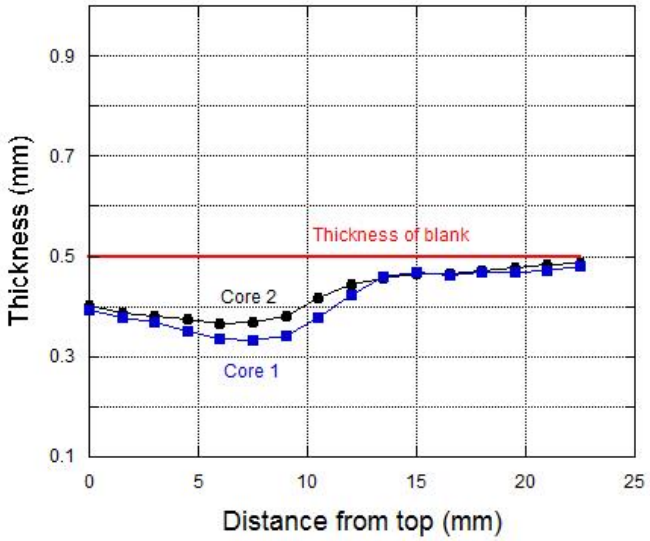

(a)

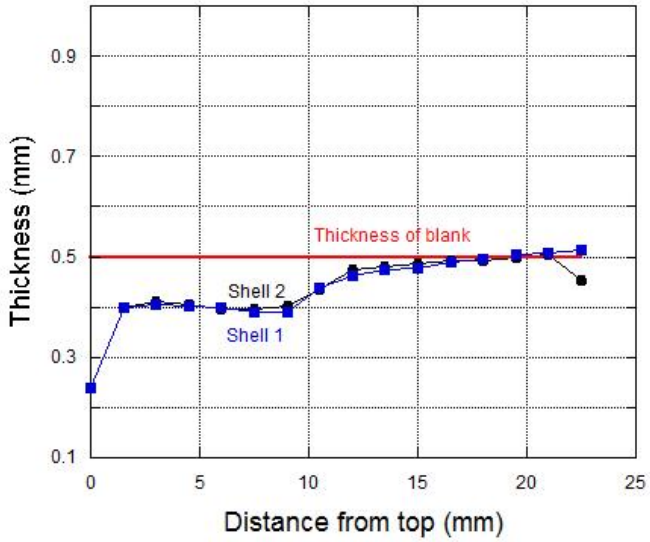

(b)

Figure 3.8. Thickness distribution of (a) the inner core and (b) the outer shell.

3.2 Material Characterization

The characterization of the material properties is a comprehensive behavior since to select the suitable material models and the accurate determination of material parameters will directly affect the success of the numerical work to be carried out. Additionally, the strain rate sensitivity of the materials should be taken into consideration in numerical studies due to the fact that the materials will be exposed to dynamic loads. For this reason, the material characterization was a very detailed study

including both the strength model and the damage parameter determinations. Therefore, the material characterization tests of AISI 304L stainless steel and polyurethane foam were conducted at both quasi-static and dynamic strain rates.

3.2.1 Material Characterization and Material Model Selection of AISI 304L Stainless Steel Material

Testing machines are fundamental to determine the properties of materials and their deformation behavior since it is important to know that the machines are strong and rigid enough to withstand the loads to be applied. One of the most preferred methods in mechanical characterization is a tensile test. The main purpose of tension test is to obtain a stress-strain curve to determine the major parameters belonging to material such as yield strength, elastic modulus and failure strain. One of the points to be noted in quasi-static tension test is the preparation of a proper test specimen to place between the jaws of the test machine to be used. Tensile specimens are created according to the standards from the material to be produced of the geometries and the cross section of the specimens can be a form of square, rectangular or round.

Shimadzu universal testing machine was used in accord with ASTM E8M-04 at quasi-static strain rates (10^{-3} s^{-1}, 10^{-2} s^{-1} and 10^{-1} s^{-1}). Shimadzu universal testing machine and the quasi-static test specimens used in this study are seen in Figure 3.9, respectively.

(a)

Figure 3.9. (a) Shimadzu universal testing machine and (b) the quasi-static test specimens.

(cont. on next page)

(b)

Figure 3.9. (cont.)

The strain-stress curves of AISI 304L stainless steel material at different quasi-static strain rates (10^{-3} s^{-1}, 10^{-2} s^{-1} and 10^{-1} s^{-1}) are presented in Figure 3.10.

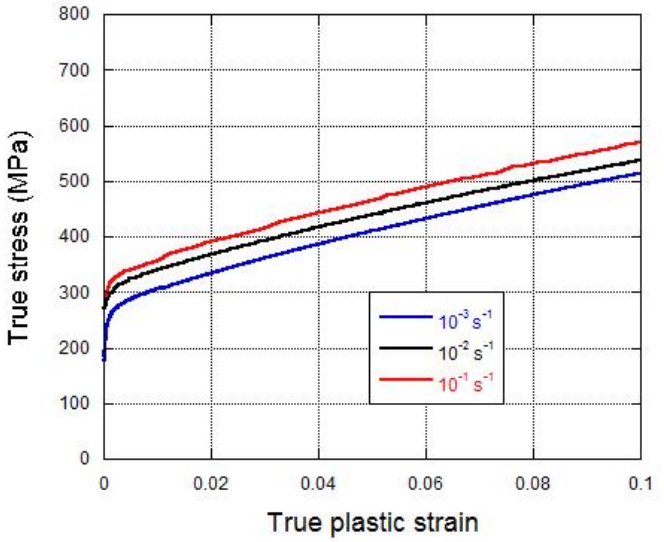

Figure 3.10. Quasi static true plastic strain-true stress curves of AISI 304L stainless steel.

Materials used in protection systems undergo high strain rate deformations such as crushing events, explosions and penetrations. Therefore, Split Hopkinson Tension Bar (SHTB) which is one of the most advanced methods developed for high strain rate material testing is used to determine the material properties under the dynamic loadings. Hence, after the quasi-static tests were completed, tension tests at different dynamic strain rates were conducted. The SHTB test setup and relevant test coupons are given in Figure 3.11.

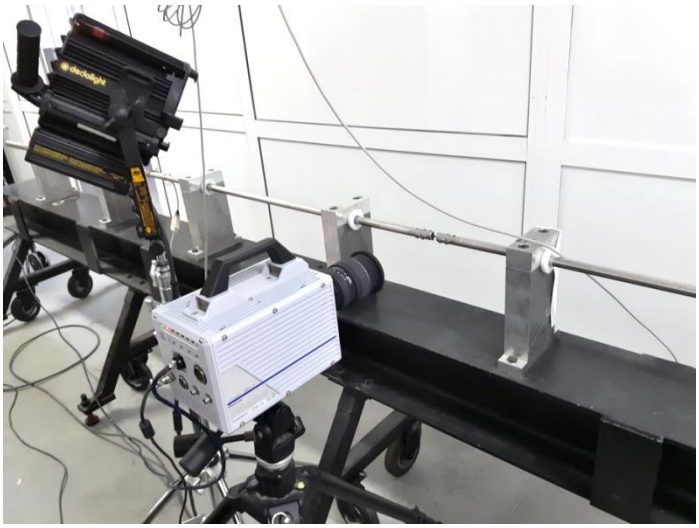

(a)

(b)

Figure 3.11. (a) SHTB test setup and (b) SHTB test specimens.

A typical example of voltage history obtained from SHTB test of AISI 304L stainless steel using an oscilloscope is given in Figure 3.12. Besides, each conducted tests was recorded by Photron Fastcam high-speed camera. An example of high-speed camera images and a strain-stress curve of AISI 304L stainless is shown in Figure 3.13.

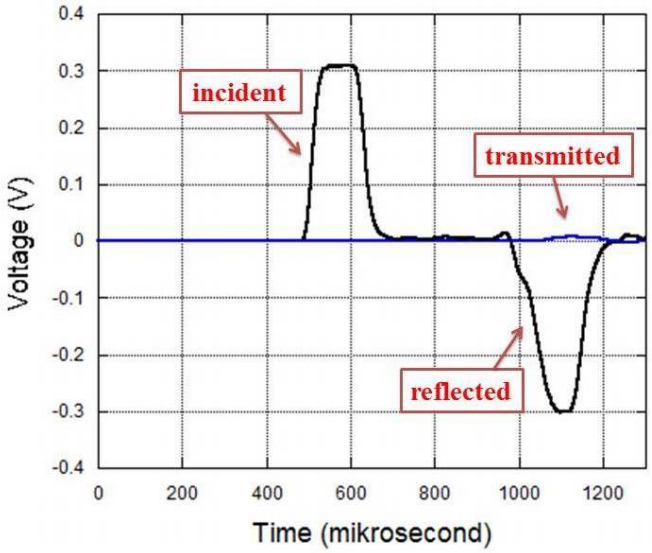

Figure 3.12. A typical SHTB test result.

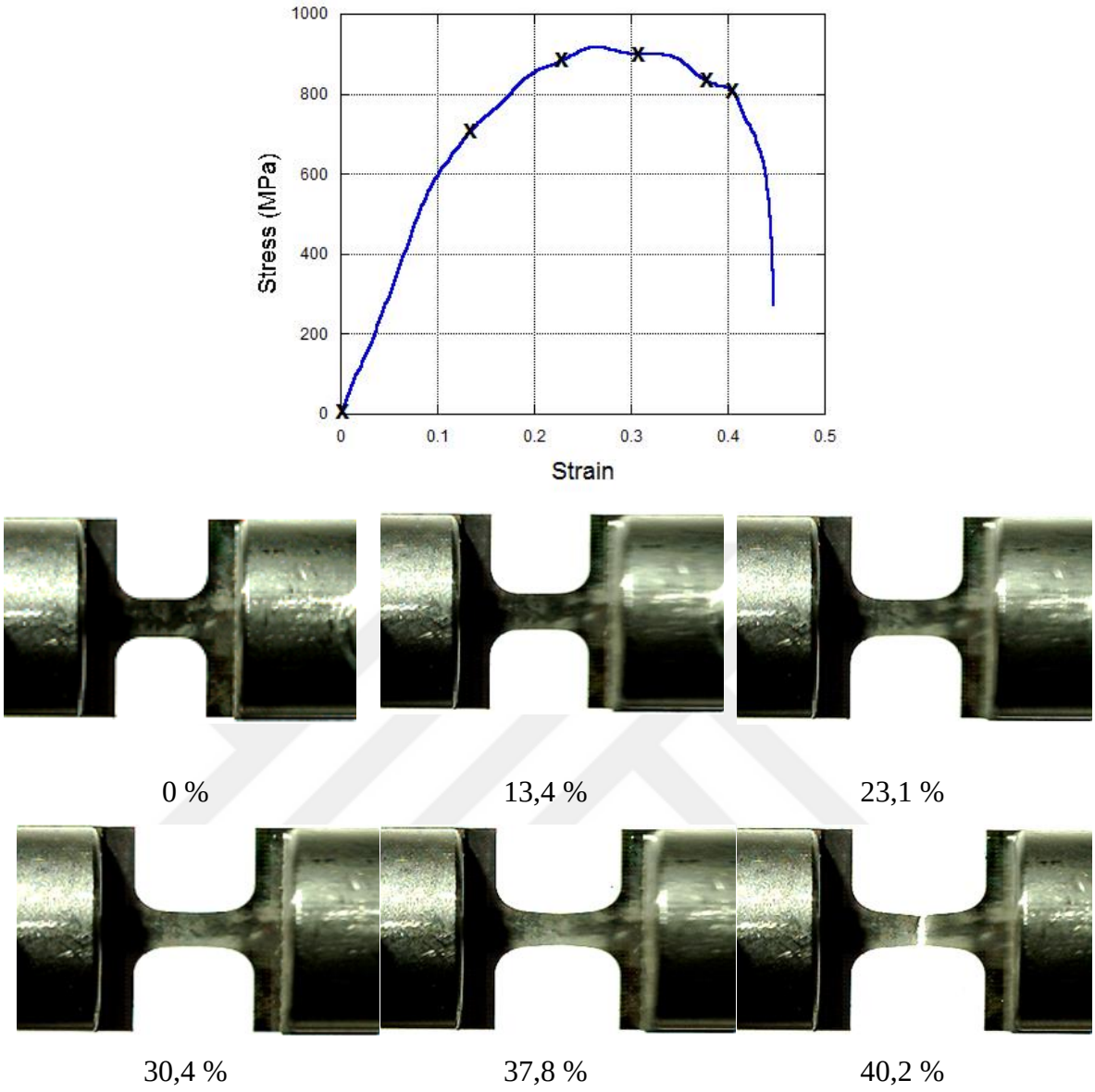

Figure 3.13. SHTB test and high speed camera images of AISI 304L stainless steel.

Split Hopkinson Tension Bar (SHTB) experiments were carried out at different dynamic strain rates (1580 s^{-1} and 2235 s^{-1}) and true plastic strain-stress curves of these experiments are presented in Figure 3.14.

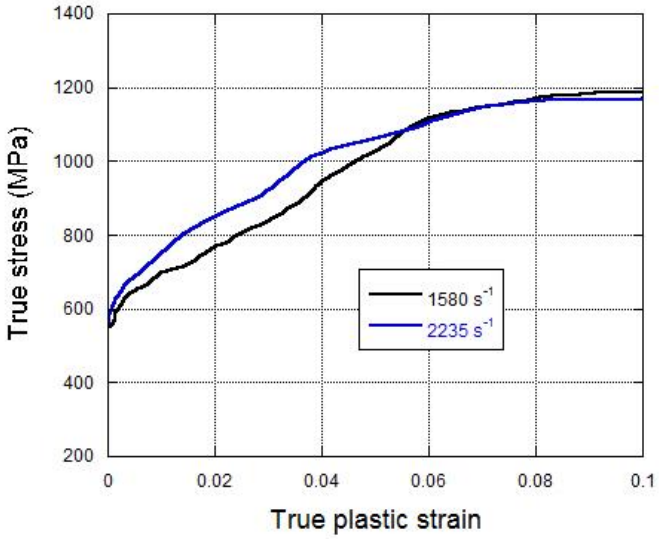

Figure 3.14. Dynamic true plastic strain-true stress curves of the stainless steel.

Thanks to data acquisition system, mechanical properties of materials are not only obtainable but also they are computable using some equations. These equations using for transforming voltage-time curves to strain-stress curves at the SHTB tests are as given below. Using the Equation 3.1 voltage vs. time data, V(t), can be converted to strain vs. time data, ™(t). In this equation, GF refers to gage factor, K_{gain} is the gain and V_{exc} represents the excitation number.

$$\varepsilon(t) = \frac{4 \times V(t)}{GF \times K_{gain} \times V_{exc}} \tag{3.1}$$

The strain of the specimen is calculated using the Equation 3.2.

$$\varepsilon_s(t) = -2\frac{C_b}{L_s}\int_0^t \varepsilon_r dt \tag{3.2}$$

In Equation 3.2, C_b represents the elastic wave speed of the bar while L_s symbolizes the length of the specimen. Besides, the stress in the specimen is given by Equation 3.3.

$$\sigma_s(t) = \frac{E_b \times A_b \times \varepsilon_t}{A_s} \tag{3.3}$$

where E_b, A_b, ™$_t$ and A_s are the elastic modulus of the bar, cross-section area of the bar, the cross-section area of the specimen and transmitted strain history of the bar, respectively.

To sum up, data picked up from the SHTB test by acquisition system was in the form of time vs. voltage as exemplified in Figure 3.12. By means of above transformation equations, collected data were converted to strain vs. stress curves in order to determine the material properties of the specimen at the high strain rate deformations as mentioned before.

As can be seen from the previously presented figures, AISI 304L stainless steel shows high strain rate sensitivity and it is necessary to take account of the material model to be used in the numerical modelling. Thus, the Johnson-Cook material model which captures the strain hardening, strain rate effect and thermal effect was selected so as to determine the mechanical behavior of the material. In LS-DYNA, *MAT_SIMPLIFIED_JOHNSON_COOK and *MAT_JOHNSON_COOK material models were used respectively in static and dynamic numerical models for modelling AISI 304L stainless steel. The Johnson-Cook flow stress equation is as follows:

$$\sigma = [A + B\varepsilon^n\,][1 + Cln(\frac{\dot{\varepsilon}}{\dot{\varepsilon}_0})][1 - (T^*)^m] \tag{3.4}$$

$$T^* = \frac{T - T_r}{T_m - T_r} \tag{3.5}$$

where A is the yield stress of the material, B is the hardening modulus, n is the work-hardening exponent, C is the non-dimensional strain rate sensitivity, ™ is the equivalent plastic strain, $\dot{\varepsilon}$ is the plastic strain rate, $\dot{\varepsilon}_0$ is the reference plastic strain rate, m is the thermal softening effect, T is the effective temperature, T_r is room temperature and T_m is the melting temperature of the material.

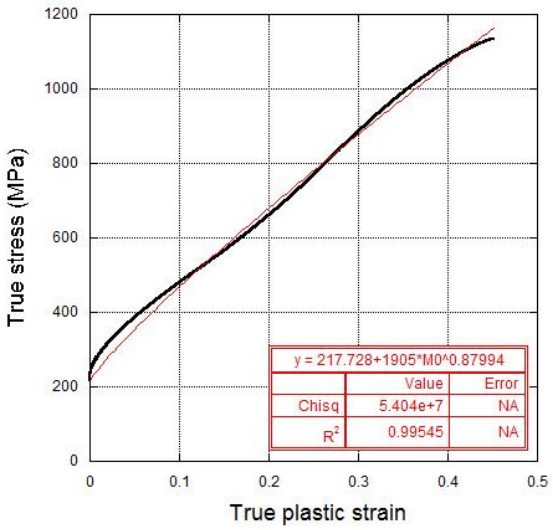

Figure 3.15. Determination of A, B and n parameters of Johnson-Cook material model.

It is obviously seen from Figure 3.10 and Figure 3.14, AISI 304L stainless steel shows strain rate sensitivity. Thus, tension tests at different strain rates were fitted to determine parameters of material model in the first bracket of Johnson Cook material model. As seen in Figure 3.15, the characterization result is quite successful. Furthermore, C parameter which symbolizes strain rate sensitivity was found out as seen in Figure 3.16.

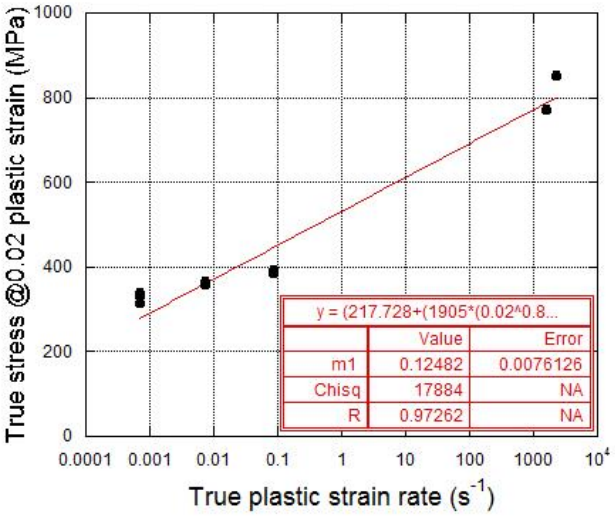

Figure 3.16. Strain rate sensitivity of the material (C parameter).

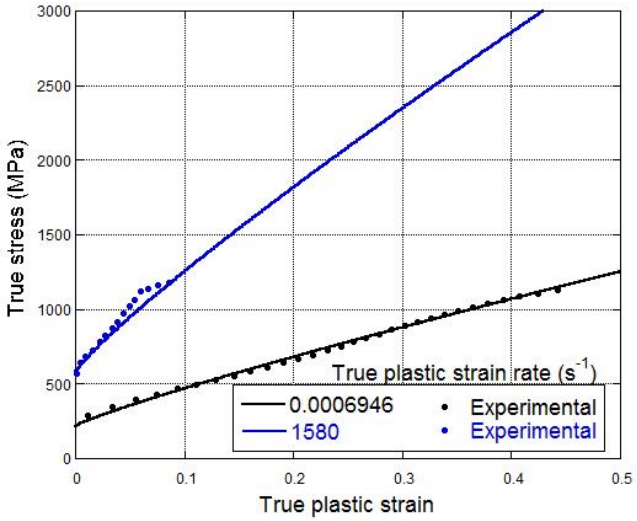

Figure 3.17. Johnson Cook material model results and experimental results.

In Figure 3.17, comparison of Johnson-Cook material model and performed tests for characterization at different strain rates of AISI 304L stainless steel is given.

In the current study, Johnson-Cook damage model was also used to determine the failure strain. Strain at fracture was modelled using the Equation 3.6.

$$\varepsilon_f = \left[D_1 + D_2 e^{D_3 \sigma^*}\right]\left[1 + D_4 \, ln\left(\frac{\dot{\varepsilon}}{\dot{\varepsilon}_0}\right)\right](1 + D_5 T^*) \tag{3.6}$$

where D_1, D_2, D_3, D_4 and D_5 are failure parameters and $\sigma^* = \frac{\sigma_m}{\sigma_e}$ represents the stress triaxiality ratio. D_1 symbolizes the failure strain at the lowest strain rate. The parameters related with stress triaxiality were not considered as the stress state does not change highly during crushing. Therefore, Johnson Cook damage model was in the form of considering strain rate sensitivity as in the Equation 3.7.

$$\varepsilon_f = D_1\left[1 + D_4 \, ln\left(\frac{\dot{\varepsilon}}{\dot{\varepsilon}_0}\right)\right] \tag{3.7}$$

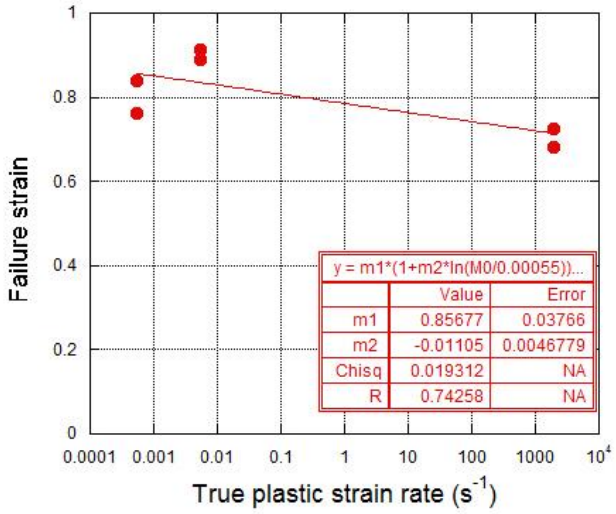

Figure 3.18. Failure parameters.

Material model parameters of AISI 304L stainless steel obtained using above equations were given in Table 3.1.

Table 3.1. Johnson-Cook material model parameters of AISI 304L stainless steel.

ρ (kg/m^3)	7830	**D1**	0.8567700
G (GPa)	80	**D2**	0
E (GPa)	193	**D3**	0
υ	0.305	**D4**	-0.0110500
A (MPa)	217.728	**D5**	0
B (MPa)	1905	**T_r (^{o}K)**	296
n	0.87994	**T_m (^{o}K)**	1698
C	0.12482	**m**	1.0

3.2.2 Material Characterization and Material Model Selection of Polyurethane Foam Material

As explained previous chapter, it is highly important to confine the structures externally or internally so as to improve the energy absorbing characteristic of the structure. Hence, the inner core structure was supported by filling with polyurethane foam so as to increase the energy absorbing capacity of the balanus geometry especially

during the dynamic deformation. The material characterization of the polyurethane foam was determined in order to use in numerical models to be explained in detail later.

In order to produce polyurethane foam specimen, FOAM IT-8 was used and *MAT_MODIFIED_CRUSHABLE_FOAM material model was chosen for modelling foam material in LS-DYNA since it accepts static and dynamic strain-stress curves as an input. The strain-stress curves for each strain rate were defined separately. Split Hopkinson Pressure Bar test setup was utilized for dynamic material characterization of polymeric foam material. During the Hopkinson Pressure Bar tests of materials having very low acoustic impedance such as foam, it is not possible to test this kind of materials with the classical SHPB. Because the signal transmitted from the specimen to the transmitter bar is at very low levels and the actual value of the signals falls into the existing noise scale in the signal. The dynamic stress balance (the differences between the forces acting on the front and back surfaces of the specimen) cannot be obtained from the beginning of the deformation to the proceeded deformation values during the test such material. Therefore piezo electric quartz crystals are placed on the specimen-bars interface. The acoustic impedance of these quartz crystals is very close to the 7075-T6 aluminum material used in the Hopkinson Bar where the tests are performed and the strain/stress measurement accuracy is very high. Thereby, characterization tests were carried out for polyurethane material using piezo electric quartz crystals.

A schematic drawing of the Split Hopkinson Pressure Bar test setup is shown in Figure 3.14. As seen in the figure, a gas gun, bar constituents consisting of a striker bar, an incident bar and a transmitter bar, data acquisition system and record system are major parts of SHPB test setup. In this compression test setup, all bars are made of the same material with the same cross section area. Furthermore, the test speimen is interposed with incident and transmitter bars. Then the system is loaded by gas gun. After the system is loaded, striker bar is fired by gas gun and is pushed forward to the incident bar. Moreover, the first movement results in a compressive elastic wave which propagates in the incident bar towards the specimen. When the elastic wave reaches the specimen, test specimen starts to deform plastically. After the damage of the specimen, a part of wave proceeds to propagate along with transmitter bar and it is called as transmitted pulse whereas another part of wave turns back to the incident bar and it is called as reflected pulse. Data corresponding to the pulses is gathered by strain gages

mounted on related bars at the same distance away from the test specimen as voltage using oscilloscope and signal conditioner.

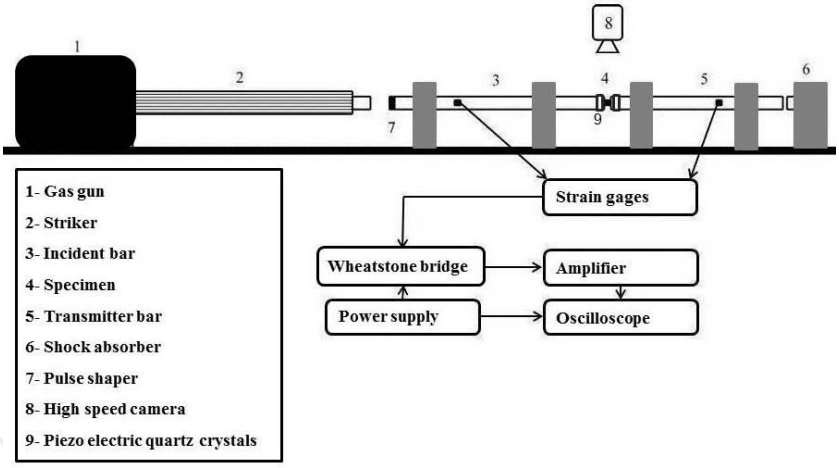

Figure 3.19. Modified SHPB.

Quasi-static and Split Hopkinson Pressure Bar compression test specimens were prepared in a cylindrical shape with approximately 312.5 mg weight, 9.2 mm length and 18 mm diameter. From these quantities, the density of polyurethane foam material was determined as 0.1335 g/cm^3.

Quasi-static and dynamic strain-stress curves of the foam material are given in Figure 3.20. These curves are used as input data for the relevant material model. As expected from the foam material, it is a strain rate sensitive material.

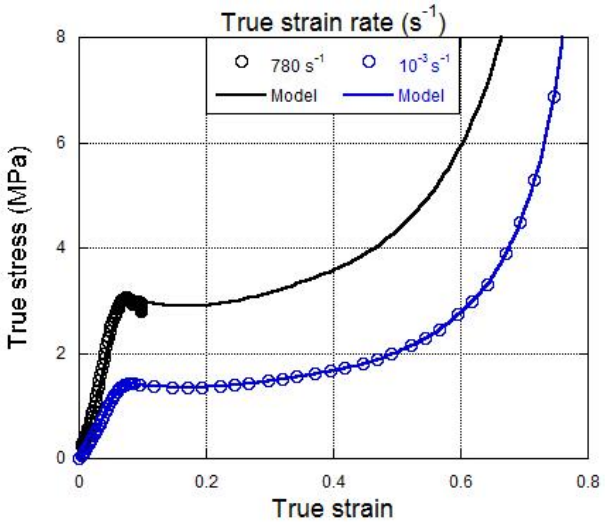

Figure 3.20. Static and dynamic compression strain-stress curves of polyurethane foam material.

To investigate the dynamic deformation history of the foam material, the conducted tests were recorded by a high speed camera (Figure 3.21). After about 25 percent deformation, material damage occurred. This behavior can be modeled with the material model to be used for the foam material.

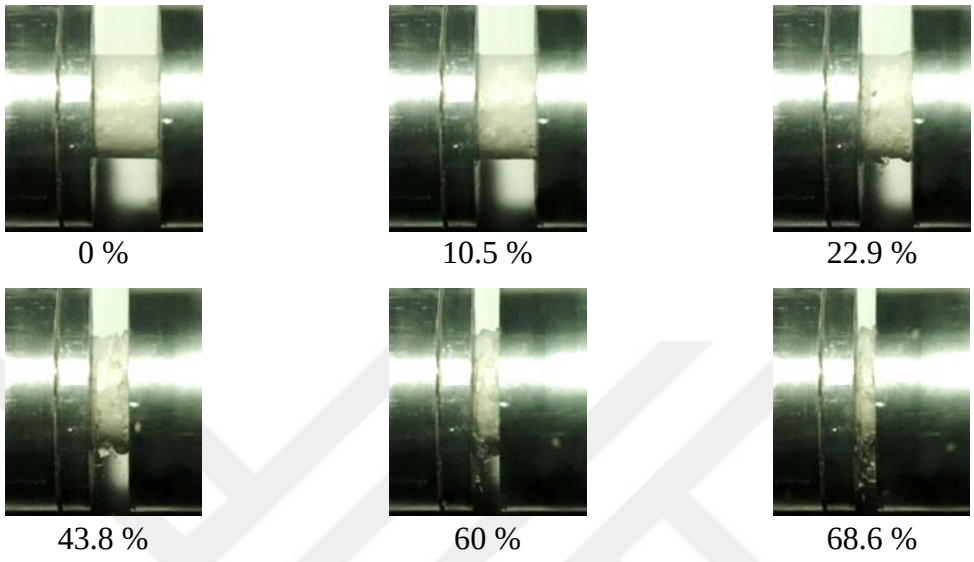

Figure 3.21. The dynamic deformation history of polyurethane foam.

Material model parameters of polyurethane foam obtained using conducted tests are given in Table 3.2.

Table 3.2. Material model parameters of polyurethane foam used in numerical models.

ρ (kg/m^3)	**E (GPa)**	**υ**
133.5	0.024444	0.01

3.3 Testing Methods

In the present study, two different experiment setups were used for investigation of crushing behavior of the structures at various strain rates. Shimadzu AG-X universal testing machine having maximum 300 kN capacity was used for quasi-static crushing experiments whereas Fractovis Plus drop weight tower was used for low-velocity impact tests. The aims of the experiments are to investigate the strain rate sensitivity of

the stainless steel used in the production of the geometries and determination of the energy absorbing performance of the structures under different loadings.

3.3.1 Quasi-static Compression Tests

Shimadzu AG-X universal testing machine is seen in Figure 3.22. The device was equipped with cross heads and a video extensometer. A video extensometer was used to remove the errors in stroke values stemmed from the elastic deformations of the device. Moreover, deformation histories of experiments were recorded by camera. Quasi-static experiments can be performed at between strain rates of 10^{-4} s^{-1} and 10^{0} s^{-1}. In order to conduct an experiment at quasi-static strain rates, specimens are sandwiched between the cross heads of the machine. One of these heads is a bottom rigid plate and it is fully constrained. The other is top rigid plate moving with various constant crushing velocities. Constant velocities at targeted strain rates can be determined using the Equation 3.8.

$$\dot{\varepsilon} = \frac{V}{l} \tag{3.8}$$

where $\dot{\varepsilon}$ is the strain rate, V is the constant velocity of the top plate and l is the length of the specimen.

Figure 3.22. Shimadzu AG-X universal testing machine.

3.3.2 Drop Weight Tests

Compression tests under low-velocity impact loading were performed using Fractovis Plus drop weight test machine so as to determine the crushing behavior of the specimens at dynamic strain rates. Low-velocity impact tests can be carried out at between strain rates of 10^0 s^{-1} and 10^2 s^{-1} with the machine. The device was equipped with a tube holder for extra dropping weights which provide targeted kinetic energy, a striker having 222 kN maximum force capacity, a flat striker tip having 70 mm, a velocity sensor to determining the impact velocity of diameter and a stationary rigid bottom plate to place a specimen on it. Besides, the compression springs of the system were used to supply higher kinetic energy when extra dropping weights were inadequate for the targeted kinetic energy value with free fall of the weights. Deformation histories of dynamic crushing tests were saved by Photron Fastcam high-speed camera. Data related to the experiments were recorded by data acquisition system (DAS) in terms of time, displacement, force and energy.

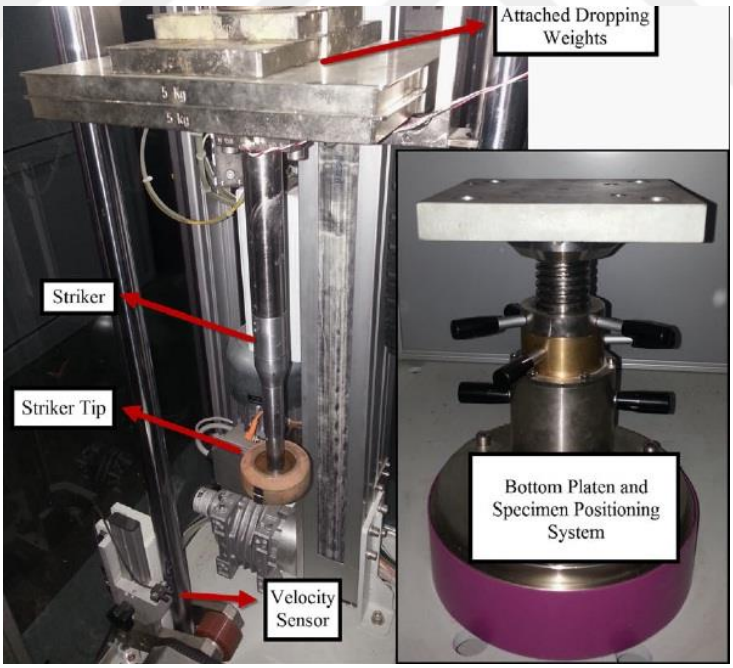

Figure 3.23. Fractovis Plus drop weight testing machine (Source: Tasdemirci et al., 2015).

CHAPTER 4

NUMERICAL STUDIES

Numerical analysis is commonly used to understand and validate the effects of the material parameters in order to obtain well-optimized system. Therefore, finite element analysis (FEA) was utilized to develop the efficiency of the balanus structure as a bio-inspired energy absorber under static and dynamic loadings. FEA is a technique which considers the solution of boundary value problems and partial differential equations to solve the engineering problems. In the present research, LS-DYNA 971 was used as a commercial explicit finite element analysis program to simulate the conducted experiments.

Before the simulations of the experiments, three different numerical outer shell geometries were modeled in order to determine the appropriate numerical model. Therefore, deep drawing process was modeled using blank material consisting of shell elements to obtain the first specimen having residual stress/strain and non-linear thickness distribution. The second numerical outer shell specimen is also obtained from deep drawing but it includes only non-linear thickness distribution and the effect of residual stress/strain was not considered. The third outer shell specimen was modeled with a constant thickness of 0.5 mm. As seen in Figure 4.1, there is a good agreement between experimental result and the first numerical specimen result due to the similarity between manufacturing and crushing conditions. The force-displacement curve of the first specimen also describes that residual stress/strain and the non-linear thickness distribution must be implemented in the numerical models in order to obtain correlated results with experimental results. Thanks to the forming process, it was also observed that the crushing response of the first specimen increased when compared with the others. The remaining numerical specimens having not the effects stemming from the forming process could not show the crushing response as effective as the first one.

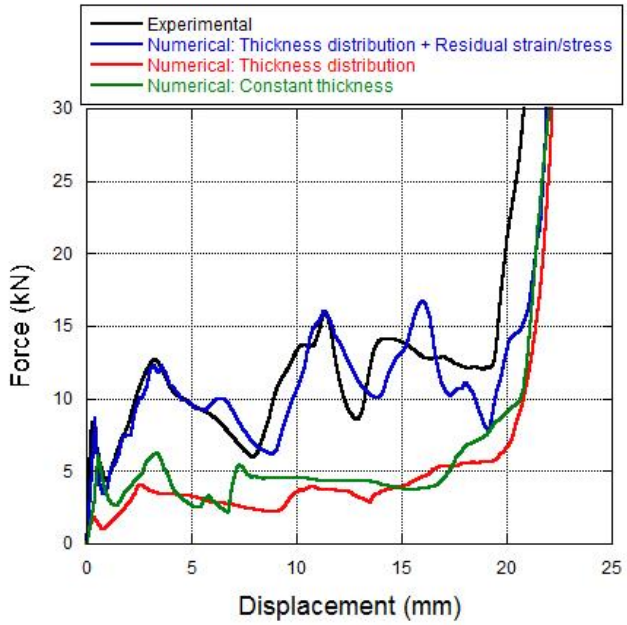

Figure 4.1. Forming effects on crushing behavior of outer shell geometry.

4.1 Deep Drawing Simulations

After the describing the importance of the numerical deep drawing simulation with the comparisons, appropriate deep drawing parts were created for both geometries. In the current study, deep drawing process involved two stages for each geometry. Components of a deep drawing numerical model are as seen in Figure 4.2. All components were modelled with Belytschko-Tsay element formulation having five integration point. In deep drawing, blank holder and punch were constrained along the radial direction and so did rotations. The die was also constrained to move all directions. Blank was placed between the blank holder and die and the punch moved through the die cavity to give a shape to the blank material.

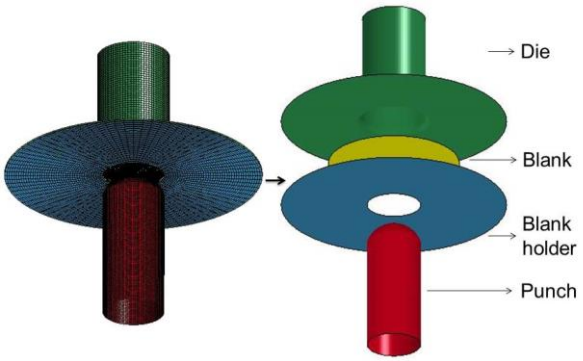

Figure 4.2. Deep drawing model.

In the numerical deep drawing process, drawing parts were assumed to be rigid except blank material. However, the blank material was modelled selecting Johnson-Cook material model. Moreover, boundary prescribed motion rigid card was used to define velocity curve in order to give a movement to the punch.

The importance of residual strain/stress and thickness change was mentioned before. Therefore, the interface spring back lsdyna thickness card was activated in numerical deep drawing model since this card allowed obtaining drawn part by generating a dynain file which included the all deep drawing effects. The second stage of deep drawing and trimming operation of inner core material are shown in Figure 4.3.

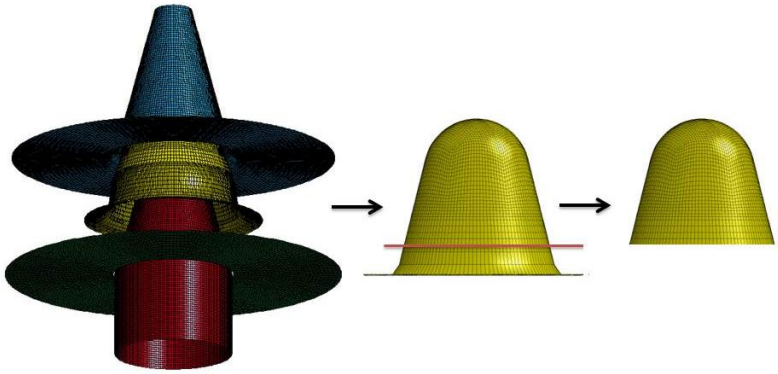

Figure 4.3. Deep drawing and trimming operation.

4.2 Crushing Simulations

In order to investigate and determine the static and dynamic crushing behavior of geometries in detail, conducted experiments were simulated. Numerical models of the static and dynamic crushing tests consist of three main parts. These are a moving top head, a specimen and a fixed bottom plate. As a specimen numerically trimmed inner core, outer shell or balanus geometries was imported into the simulations as a specimen. In Figure 4.4, a numerical model with balanus geometry is seen.

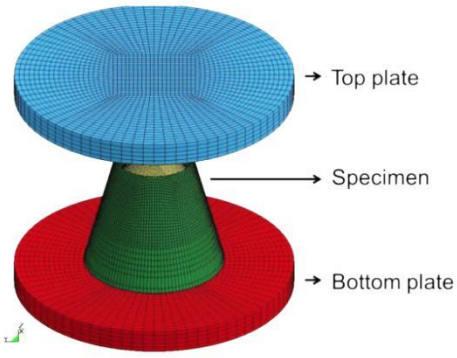

Figure 4.4. Crushing model.

The cross heads were created using butterfly block mesh and were modelled as a rigid material. Moreover, the rigid top head was unconstrained to move only in-plane direction and constrained for all rotations whereas the rigid bottom plate was constrained to move all directions.

In the static crushing numerical models, a time-dependent displacement curve was defined for the moving top head and mass scaling method was used. In this method, the density of the specimen was reduced and the crushing speed was increased. The principal purpose here is to protect the solution time of the static crushing model at the acceptable limit in LS-DYNA. When mass scaling was performed, the internal energy and kinetic energy histories of the specimens were recorded in the numerical model and the ratio between them remained about only 5 percent. However, an initial velocity was given to the moving top head and the drop weight masses used in the experiments was defined as the total weight of the top head in the dynamic crushing (drop weight) numerical models. In addition, the contacts consisting of the folds formation and the failure within the specimens were taken into consideration with the single surface contact algorithm in the both models. In the numerical model of both tests, the contact between the specimen and the plates is defined with the surface to surface contact algorithm. The static and dynamic friction coefficients between the specimen and the plates were taken as 0.3 and 0.2, respectively. In addition, the static and dynamic crushing simulations were modeled using foam filled inner core and balanus specimens. Therefore, foam material was generated as a solid material in a finite element software and all contact relations were also applied when the foam filled specimen was used. Experimentally obtained strain-stress curves of the foam material were used as input information for the relevant material model. Crushing numerical model of foam filled balanus is seen in Figure 4.5.

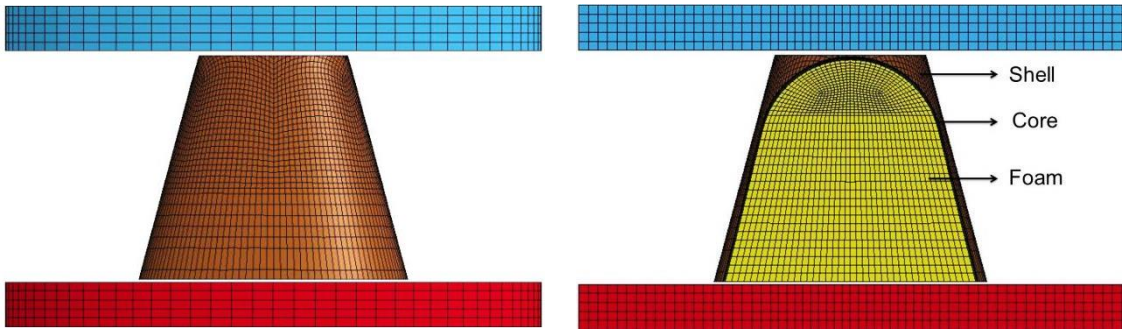

Figure 4.5. Crushing numerical model of foam filled balanus.

As is known, balanus geometry consists of an outer shell structure and an inner core structure and they interact with each other during the crushing. It is possible to get more detailed information from numerical models to well understand this interaction since interaction may lead to energy partition between these parts at the static and dynamic strain rates. The interface pressure history of the inner core and the outer shell for different points was recorded in the numerical model. Since pressure value gives a direct insight into the interaction between the two components during deformation, numerical model results were compared in order to understand energy partition of the geometries at the different strain rates.

CHAPTER 5

RESULTS AND DISCUSSIONS

5.1 Numerical Approach of Deep Drawing

The deep drawing processes consisting of four major parts were modeled at two stages in order to generate the numerical inner core and outer shell specimens. During deep drawing, thickness variation of the blank depending on the punch displacements was observed. The thickness distributions are given for 0-15-20 and 24 mm of punch displacements for inner core specimen at the first stage of deep drawing in Figure 5.1. Fringe levels represent the thickness distributions of blank material only.

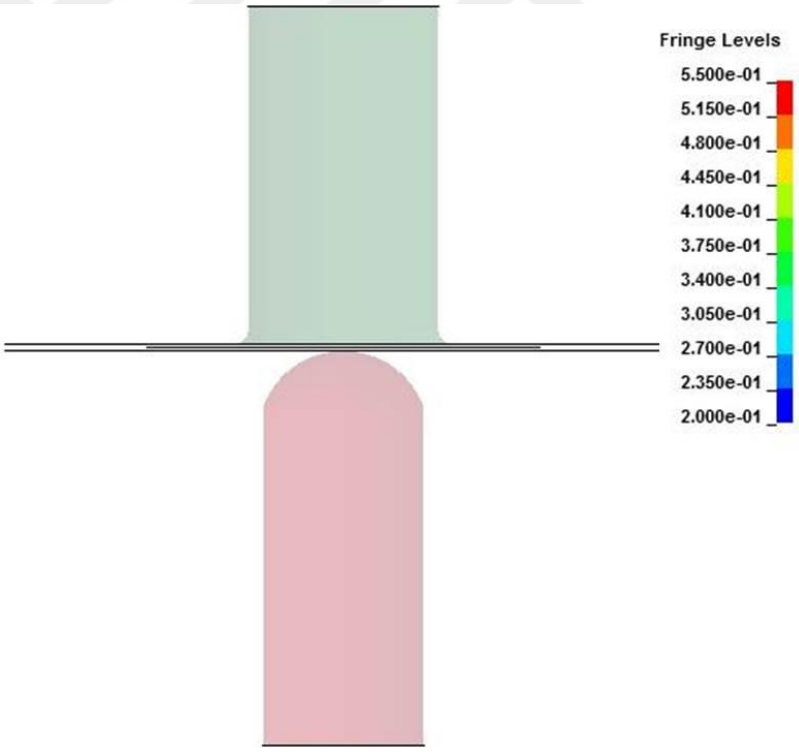

(a)

Figure 5.1. Thickness distributions of inner core specimen during the first stage deep drawing at (a) 0 mm, (b) 15 mm, (c) 20 mm and (d) 24 mm of punch displacements.

(cont. on next page)

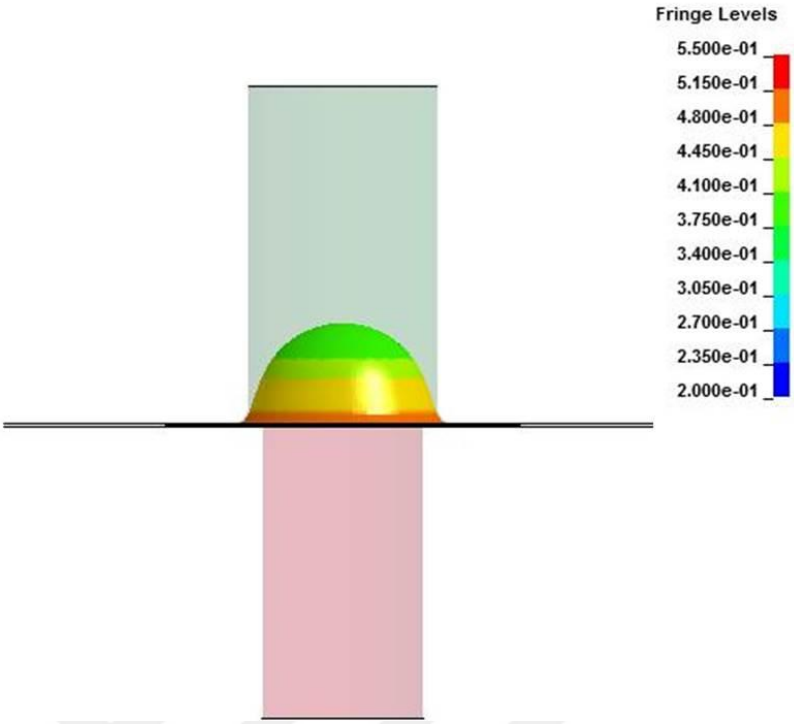

(b)

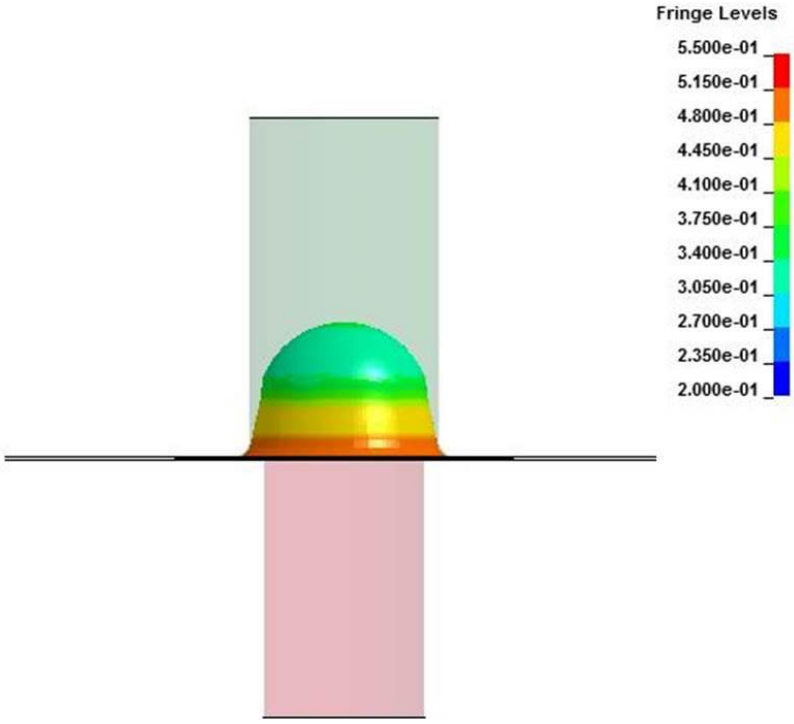

(c)

Figure 5.1. (cont.)

(cont. on next page)

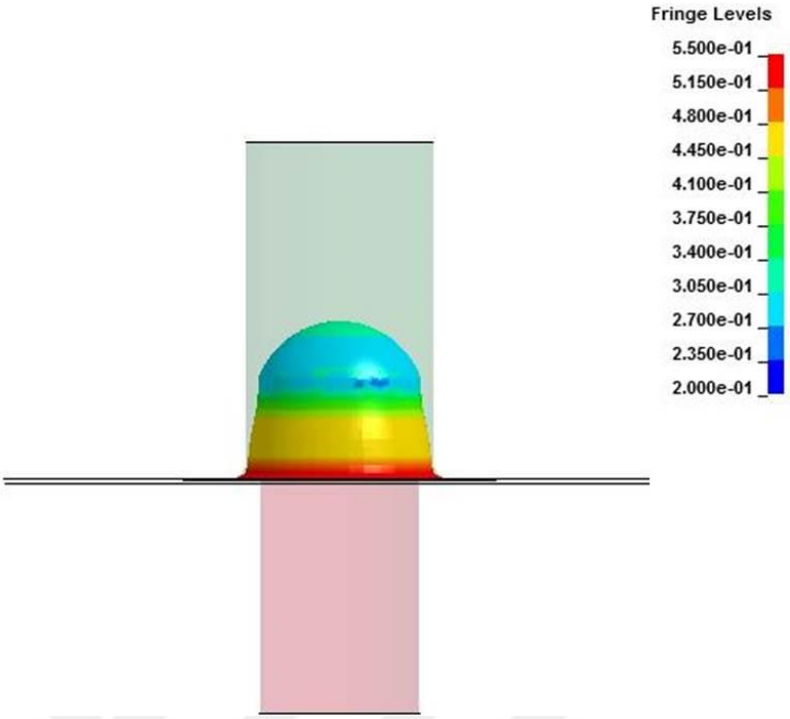

(d)

Figure 5.1. (cont.)

The thickness distributions are given for 24-26-28 and 30 mm of punch displacements for inner core specimen at the second stage of deep drawing in Figure 5.2.

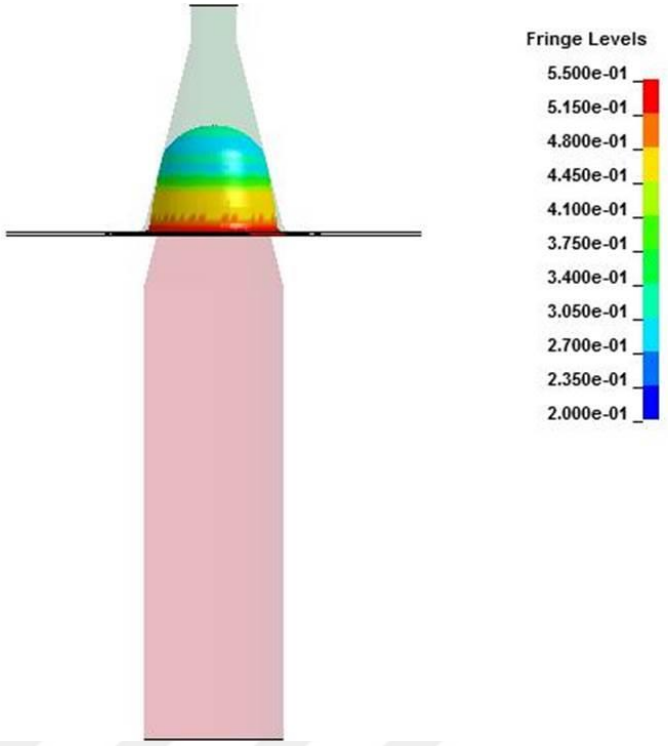

(a)

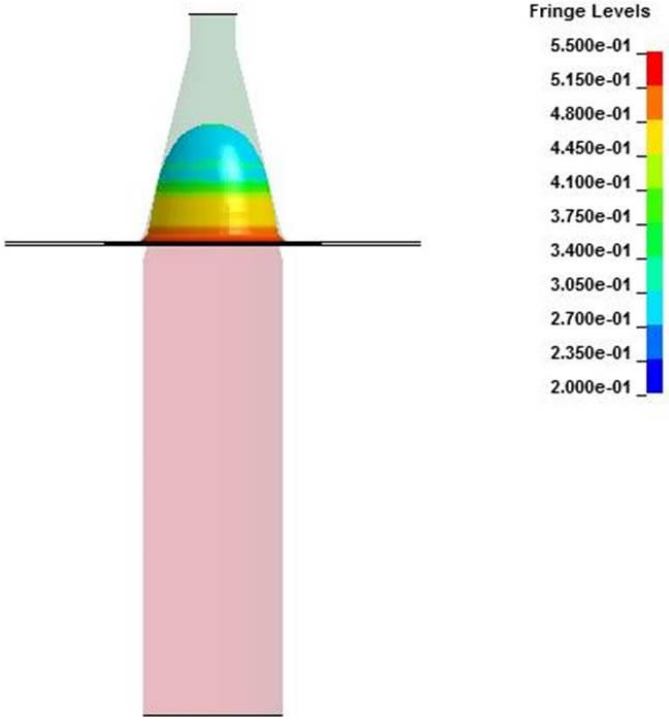

(b)

Figure 5.2. Thickness distributions of inner core specimen during the second stage deep drawing at (a) 24 mm, (b) 26 mm, (c) 28 mm and (d) 30 mm of punch displacements.

(cont. on next page)

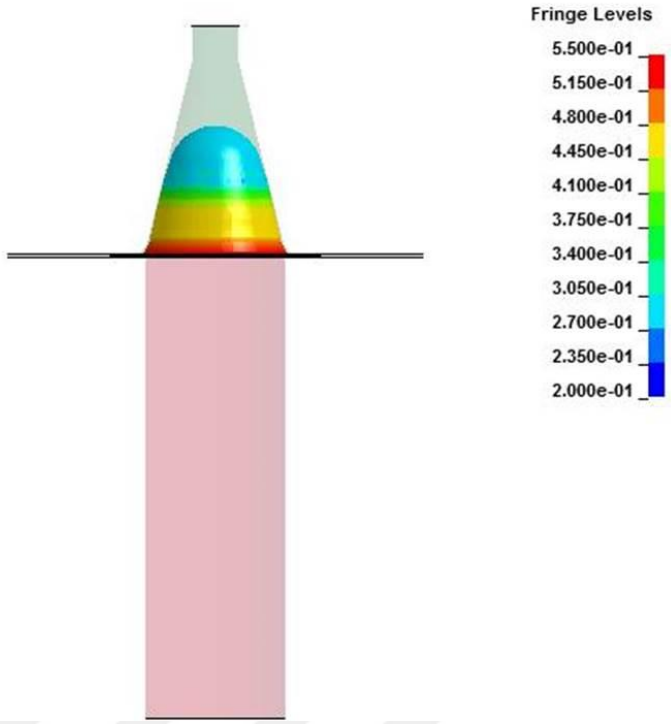

(c)

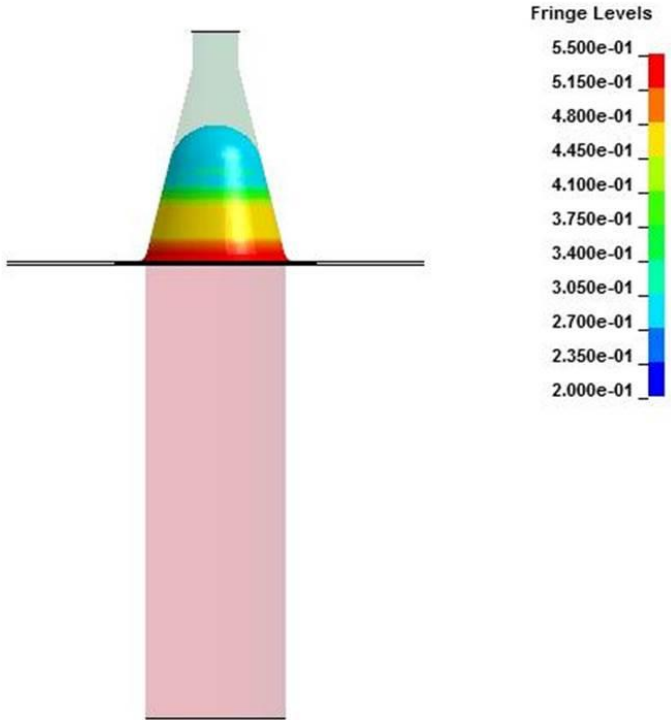

(d)

Figure 5.2. (cont.)

Similarly, the thickness distributions of outer shell geometry at the first stage of deep drawing are given for 0-15-20 and 24 mm of punch displacements in Figure 5.3.

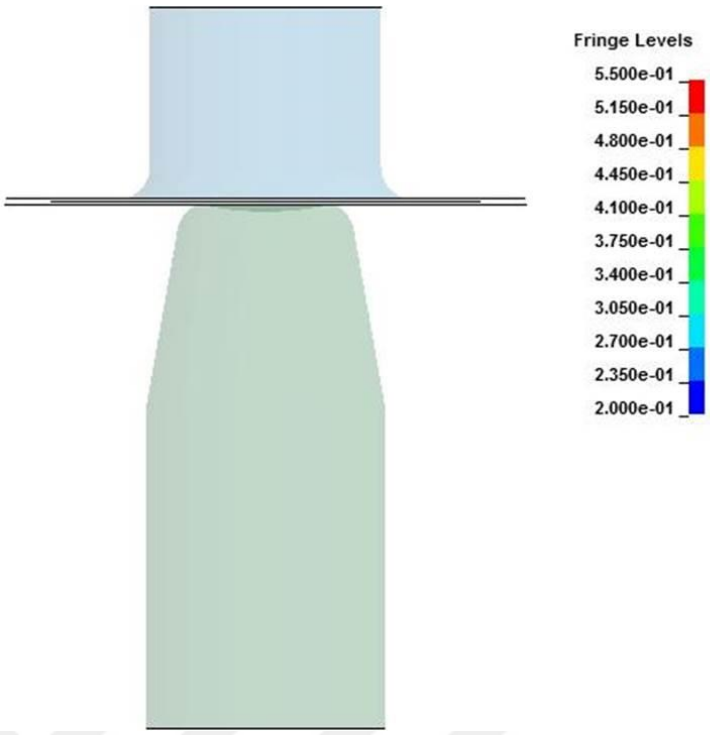

(a)

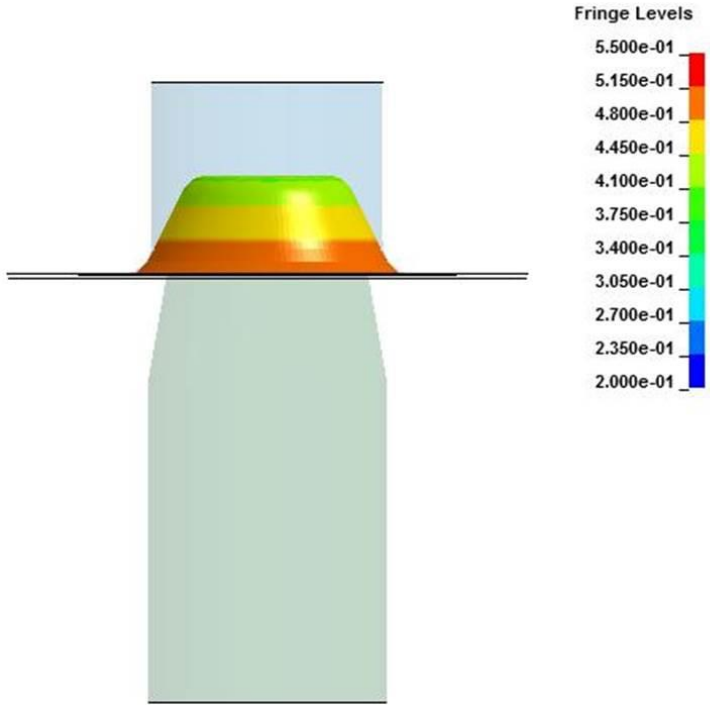

(b)

Figure 5.3. Thickness distributions of outer shell specimen during the first stage deep drawing at (a) 0 mm, (b) 15 mm, (c) 20 mm and (d) 24 mm of punch displacements.

(cont. on next page)

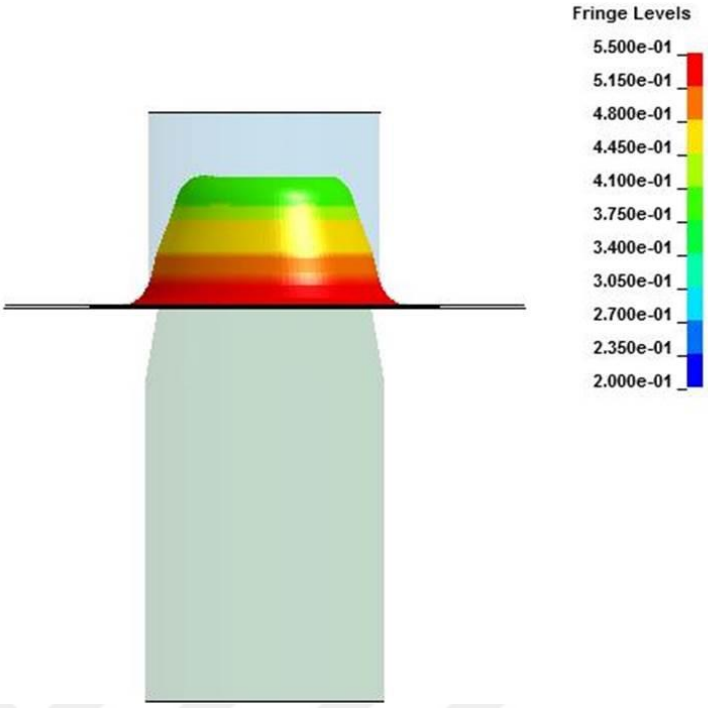

(c)

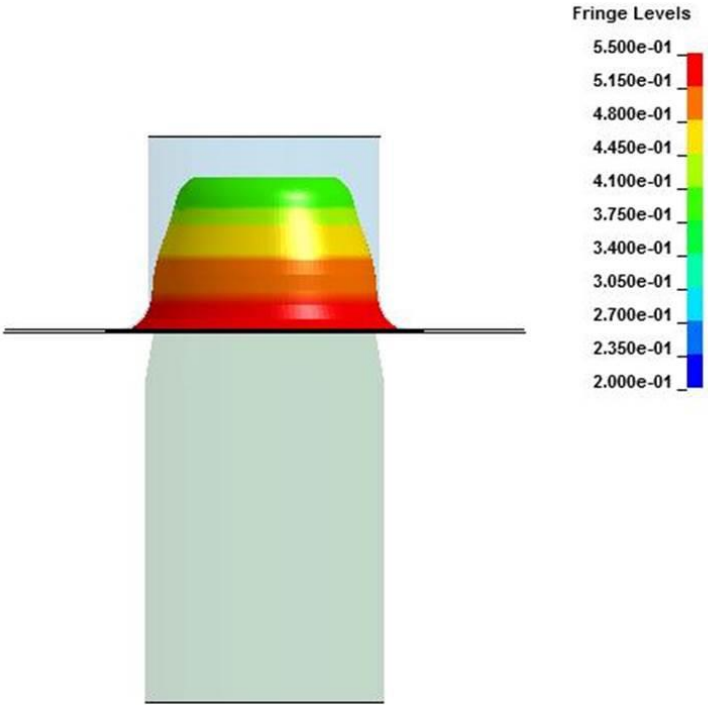

(d)

Figure 5.3. (cont.)

The thickness distributions are given for 24-28-30 and 33 mm of punch displacements for outer shell specimen at the second stage of deep drawing in Figure 5.4.

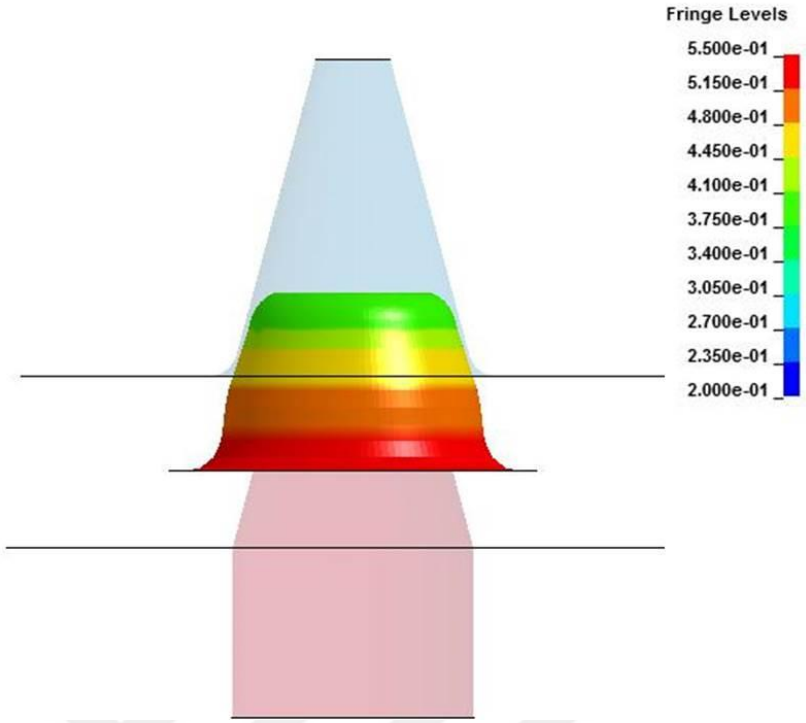

(a)

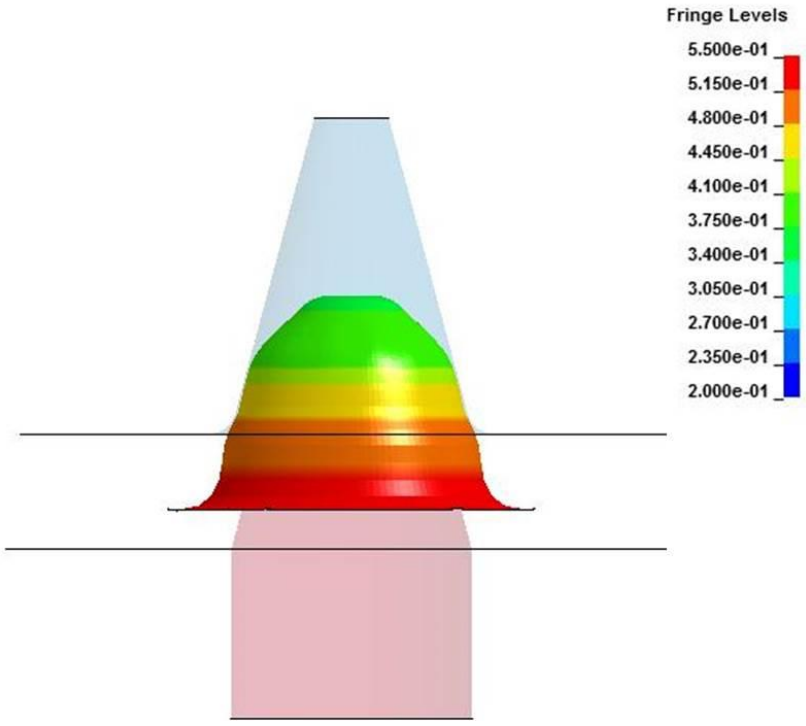

(b)

Figure 5.4. Thickness distributions of outer shell specimen during the second stage deep drawing at (a) 24 mm, (b) 28 mm, (c) 30 mm and (d) 33 mm of punch displacements.

(cont. on next page)

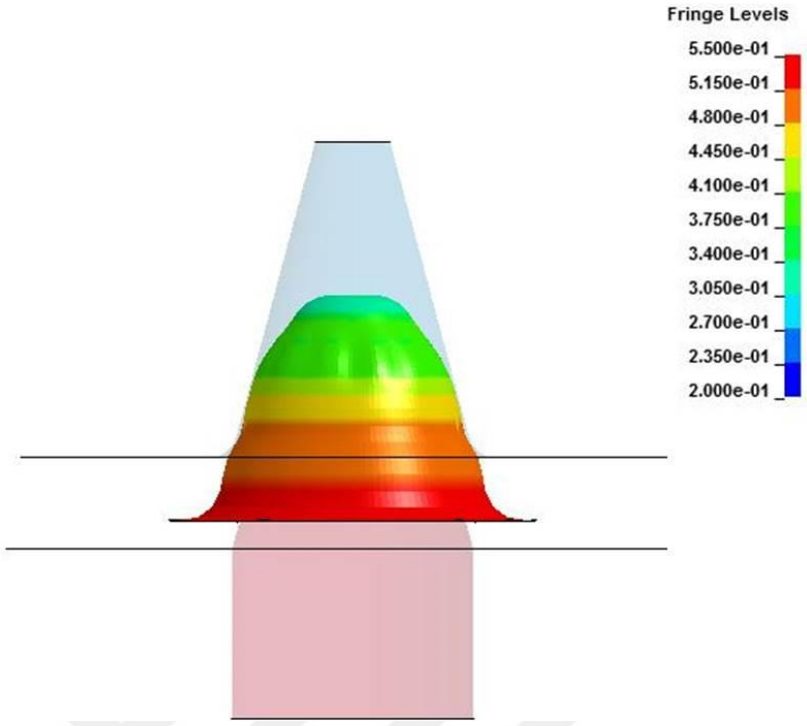

(c)

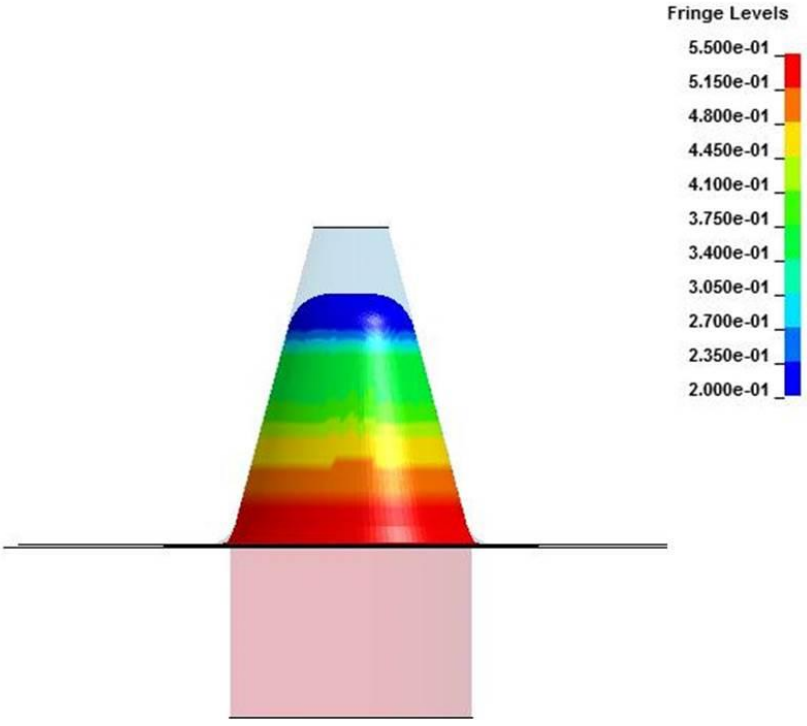

(d)

Figure 5.4. (cont.)

As seen in Figure 5.5 and Figure 5.6, there is a good agreement about thickness values and distributions between experimental and numerical results. These close thickness distributions of inner core and outer shell geometries will influence the sensitivity of the subsequent results of crushing analysis of the balanus geometries.

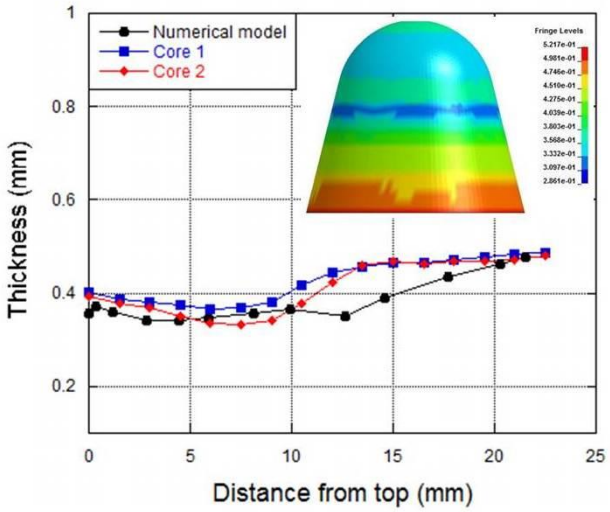

Figure 5.5. The thickness distribution of the inner core.

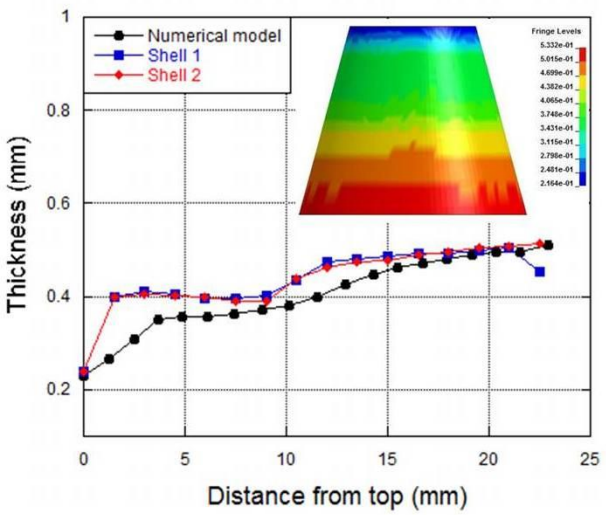

Figure 5.6. The thickness distribution of the outer shell.

5.2 Crushing Behavior of the Geometries

In the present study, the investigation of crushing behavior of the geometries started with quasi-static compression tests of the inner core, outer shell and balanus geometries. Shimadzu AG-X universal compression test machine which has 300 kN capacity was used for these tests. Quasi-static compression tests of inner core structures were first performed at 10^{-3} s^{-1}, 10^{-2} s^{-1} and 10^{-1} s^{-1} strain rates. Five specimens were tested for each strain rates. The experimental results clearly show that the deformation characteristic of the inner core is not influenced significantly depending on the quasi-static strain rate. The force-displacement curves of inner core structures are given in Figure 5.7.

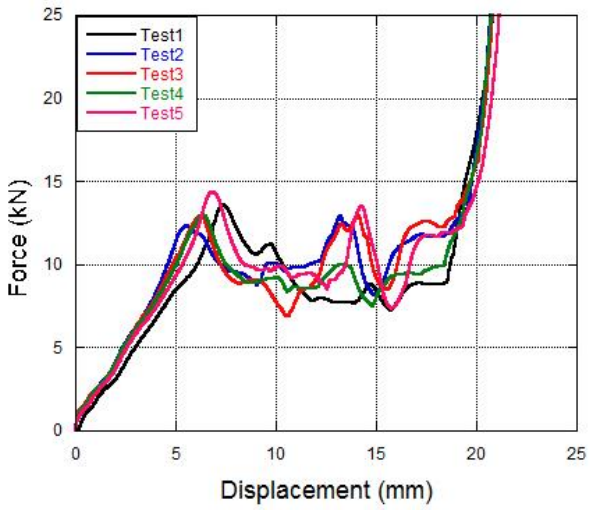

(a)

Figure 5.7. The quasi-static crushing test results of the inner core; (a) 10^{-3} s^{-1}, (b) 10^{-2} s^{-1}, (c) 10^{-1} s^{-1} and (d) strain rate sensitivity.

(cont. on next page)

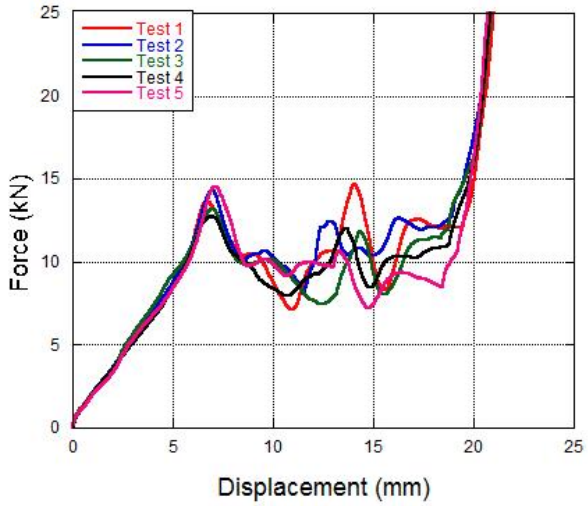

(b)

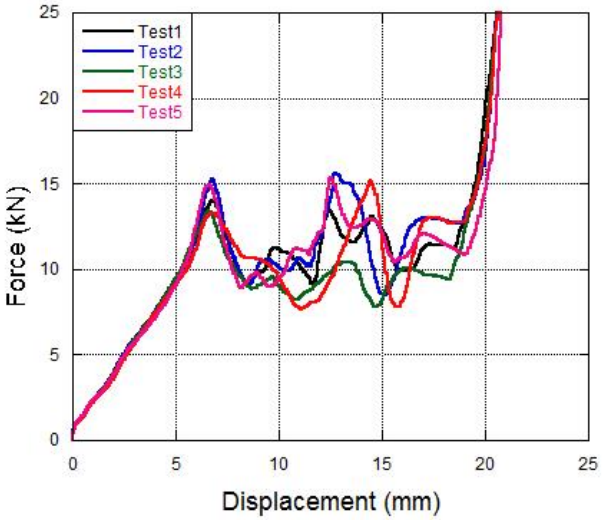

(c)

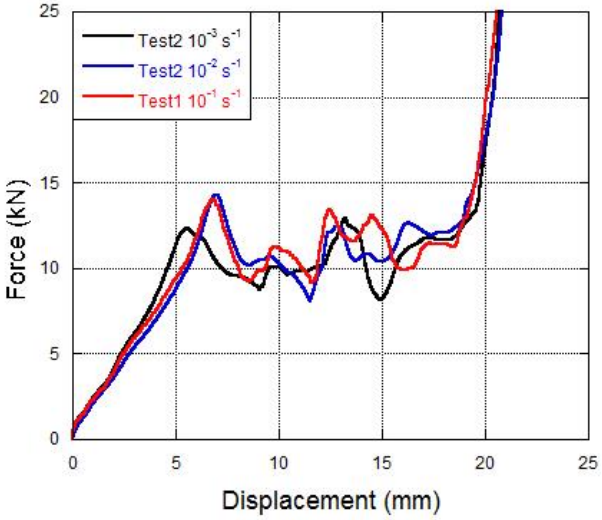

(d)

Figure 5.7. (cont.)

Figure 5.7 obviously shows that the force increased linearly when the hemispherical part of the inner core initiated to deform with the inward dimpling and the first fold formation occurred. Moreover, fold formation is seen as a peak formation in the force-displacement curves. As the deformation proceeds, the crushing force decreases until the deformation of the conical portion. Compression of conical portion caused an increase in the crushing force. This increase continued until the second fold formation at 13 mm of deformation. The new fold formations were observed with the further deformation and these are seen as the local maximum and minimum points in the force-displacement curves. After the last fold formation, specimen contacted with the crushing heads and upward deformation occurred. At 20 mm of deformation, the densification region was observed and the specimen completed the deformation in diamond mode resembling a triangular shape.

The comparison of both experimental and numerical results of inner core structure is given along with the deformation modes at various displacements, Figure 5.8. It is clearly seen that numerical results of both force-deformation curves and deformation modes are in concordance with the test results.

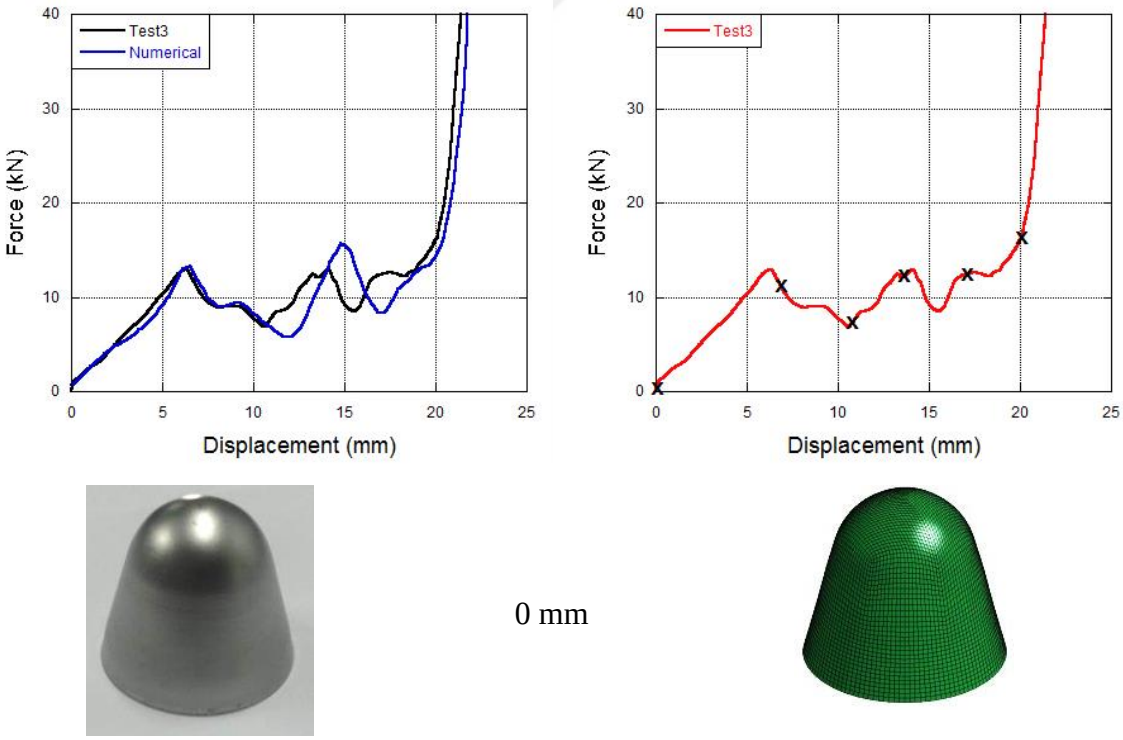

Figure 5.8. Both experimental and numerical quasi-static deformation history of the inner core.

(cont. on next page)

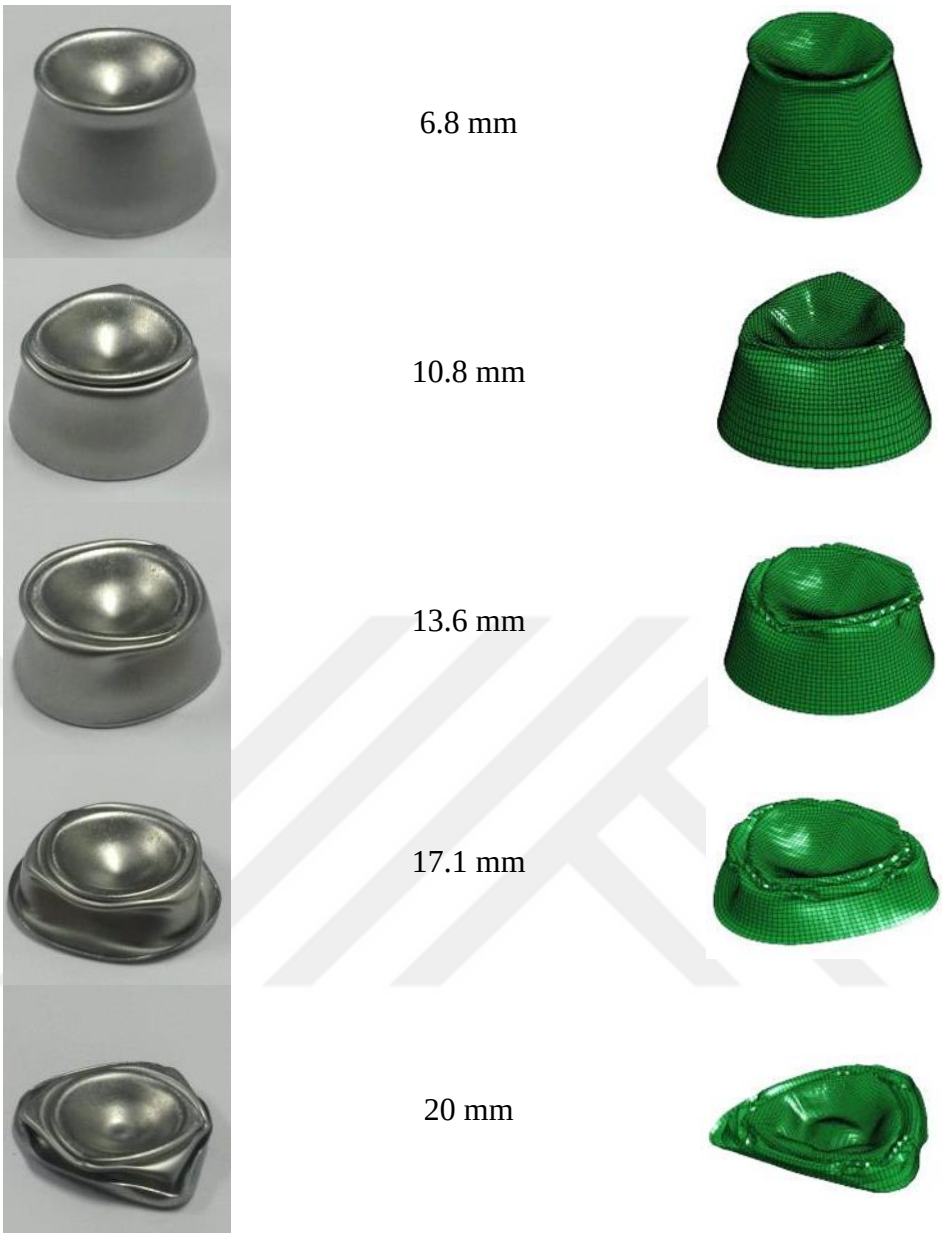

Figure 5.8. (cont.)

After the quasi-static tests of the inner core, drop weight experiments were performed both experimentally and numerically. The energy absorbing capacity of inner core structures was determined considering the quasi-static force-displacement curves up to approximate densification region. Fractovis drop weight tower was used for low-velocity axial impact experiments. In the drop weight tests, 4 m/s was selected as impact velocity and required additional masses were added to attain the statically absorbed energy levels. In Figure 5.9, both experimental and numerical force-displacement curves of the inner core are given and compression tests of the specimen are presented at static and dynamic strain rates, respectively.

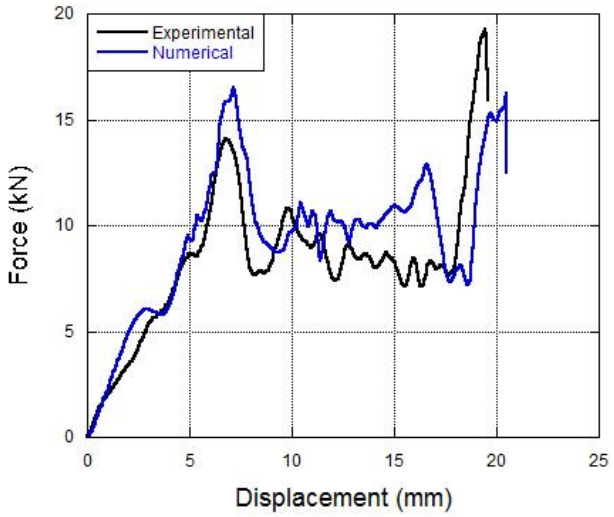

(a)

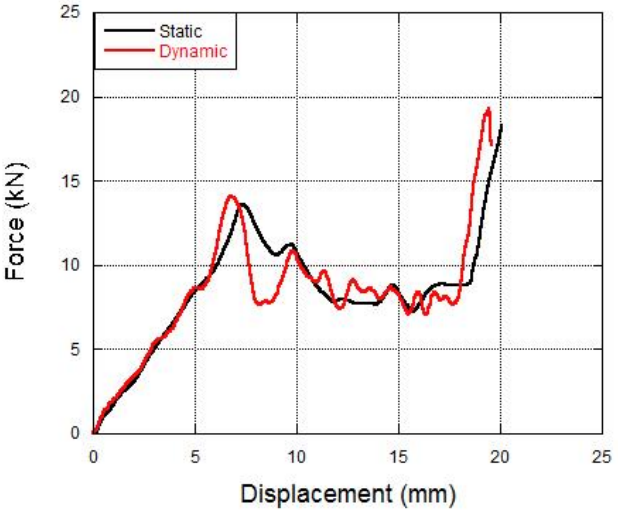

(b)

Figure 5.9. (a) The dynamic crushing behavior of the inner core and (b) the strain rate effect.

As seen in Figure 5.10, crushing force increased with the deformation of the hemispherical region of inner core structure. After the fold formation completed at about 7 mm of deformation, the crushing force started to decrease. The deformed hemispherical region of the inner core resembled a triangular shape. The deformation mode switched to a diamond pattern with the deformation proceeded. Furthermore, the local maximum and minimum points corresponding to the folds formations are seen in the force-displacement curves. The crushing force started to increase at about 17 mm of deformation. As seen from the figure, experimental results are in agreement with

numerical data. Markers on the curve represent the certain displacements of the deformation which specimen photos were taken at.

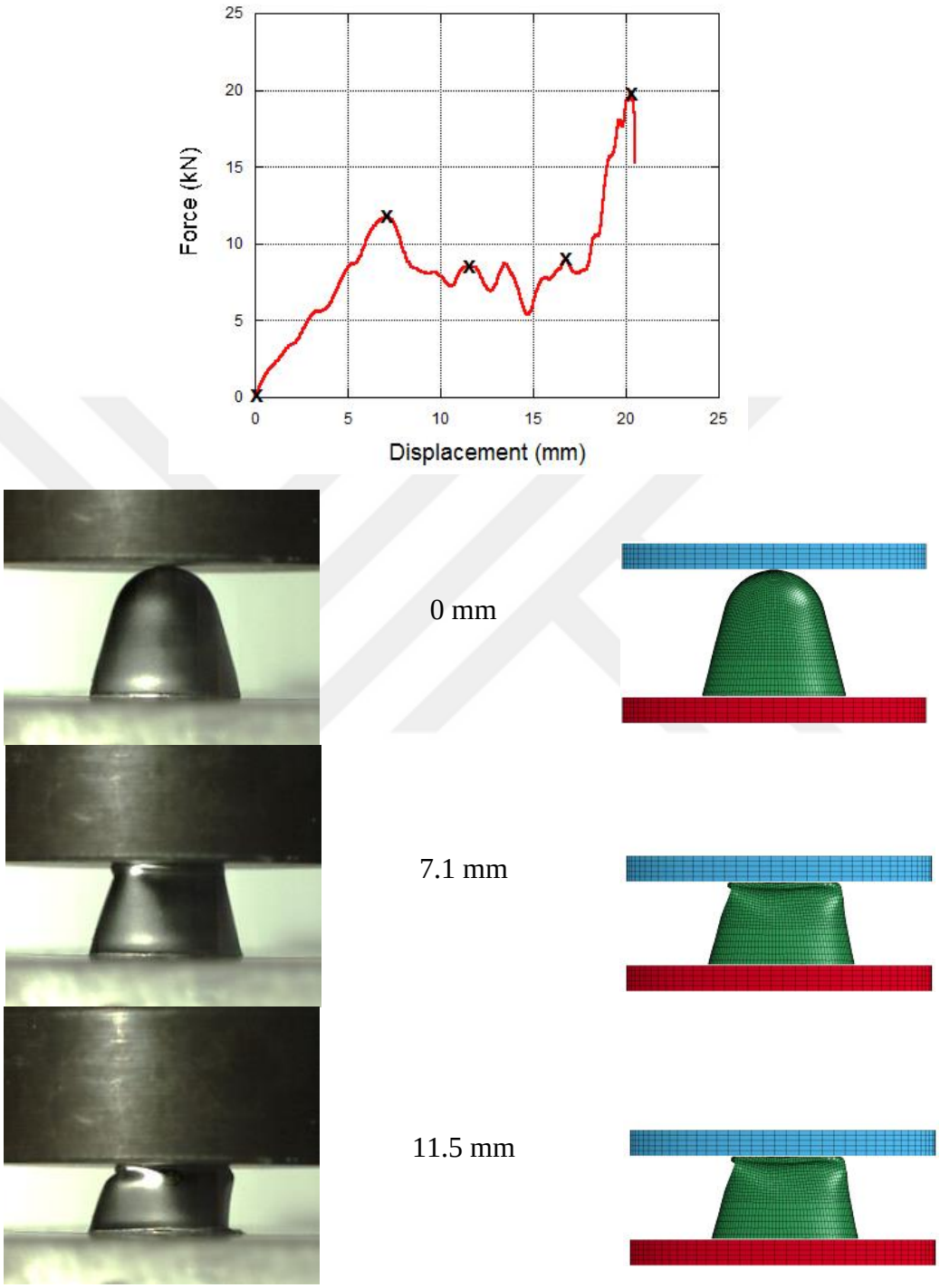

Figure 5.10. The dynamic crushing history of the inner core.

(cont. on next page)

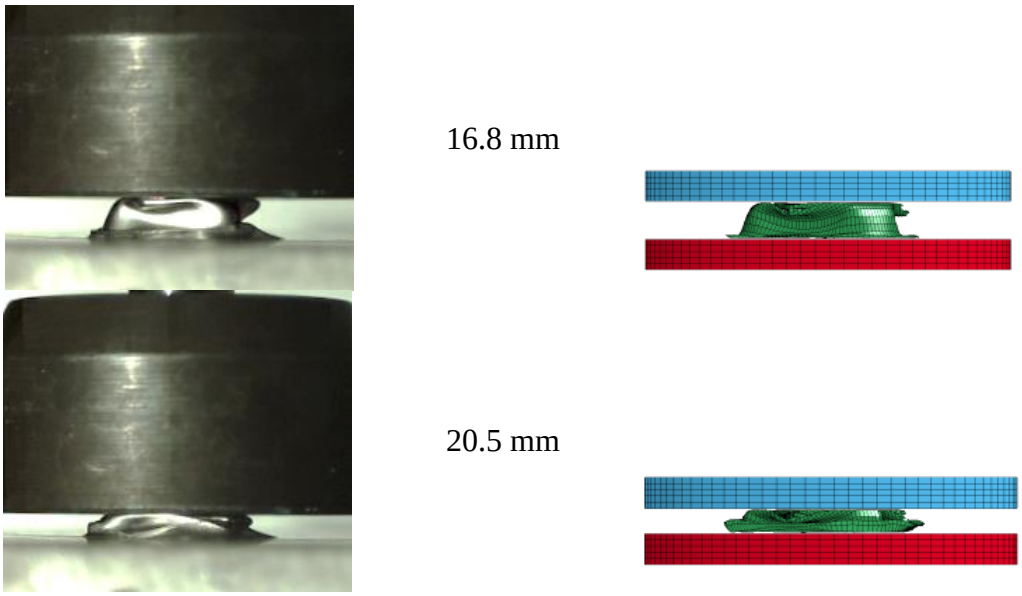

Figure 5.10. (cont.)

The tests were continued with the quasi-static crushing tests of the outer shell at 10^{-3} s^{-1}, 10^{-2} s^{-1} and 10^{-1} s^{-1} strain rates. Five specimens were deformed at these three different strain rates. The force-displacement curves of outer shell structures are given in Figure 5.11. The experimental deformation history of the outer shell clearly shows that the crushing behavior of the specimen does not change significantly at the various quasi-static strain rates.

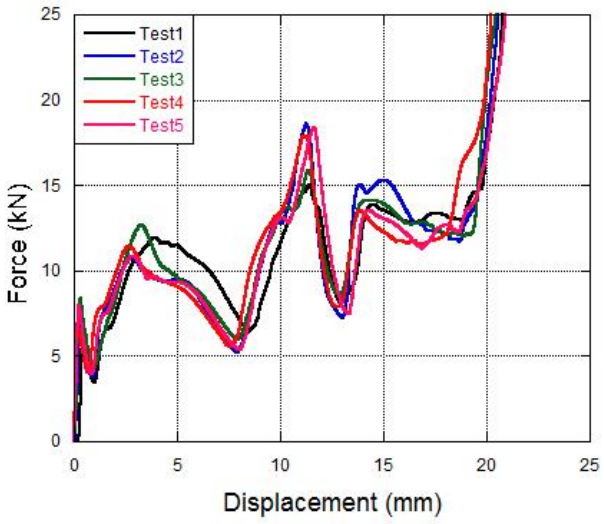

(a)

Figure 5.11. The quasi-static crushing test results of the outer shell; (a) 10^{-3} s^{-1}, (b) 10^{-2} s^{-1}, (c) 10^{-1} s^{-1} and (d) strain rate sensitivity.

(cont. on next page)

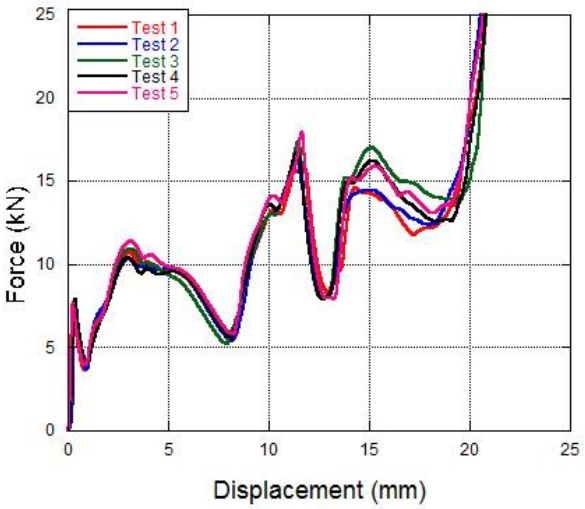

(b)

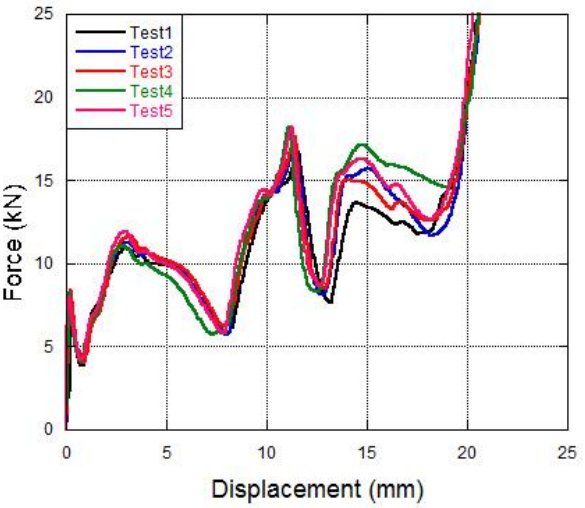

(c)

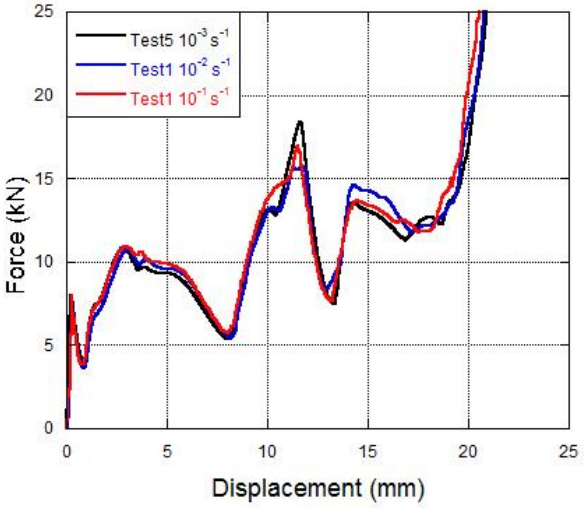

(d)

Figure 5.11. (cont.)

The experimental and numerical force-displacement curves of the outer shell are given along with the deformation modes at various displacements in Figure 5.12. The figure shows that the upper region of outer shell structure was bended inward and then the first fold formation was observed. The local maximum and minimum points corresponding to the fold formation were also observed in the load-displacement curves of the outer shell. It was found that the outer shell has a stable crushing characteristic which is about a mean force after the first fold formation. The specimens were deformed in diamond mode and the densification was observed at 20 mm of deformation. Figure 5.12 shows a comparison of the numerical results and experimental results. As seen in the figure, both force-deformation curves and deformation modes are in good agreement.

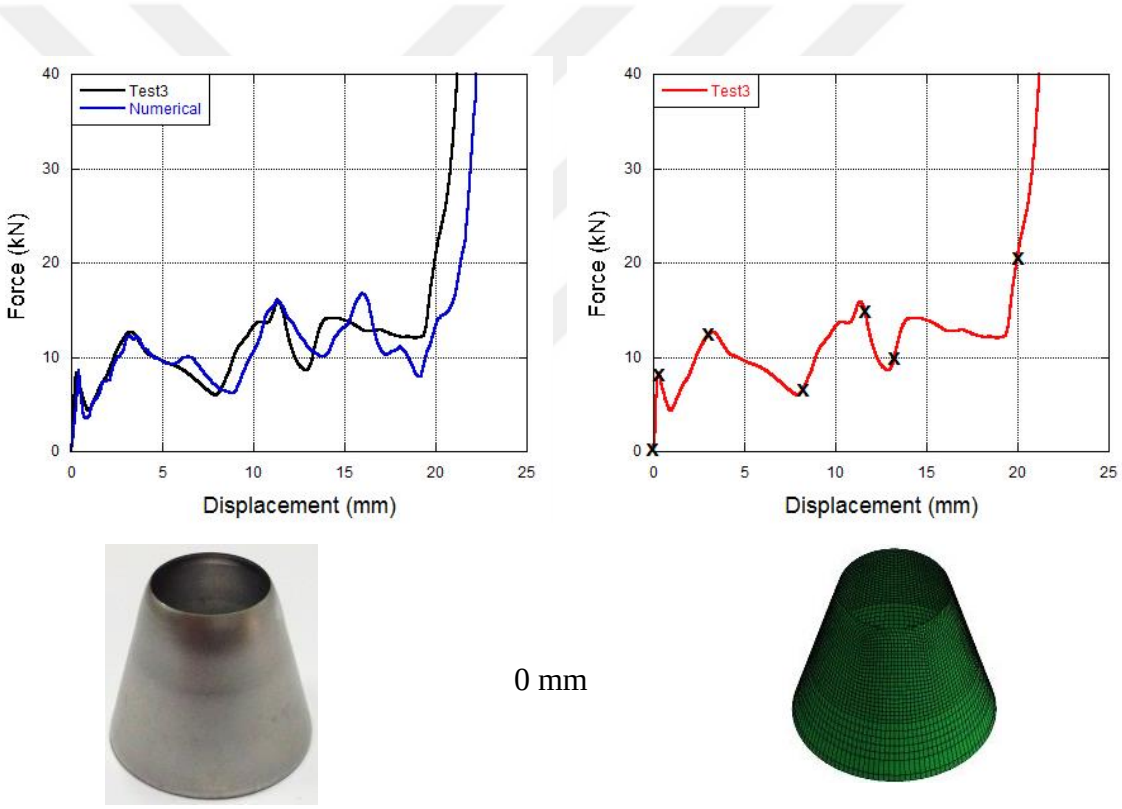

Figure 5.12. Experimentally and numerically quasi-static deformation history of the outer shell.

(cont. on next page)

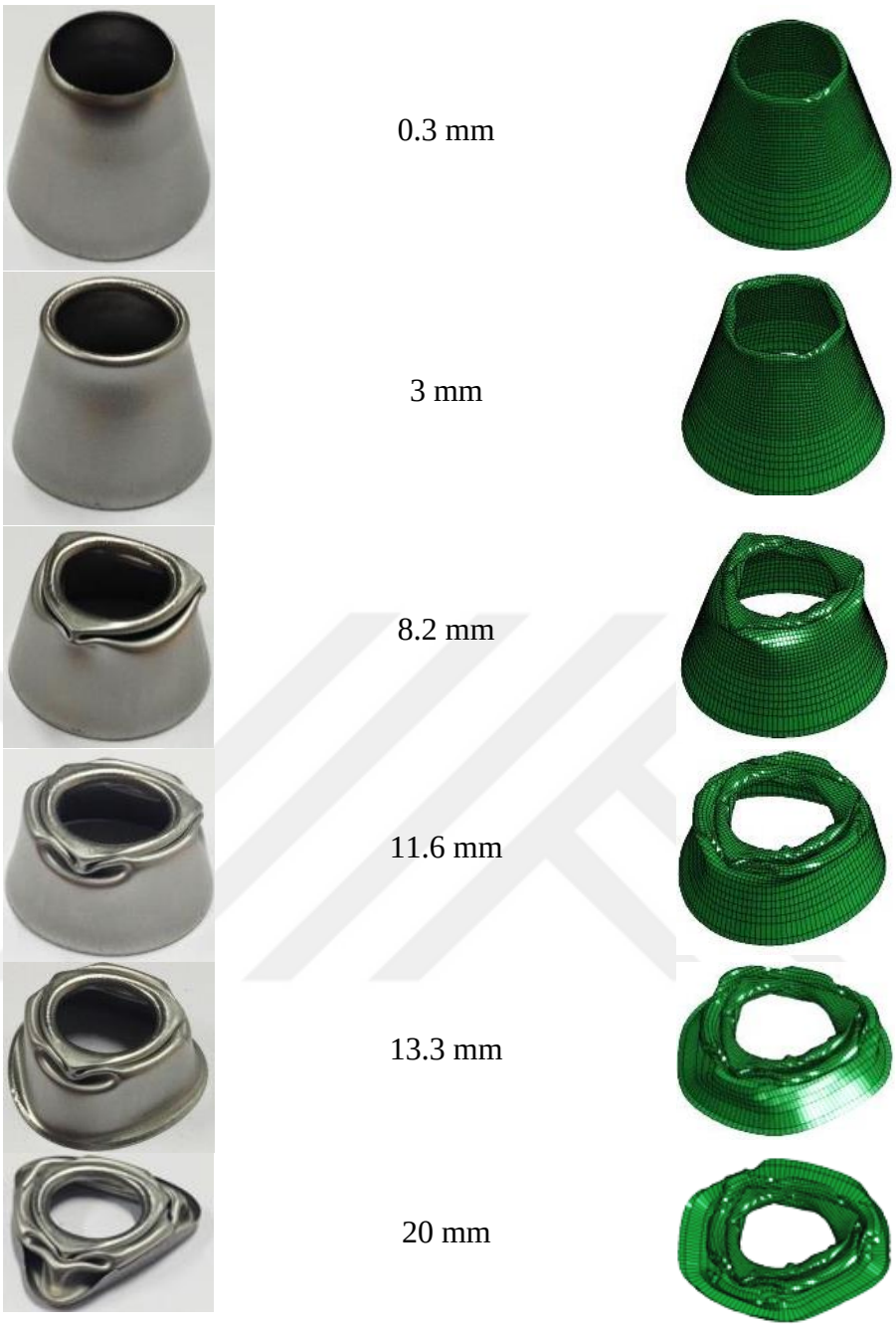

Figure 5.12. (cont.)

In Figure 5.13 (a), experimentally and numerically comparisons of force-displacement curves of the outer shell are presented and the load-carrying capacity of the structure under quasi-static and dynamic loadings is given in Figure 5.13 (b).

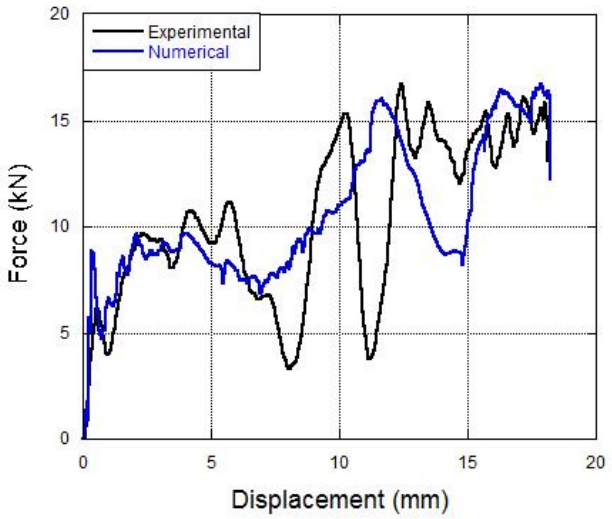

(a)

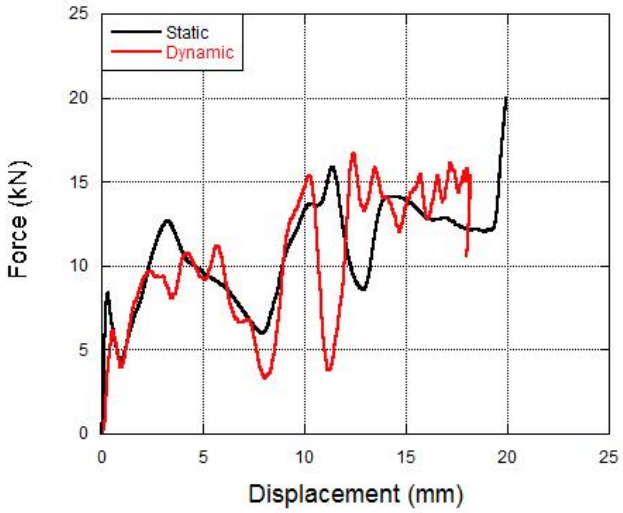

(b)

Figure 5.13. (a) Dynamic crushing behavior of the outer shell and (b) the strain rate effect.

As can be seen in Figure 5.14, experimental dynamic deformation history of outer shell structure is in pretty agreement with numerical results in terms of deformation modes. The upper region of the geometry was curled inward and then the initial peak was observed in the force-displacement curve. When the first fold formation of the conical portion of the outer shell was occurred at about 6 mm of deformation, the local maximum point was observed. In addition, the fold was completed at approximately 8 mm of deformation and then the force decreased. The overall crushing force increased with the deformation. The local maximum and minimum points corresponding to the fold formation were also observed with further deformation.

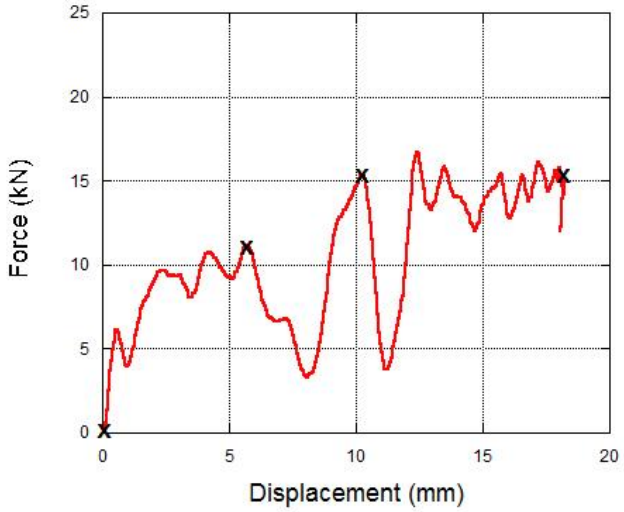

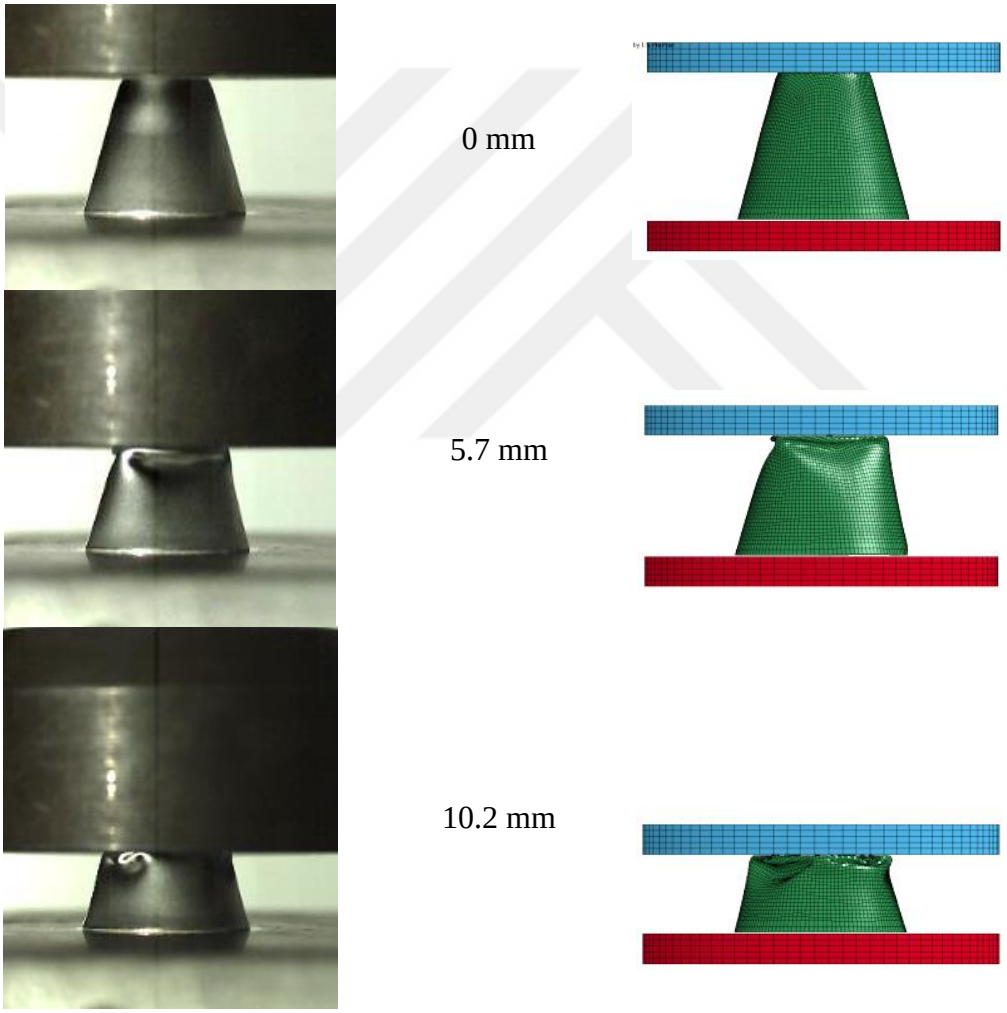

Figure 5.14. Dynamic crushing history of the outer shell.

(cont. on next page)

18.2 mm

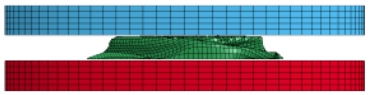

Figure 5.14. (cont.)

Quasi-static crushing tests were completed with the tests of balanus structures at different strain rates. Five balanus specimens were tested at 10^{-3} s^{-1}, 10^{-2} s^{-1} and 10^{-1} s^{-1} strain rates. The initial deformation behaviors of both balanus and outer shell geometries presented a significant amount of similarities. The outer shell and the inner core interacted with each other and deformed together as the deformation continued. The overall crushing character of the structure is around an average force. During the last fold formation which is before the densification, there is a global bending effect in the structure. This resulted in a slight variation at the last region of the curves. The specimens reached the densification at 18 mm of deformation.

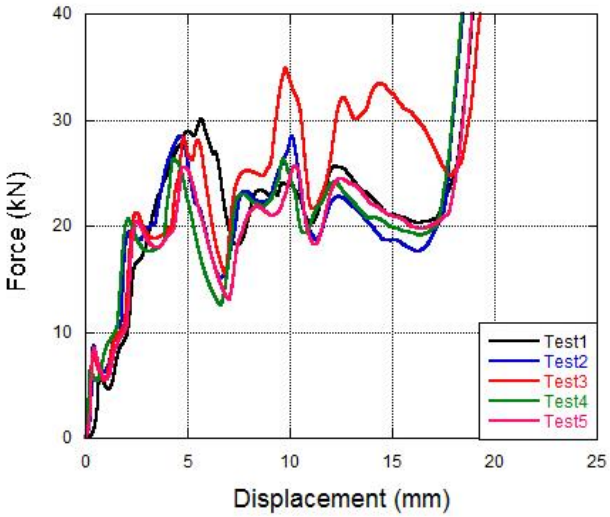

(a)

Figure 5.15. Quasi-static crushing test results of the balanus geometries; (a) 10^{-3} s^{-1}, (b) 10^{-2} s^{-1}, (c) 10^{-1} s^{-1} and (d) strain rate sensitivity.

(cont. on next page)

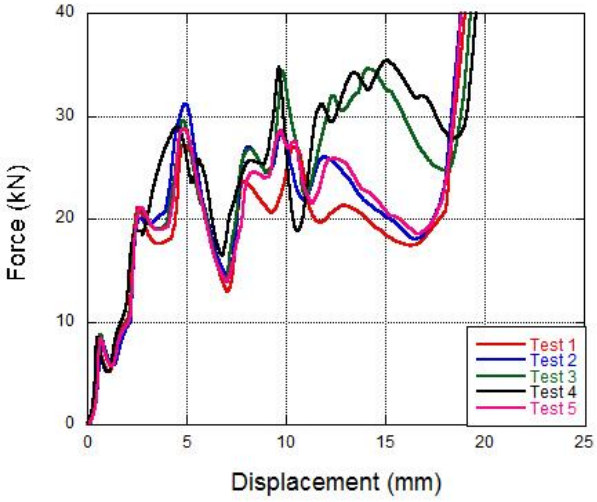

(b)

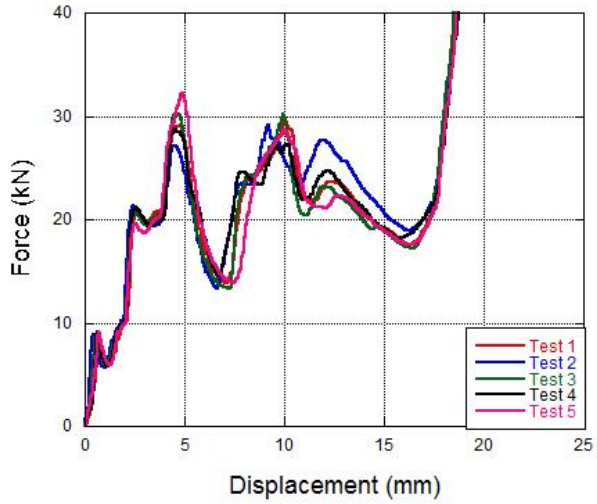

(c)

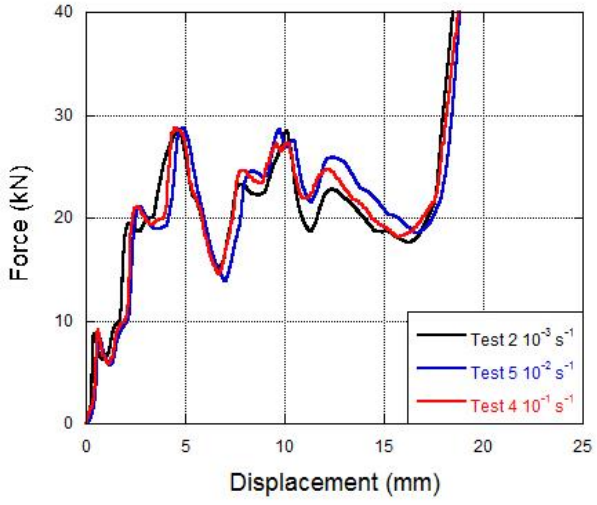

(d)

Figure 5.15. (cont.)

The comparison of both the experimental and numerical results of balanus specimens is given in Figure 5.16. As seen in the figure, numerical results of both force-deformation curves and deformation modes are close to the test data. The upper region of the balanus structure was curled inward due to the outer shell and the initial peak was observed at about 1 mm of deformation. Before the first fold formation, the force increased linearly when the hemispherical portion of inner core structure of the balanus geometry deformed with the inward dimpling. The crushing force decreased after the fold formation. The local maximum and minimum points corresponding to the fold formation were observed with further deformation in the force-displacement curves. The specimens were deformed in approximately diamond mode and the densification was observed at 18 mm of deformation.

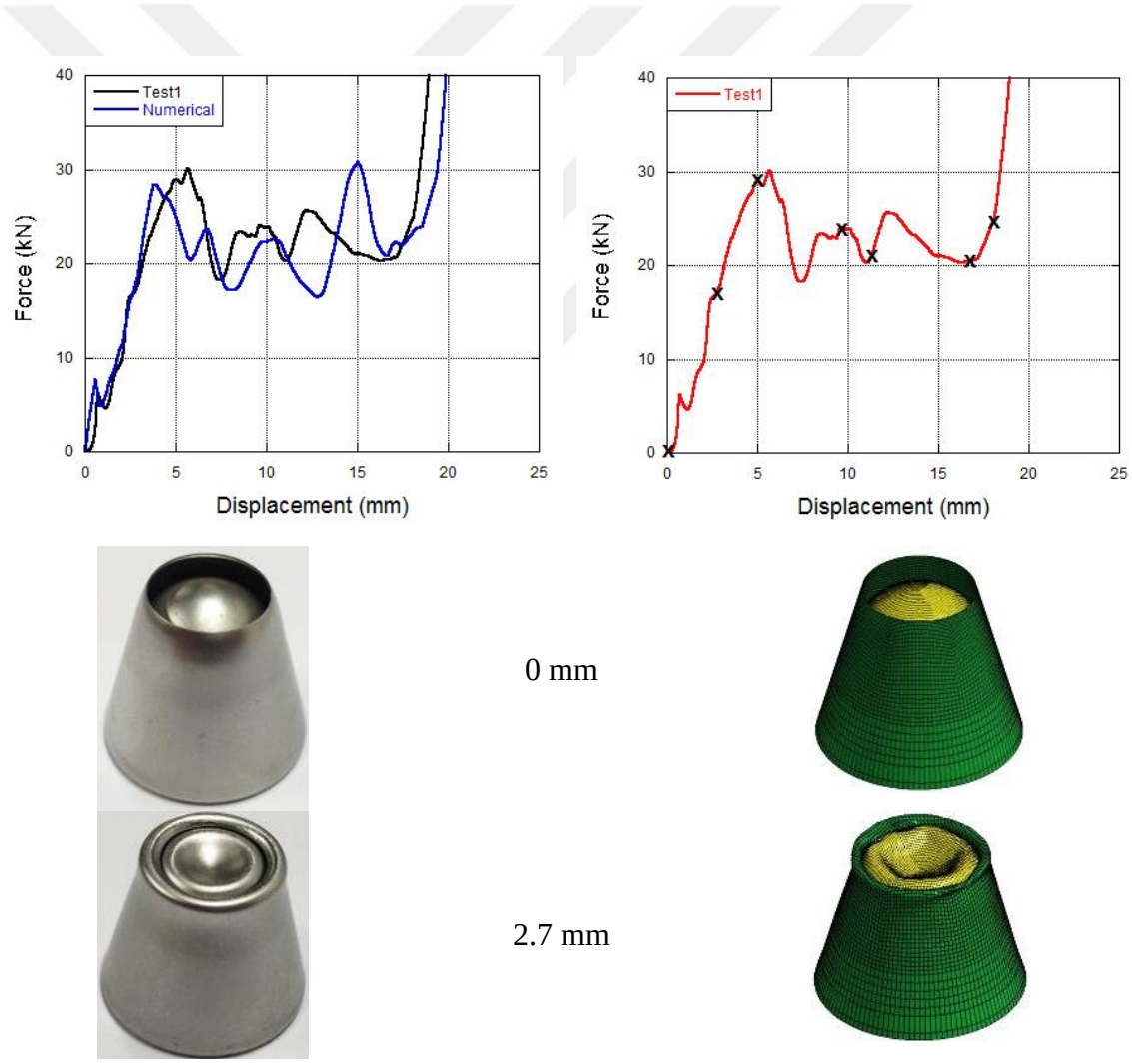

Figure 5.16. Experimentally and numerically quasi-static deformation history of balanus structure.

(cont. on next page)

Figure 5.16. (cont.)

Figure 5.17 (a) shows the experimental and numerical comparison of load-displacement curves of the balanus. Quasi-static and drop weight crushing experiments of the specimen are given in Figure 5.17 (b). It should be stated that tearing was observed in some balanus specimens during fold formation at dynamic strain rates.

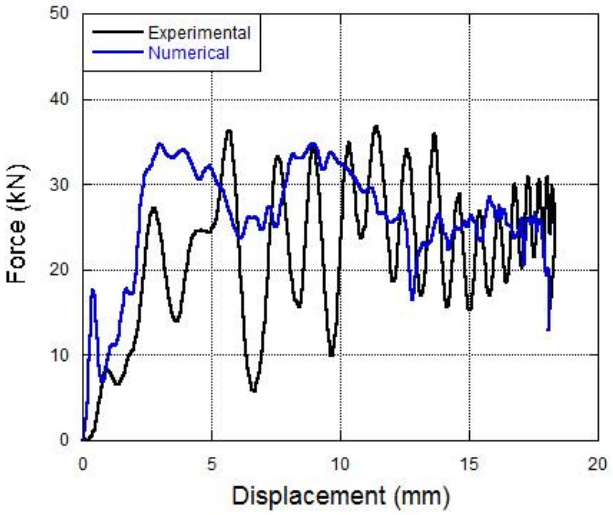

(a)

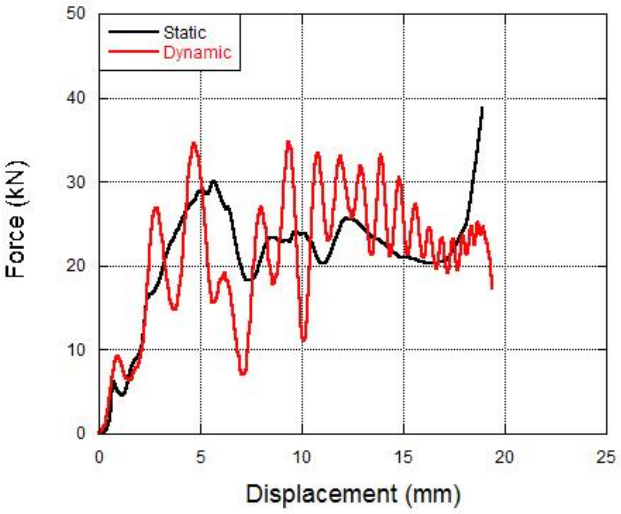

(b)

Figure 5.17. (a) Dynamic crushing behavior of the balanus structure and (b) the strain rate effect.

As can be seen from Figure 5.18, numerical deformation modes of the balanus structure closely resemble with experimental results at dynamic strain rates. The initial peak was seen at about 1 mm of deformation as an effect of the outer shell structure. The force increased during the deformation of the balanus until the first fold formation. In addition, the hemispherical region of the inner core and the upper region of the outer shell interacted with each other during the first fold. Therefore, deformation behavior of the balanus resembled with the inner core at the beginning of the first fold and inward dimpling was observed. The force started to decrease with further deformation and one of the local minimum points was seen at 7 mm of deformation. The other local

maximum and minimum points corresponding to the fold formation were observed with further crushing in the curve. The outer shell confined the inner core when the conical segment of the specimens started to deform and crushing behavior of the balanus resembled with the outer shell at the rest of the deformation.

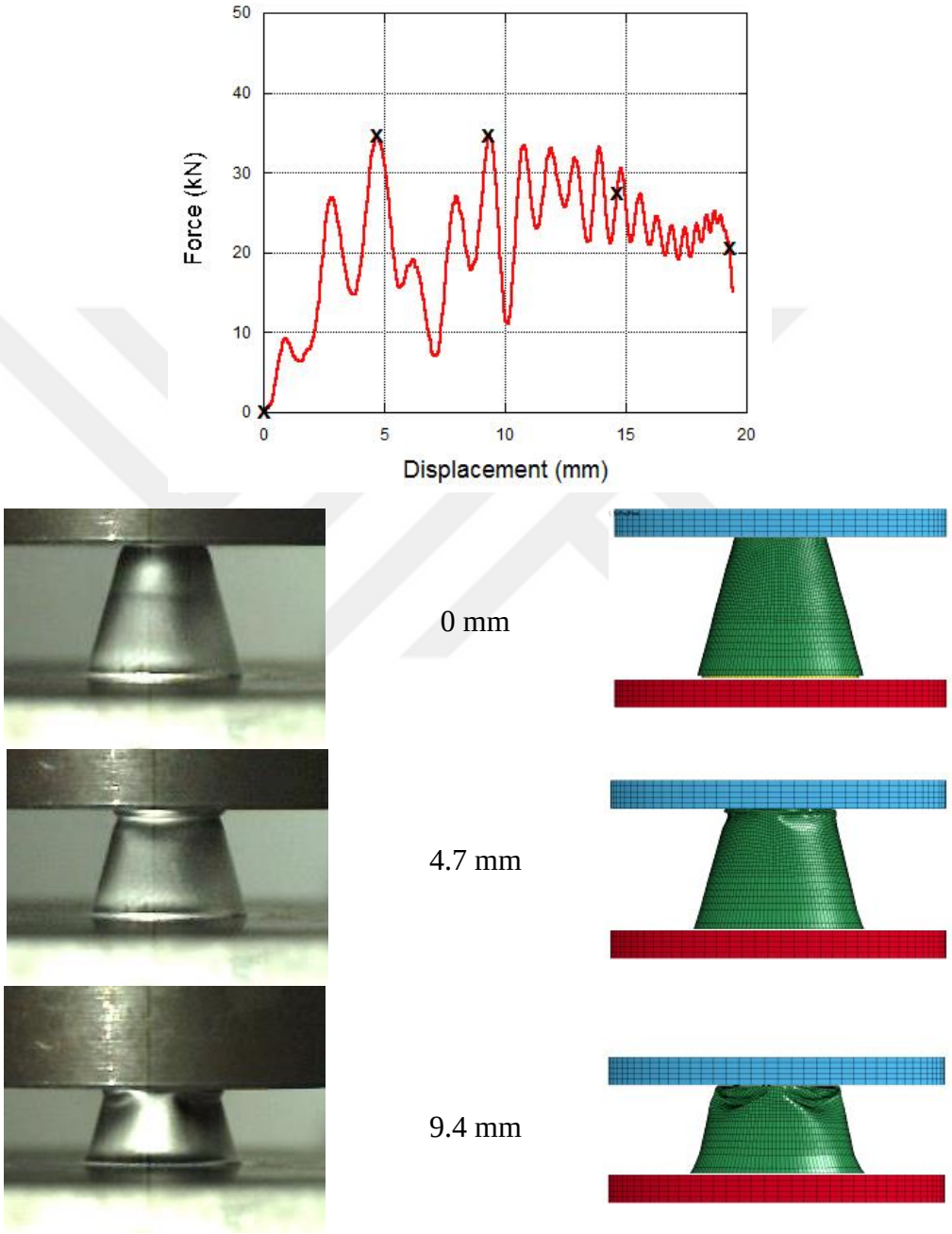

Figure 5.18. Dynamic crushing history of the balanus structure.

(cont. on next page)

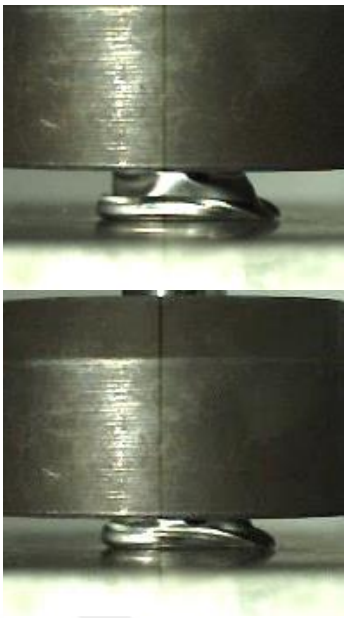

Figure 5.18. (cont.)

Experimental results were tabulated in the below tables. The maximum force value in drop weight experiments (34.73 kN) is approximately 16 percent superior than that of the quasi-static (30.03 kN). When the static and dynamic experimental test results were investigated, it was determined that inner core structure absorbed the least amount of the energy whereas the balanus structure absorbed the most. The average force value at drop weight experiment was above than that of the quasi-static, causing to higher SAE value in drop weight test. When the specific absorbed energy was considered, it was seen that the outer shell and the balanus were more efficient than the inner core at the quasi-static strain rate. However, the balanus is the most efficient configuration in terms of energy absorption among all structures at dynamic strain rates. Again with the increasing strain rate, the energy absorption characteristic of the balanus improved when the inner core and the outer shell decreased. Diamond fold formation resembling a triangular shape was observed at both quasi-statically and dynamically deformed specimens.

Table 5.1. Quasi- static experimental results of the specimens.

Specimen	P_i (kN)	P_{mean} (kN)	P_{max} (kN)	Energy (J)	Compression (mm)	SAE (kJ/kg)	SAE (kJ/kg) @18.2 mm
Core	12.96	9.04	12.96	171.30	18.95	26.47	25.03
Shell	8.35	10.69	15.87	209.36	19.58	30.96	28.45
Balanus	6.15	20.76	30.03	382.82	18.44	28.92	28.41

Table 5.2. Experimental results of the specimens at dynamic strain rates.

Specimen	P_i (kN)	P_{mean} (kN)	P_{max} (kN)	Energy (J)	Compression (mm)	SAE (kJ/kg)	SAE (kJ/kg) @18.2 mm	Test Conditions
Core	11.75	8.14	11.75	165.35	20.32	25.55	20.53	4 m/s 26.63 kg
Shell	6.09	10.33	16.71	188.05	18.20	27.81	27.81	4 m/s 28.38 kg
Balanus	9.17	21.21	34.73	401.80	18.94	30.35	29.02	4 m/s 59.38 kg

During the deformation of the balanus, the inner core and the outer shell deformed together and the interaction between the two components occurred. First of all, the force-displacement curves and energy absorption capacities were determined for each the inner core and the outer shell in order to investigate the efficiency of this interaction. The outer shell confined the inner core and advanced the energy absorption capacity of the inner core during the deformation. In order to understand this improvement, the arithmetic total results of the test results of the inner core and the outer shell were compared with the test results of the balanus. Quasi-static and drop weight test results are shown below, Figure 5.19.

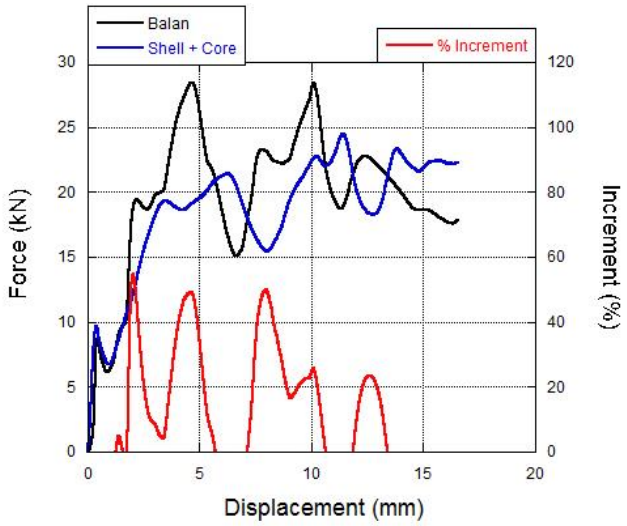

(a)

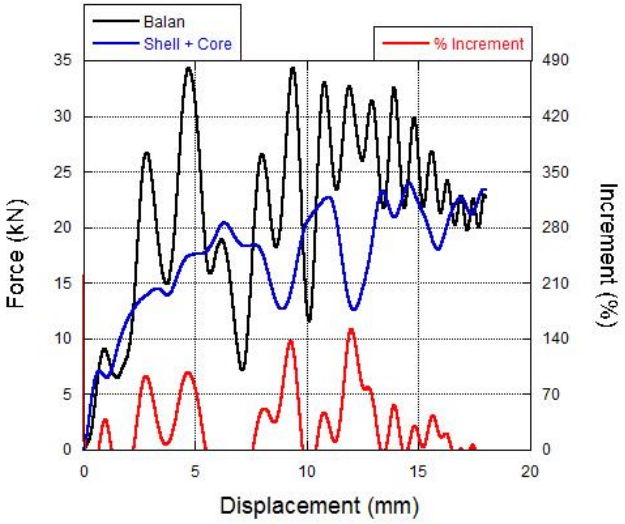

(b)

Figure 5.19. Force increase stemming from the interaction between the surfaces of inner core and the outer shell; (a) static and (b) dynamic.

A 50 percent increase of load carrying capacity was observed due to the interaction between the surfaces of the inner core and the outer shell during the static crushing experiments. However, the amount of increase reached up to a 150 percent of load carrying capacity in the dynamic crushing experiments. As seen in the figures, as the crushing velocity increases, the amount of interaction increases.

The inner core structures were filled with polyurethane foam material to see the effect of inner confinement. 50 percent increase of load carrying capacity was observed due to the effect of foam material in the inner core during the quasi-static crushing experiments. 80 percent increase of load carrying capacity was reached due to the foam material in the dynamic crushing experiments. As seen in Figure 5.20, the contribution of foam material increases with the increase in velocity.

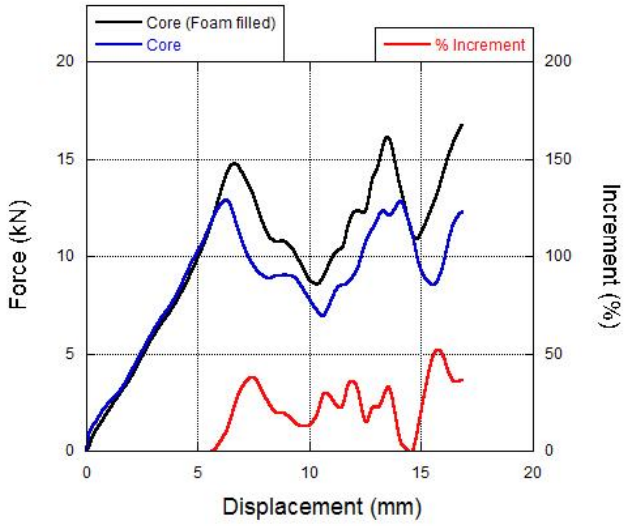

(a)

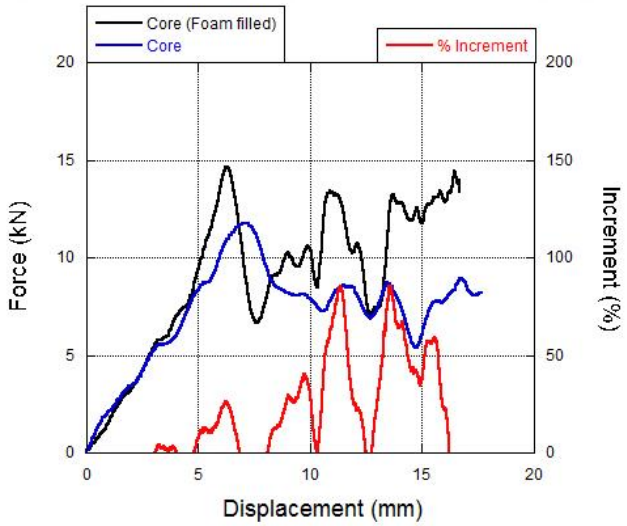

(b)

Figure 5.20. Force increment stemming from the interaction between the foam material and the inner core; (a) static and (b) dynamic.

In Figure 5.21, the experimental and numerical force-displacement curves of the structure are presented together. When the curves were investigated it was seen that the force linearly increased during the crushing of the hemispherical region of the inner core and the fold formation occurred after the deformation of the hemispherical region was completed. Fold formation continued with further deformation and this resulted in the occurrence of local maximum and minimum points in the curve.

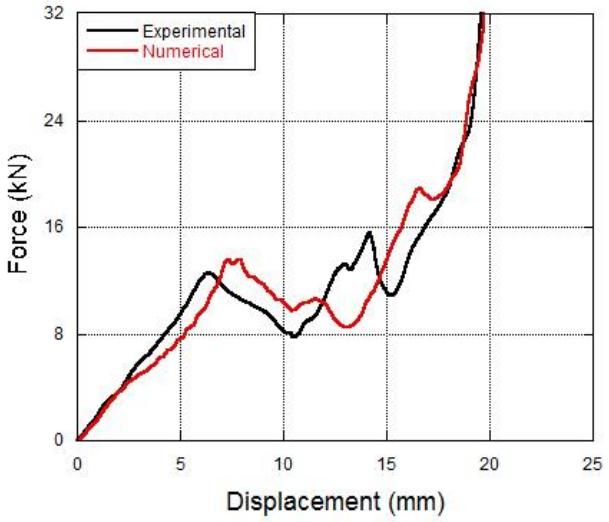

(a)

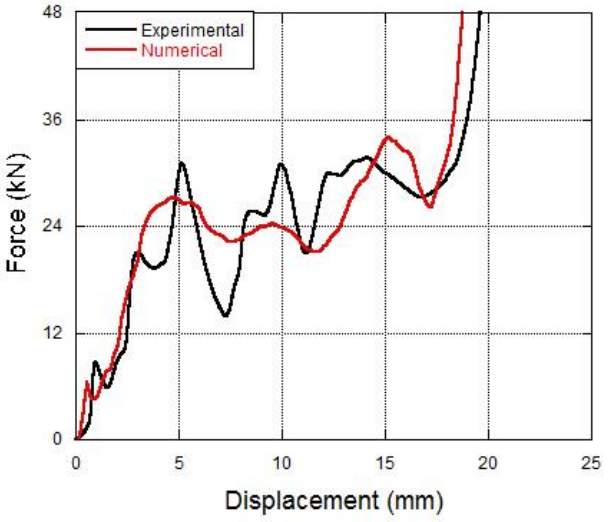

(b)

Figure 5.21. Quasi-static crushing behavior of foam filled specimens; (a) inner core and (b) balanus structure.

The deformation profiles of numerically deformed foam-filled inner core and balanus structures are in good agreement with experimental observations as seen in Figure 5.22.

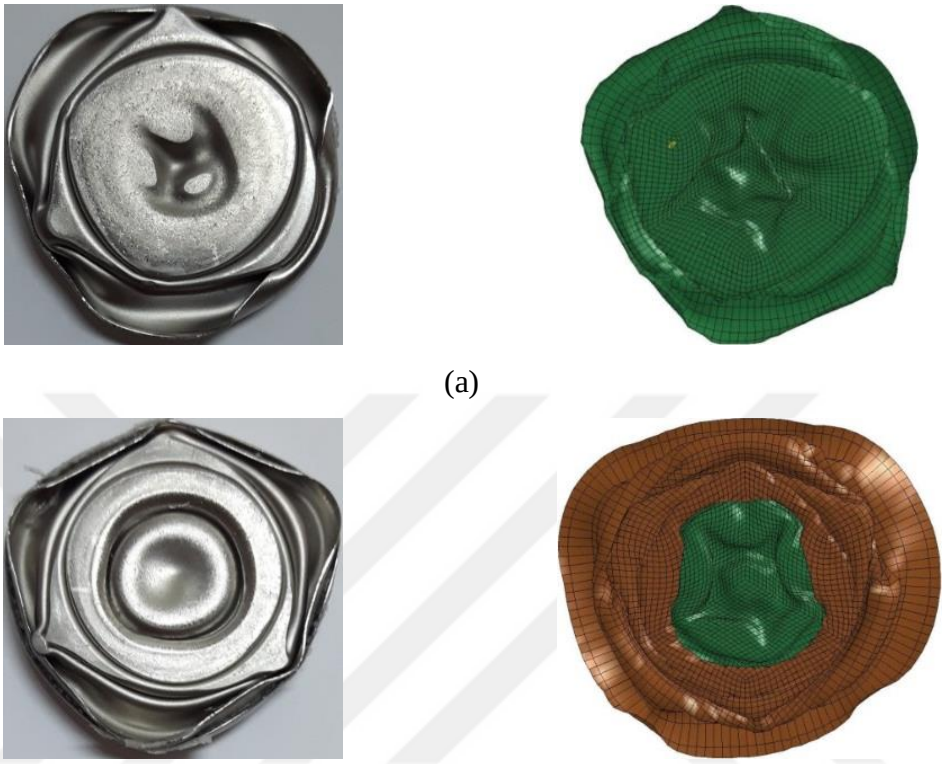

(a)

(b)

Figure 5.22. Experimentally and numerically crushed specimens under quasi-static strain rates; (a) the inner core and (b) balanus structure.

The crushing behaviors of the foam filled structures are different from other configurations due to the confinement effect as seen in the Figure 5.23. The load-carrying efficiency of the foam-filled material increases with further deformation.

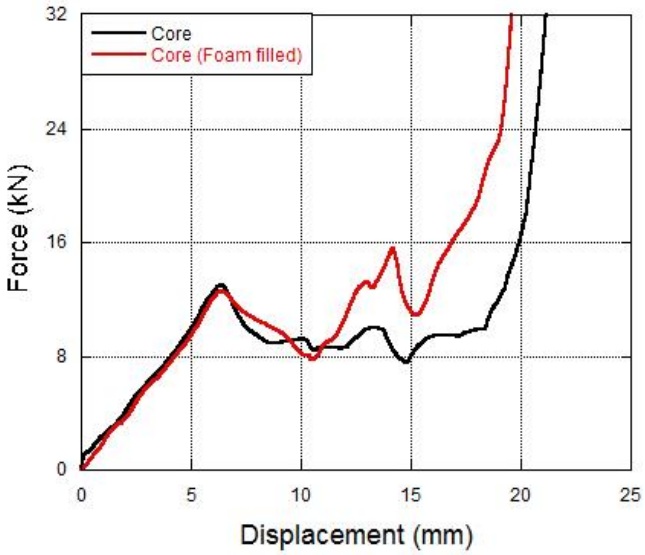

(a)

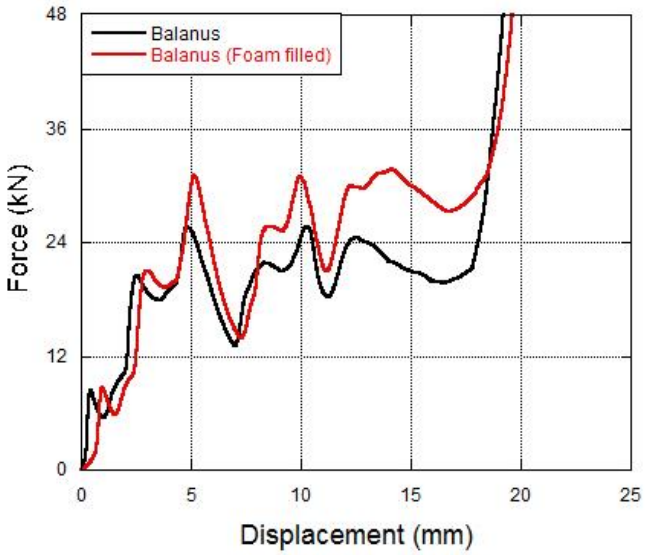

(b)

Figure 5.23. The quasi-static crushing behavior; (a) inner core structure and (b) balanus structure.

Drop weight experiments were conducted so as to clarify the dynamic deformation behavior of the foam-filled specimens. The impact velocity was selected as 4 m/s and additional drop masses to be used during experiments were determined by preliminary calculations taking into account the static energy of the structures (area below the force-displacement curves). The acquired force-displacement profiles are given in Figure 5.24. It is known that the mechanical properties of the polymeric based foam material show strain rate dependent behavior. The experimental data clearly indicate that the load carrying capacity of the structures increased with further

deformation due to both the constrained influence of polyurethane foam material and rate sensitivity of the material.

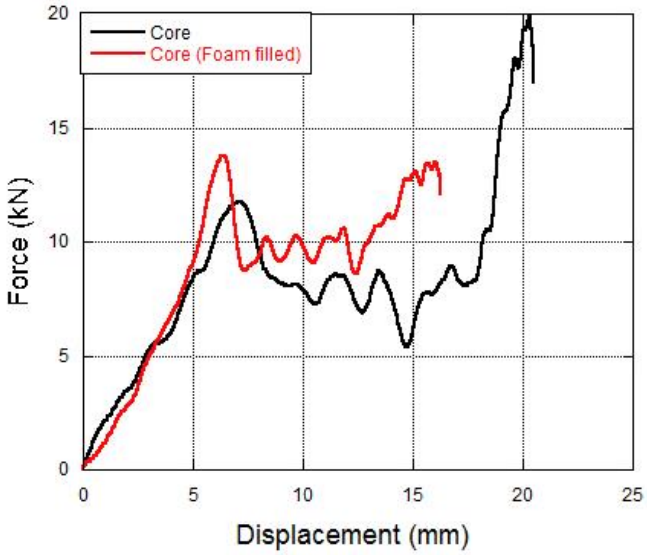

(a)

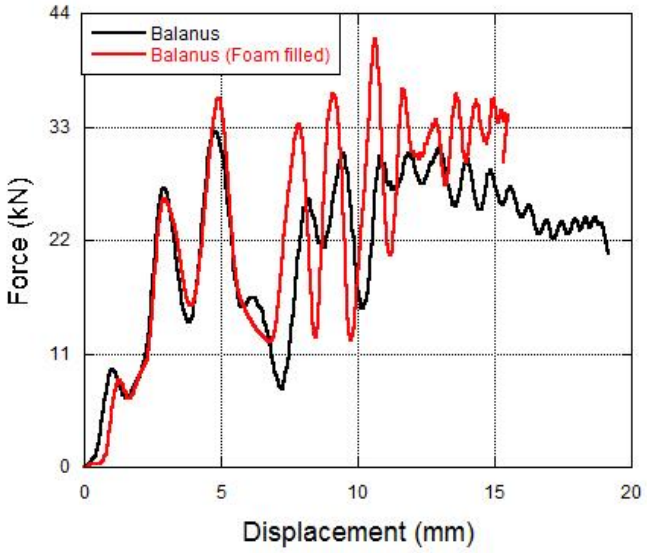

(b)

Figure 5.24. The dynamic crushing behavior; (a) the inner core and (b) balanus structure.

The force-displacement curves of foam-filled structures are presented both experimentally and numerically in Figure 5.25.

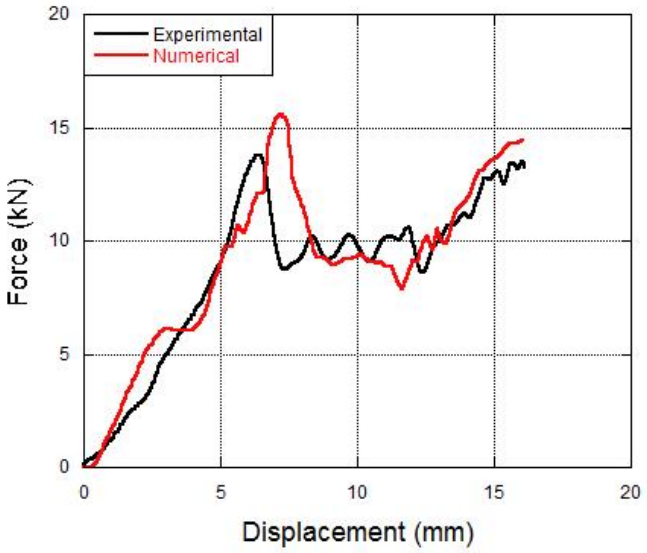

(a)

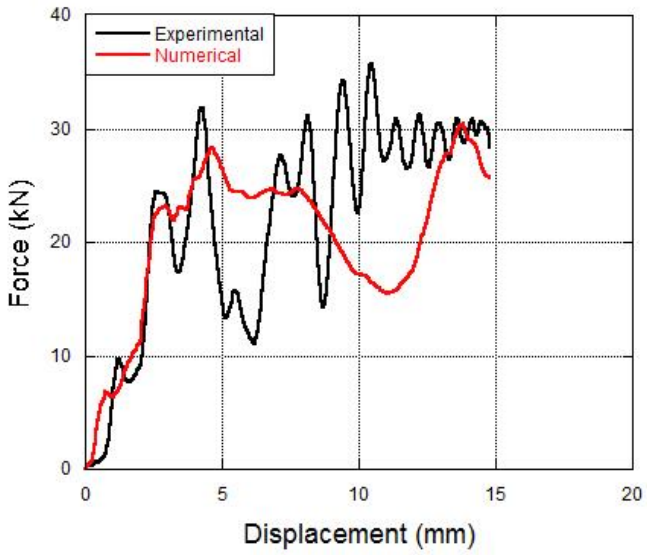

(b)

Figure 5.25. The dynamic crushing behavior of foam filled specimens; (a) the inner core and (b) balanus structure.

Figure 5.26 shows experimentally and numerically deformed specimens. As seen, numerical model results are good agreement with the experimental data.

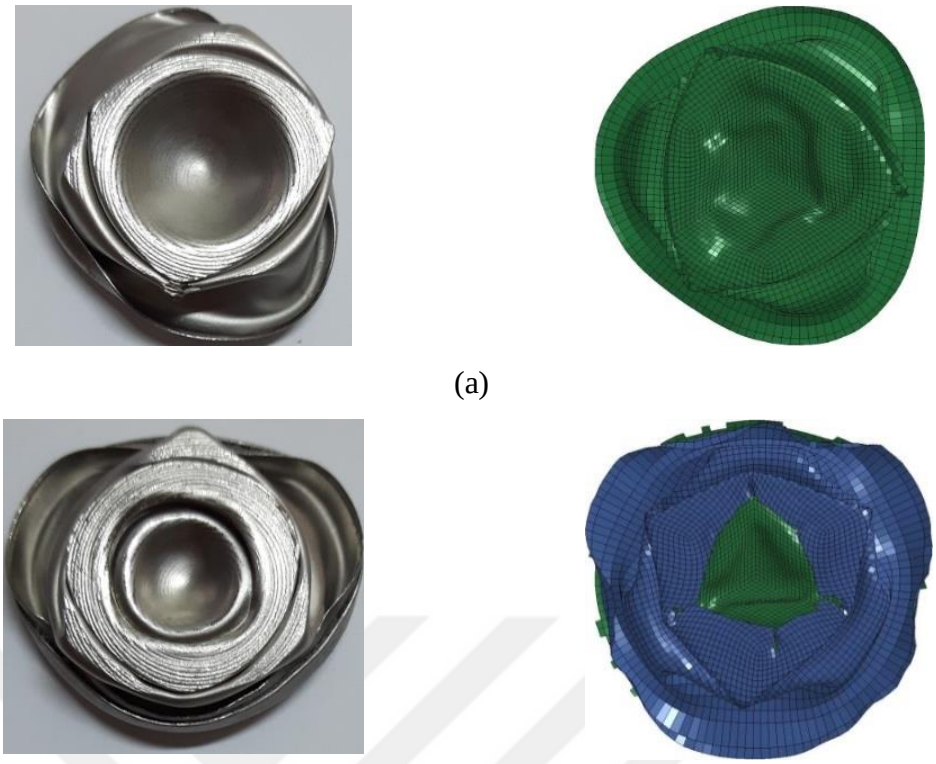

Figure 5.26. Experimentally and numerically crushed specimens at dynamic strain rates; (a) the inner core and (b) balanus structure.

It is possible to achieve more detailed information from numerical models so as to understand the interaction between the interfaces of inner core structure and the outer shell. In the numerical models, interface pressure history for different points can be determined and this gives a direct insight into the interaction during the deformation. Figure 5.27 shows the time-dependent pressure history at the interface between inner core structure and the outer shell at different points for both quasi-static model and drop weight model. During the deformation, the inner core and the outer shell interact with each other. Furthermore, this interaction influences the amount of energy absorption and the deformation mode. When the quasi-static model results were compared with the drop weight model results, it was determined that the interface pressure increases with the dynamic deformation.

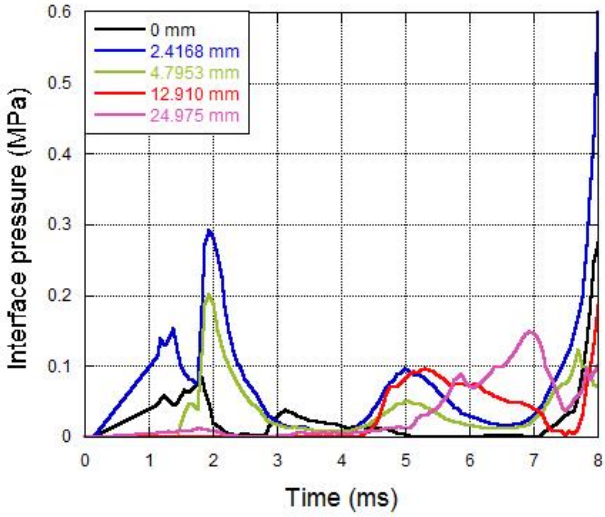

(a)

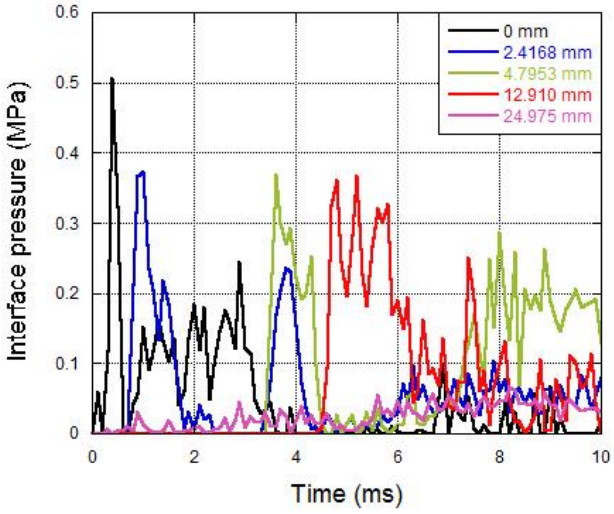

(b)

Figure 5.27. Interface pressure history of the inner core and outer shell; (a) static and (b) dynamic.

Figure 5.28 shows that the outer shell absorbs higher level energy than the inner core at the beginning of the deformation. At approximately 10 mm of deformation, the distribution of total absorbed energy among the components reached up to 60 percent and 40 percent. It was observed that the outer shell absorbed higher energy than the inner core throughout the deformation history. In the below Figure 5.28, energy partition curves of the components are given for both static and dynamic crushing. Obviously, the percentage of energy partition remained at similar levels for two strain rates.

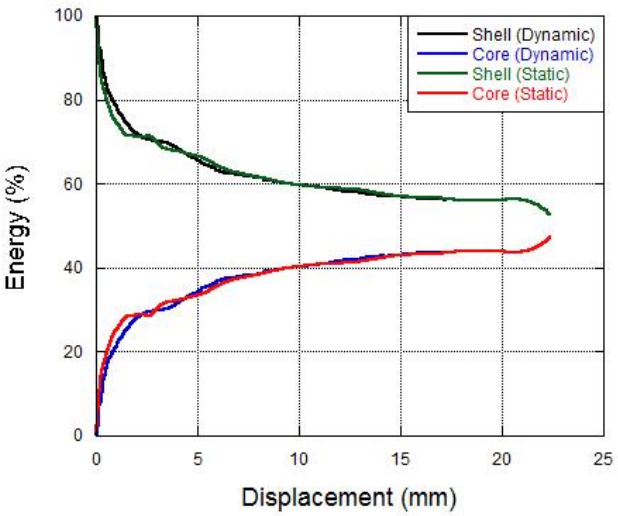

Figure 5.28. Energy partition of the inner core and outer shell structures.

The force-displacement curves of inner core, outer shell and balanus structures are given for different impact velocities in Figure 5.29. Quasi-static crushing behaviors of each structure were also presented for comparison. In general, the load bearing capacity of the structure increases with the increase of the impact velocity since AISI 304L stainless steel is a high strain rate sensitive material. Moreover, the micro-inertia effect of the geometry has also a significant role on the increments.

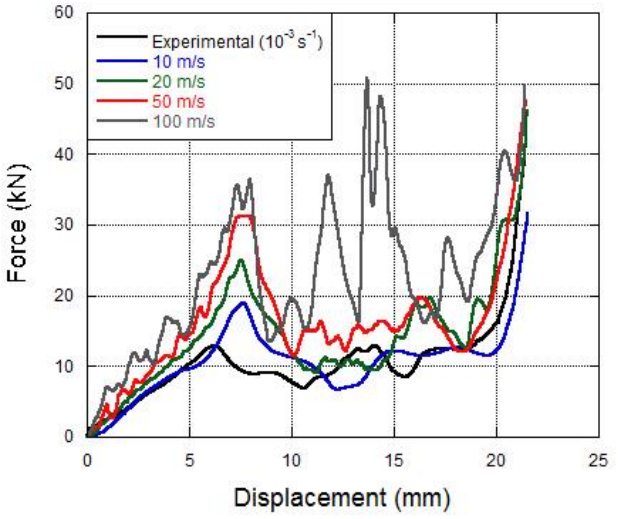

(a)

Figure 5.29. Force-displacement curves at different impact velocities; (a) inner core, (b) outer shell and (c) balanus.

(cont. on next page)

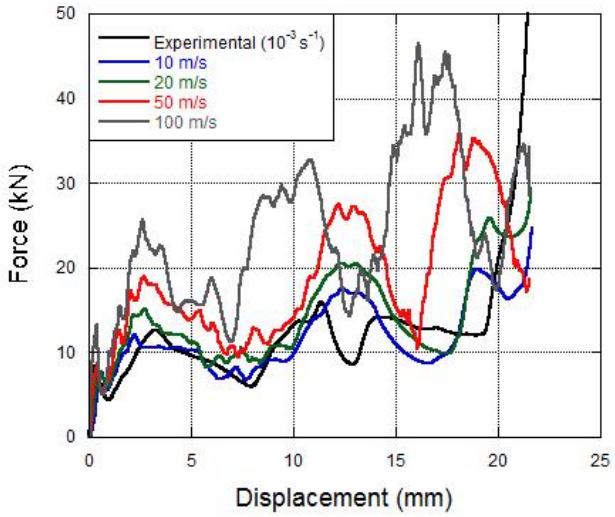

(b)

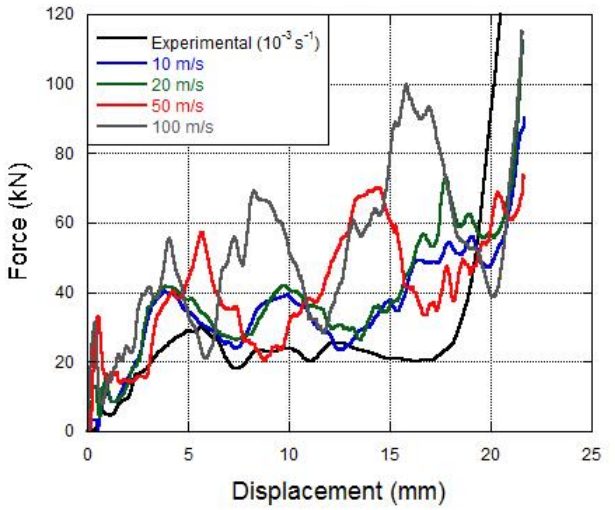

(c)

Figure 5.29. (cont.)

The energy partitions of the components of balanus structure during the deformation can be determined using numerical models. In the present study, balanus structure was investigated in terms of percentages of the energy absorption depending on the impact velocities. As the impact velocity increases, the difference of the energy absorption capacities between inner core and outer shell structures decreases with further deformation. The energy-displacement curves of the structures regarding percentages of the energy absorption at different impact velocities are given in Figure 5.30.

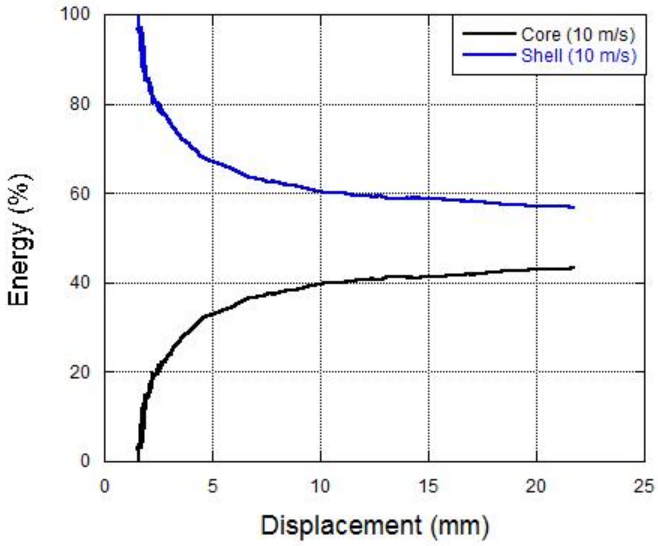

(a)

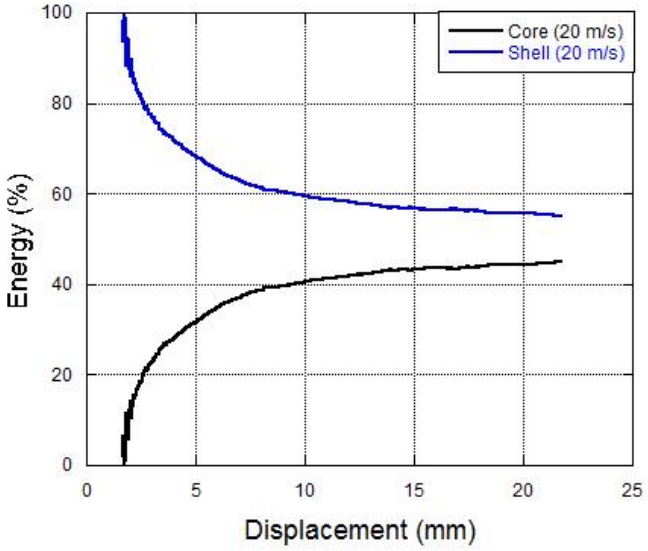

(b)

Figure 5.30. Energy partitions of inner core and outer shell structures at different impact velocities; (a) 10 m/s, (b) 20 m/s, (c) 50 m/s and (d) 100 m/s.

(cont. on next page)

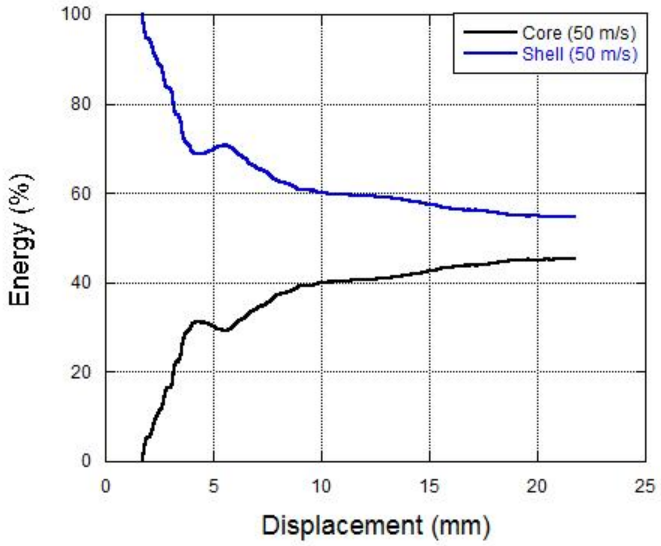

(c)

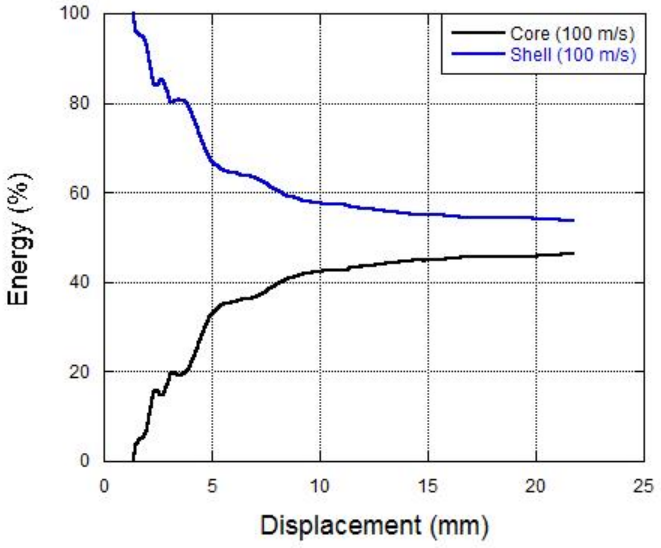

(d)

Figure 5.30. (cont.)

CHAPTER 6

CONCLUSION

In the scope of the study, a bio-inspired thin walled geometry consisting of an inner core and outer shell structures was designed and produced using AISI 304L stainless steel sheet metal. Deep drawing method was preferred as a forming process. Structures to be used as energy absorbers were exposed to both quasi-static and dynamic loads to determine the crushing behavior of the geometries. After the material characterization was accomplished at static and dynamic strain, stages of deep drawing were prepared numerically using commercial software LS-DYNA 971. Then, plastically formed numerical specimens were obtained. It was observed that the thickness distributions of these numerical specimens match to the experimental measurements. In the following steps, experimental and numerical studies were carried out to verify the material model constants which are significant for future works. Also, the strain rate sensitivity effect of the material was considered conducting experiments under dynamic loadings. The crushing behavior and energy absorbing performance of the empty and the foam-filled balanus were investigated at different strain rates and thus polyurethane foam material was also analyzed to clarify the confinement effect. Furthermore, the specific energy absorption capacities of the structures and the energy partitions between the constituents of the balanus were compared.

Briefly summarized experimental and numerical observations are listed below in detail:

- As can be seen from the thickness measurements of the components of balanus geometry, the thickness increases from the top of the specimens towards the bottom of the conical region and it is clear that the profile of thickness distribution stems from deep drawing process. Further, thickness distributions of the numerical specimens are close enough to the measurements of the experimental specimens.
- It was obviously demonstrated that the numerical specimens containing plastic stress and strain and having thickness distribution throughout the length must be considered to reach closer experimental results.

- Crushing experiments conducted at different strain rates was modelled numerically to verify the material model parameters and numerical studies proved that the results match up well with the experimental.
- Load-carrying capacity of the structures increased due to the strain hardening as a result of plastic deformation. Thus, energy absorbing capacity of the thin-walled structures improved.
- At the quasi-static deformation of the balanus, the global bending effect was observed in the last fold formation before the densification. This led to be observed little variation between tests in the last region of the curves.
- Between the static strain rate ranges, the deformation characteristics of the inner core, outer shell and balanus structures did not change significantly depending on the strain rate and the structures deformed in diamond mode resembling a triangular shape.
- When specific absorbed energy was considered it was easily seen that the energy absorption capacities of the outer shell and the balanus are more efficient than the inner core at quasi-static strain rate. However, the balanus is the most effective configuration among all structures in terms of energy absorption at dynamic strain rates.
- Drop weight experiments proved that the specific absorbed energy of the balanus improved with the increase in deformation rate while the SAE of the other two structures decreased.
- The outer shell confines the inner core during the deformation and thus improves the energy absorption performance of it. The force-deformation curve of the balanus was found above than the arithmetic sum of the force-deformation curves of the inner core and the outer shell due to the aforementioned confinement effect.
- There is only 50 percent increase of load carrying capacity in quasi-static compression tests of the balanus due to the interaction while the ratio ascended up to 150 percent at drop weight experiments
- During the quasi-static crushing tests of the foam filled balanus, only 50 percent increase of load carrying capacity resulted from the confinement effect of the polyurethane foam material. However, the foam improved

the load carrying performance of the balanus up to 80 percent increase in the drop weight tests. It is obviously seen from observations that the contribution of foam material enhanced depending on the increase in strain rate. The effectiveness of foam material became apparent as the deformation proceeded.

- Some variables that are difficult to measure in experiments were determined using numerical models and numerical studies proved that the interface pressure of the balanus increased under dynamic loadings.
- According to the results acquired from numerical models, the outer shell absorbed more energy than the inner core throughout the deformation history. Nevertheless, the difference of the energy absorbing performance between the constituents of the balanus decreased with the increase in the deformation rate.

REFERENCES

Abdewi, E. F., Sulaiman, S., Hamouda, A. M. S., & Mahdi, E. (2006). Effect of geometry on the crushing behaviour of laminated corrugated composite tubes. *Journal of Materials Processing Technology*, *172*(3), 394–399. https://doi.org/10.1016/j.jmatprotec.2005.07.017

Abdewi, E. F., Sulaiman, S., Hamouda, A. M. S., & Mahdi, E. (2008). Quasi-static axial and lateral crushing of radial corrugated composite tubes. *Thin-Walled Structures*, *46*(3), 320–332. https://doi.org/10.1016/j.tws.2007.07.018

Abosbaia, A. A. S., Mahdi, E., Hamouda, A. M. S., & Sahari, B. B. (2003). Quasi-static axial crushing of segmented and non-segmented composite tubes. *Composite Structures*, *60*(3), 327–343. https://doi.org/10.1016/S0263-8223(02)00341-0

Abosbaia, A. S., Mahdi, E., Hamouda, A. M. S., Sahari, B. B., & Mokhtar, A. S. (2005). Energy absorption capability of laterally loaded segmented composite tubes. *Composite Structures*, *70*(3), 356–373. https://doi.org/10.1016/j.compstruct.2004.08.039

Abramowicz, A., & Wierzbicki, T. (1983). On the crushing mechanics of thin-walled structures. *Journal of Applied Mechanics*, *50*(4), 727–34. https://doi.org/10.1353/lan.2015.0050

Abramowicz, W., & Wierzbicki, T. (1988). Axial Crushing of Foam-Filled Columns. *International Journal of Mechanical Sciences*, *30*(3), 263–271.

Ahmad, Z., & Thambiratnam, D. P. (2009a). Crushing response of foam-filled conical tubes under quasi-static axial loading. *Materials and Design*, *30*(7), 2393–2403. https://doi.org/10.1016/j.matdes.2008.10.017

Ahmad, Z., & Thambiratnam, D. P. (2009b). Dynamic computer simulation and energy absorption of foam-filled conical tubes under axial impact loading. *Computers and Structures*, *87*(3–4), 186–197. https://doi.org/10.1016/j.compstruc.2008.10.003

Alexander, J. M. (1960). An Approximate Analysis Of The Collapse Of Thin Cylindrical Shells Under Axial Loading. *The Quarterly Journal of Mechanics and Applied Mathematics*, *13*(1), 10–15. https://doi.org/10.1093/qjmam/13.1.10

Alkateb, M., Mahdi, E., Hamouda, A. M. S., & Hamdan, M. M. (2004). On the energy absorption capability of axially crushed composite elliptical cones. *Composite Structures*, *66*(1–4), 495–501. https://doi.org/10.1016/j.compstruct.2004.04.078

Azimi, M. B., & Asgari, M. (2016). A new bi-tubular conical – circular structure for improving crushing behavior under axial and oblique impacts. *International Journal of Mechanical Sciences*, *105*, 253–265. https://doi.org/10.1016/j.ijmecsci.2015.11.012

Babbage, J. M., & Mallick, P. K. (2005). Static axial crush performance of unfilled and foam-filled aluminum-composite hybrid tubes. *Composite Structures*, *70*(2), 177–184. https://doi.org/10.1016/j.compstruct.2004.08.021

Bar-cohen, Y. (2006). Biomimetics — using nature to inspire human innovation. *Bioinspiration & Biomimetics*, *1*, 1–12. https://doi.org/10.1088/1748-3182/1/1/P01

Buannic, N., Cartraud, P., & Quesnel, T. (2003). Homogenization of corrugated core sandwich panels. *Composite Structures*, *59*(3), 299–312. https://doi.org/10.1016/S0263-8223(02)00246-5

Côté, F., Deshpande, V. S., Fleck, N. A., & Evans, A. G. (2006). The compressive and shear responses of corrugated and diamond lattice materials. *International Journal of Solids and Structures*, *43*(20), 6220–6242. https://doi.org/10.1016/j.ijsolstr.2005.07.045

DiPaolo, B. P., & Tom, J. G. (2006). A study on an axial crush configuration response of thin-wall, steel box components: The quasi-static experiments. *International Journal of Solids and Structures*, *43*(25–26), 7752–7775. https://doi.org/10.1016/j.ijsolstr.2006.03.028

Easwara Prasad, G. L., & Gupta, N. K. (2006). An experimental study of deformation modes of domes and large-angled frusta at different rates of compression. *International Journal of Impact Engineering*, *32*(1–4), 400–415. https://doi.org/10.1016/j.ijimpeng.2004.12.001

Goel, M. D. (2015). Deformation, energy absorption and crushing behavior of single-, double- and multi-wall foam filled square and circular tubes. *Thin-Walled Structures*, *90*, 1–11. https://doi.org/10.1016/j.tws.2015.01.004

Goldsmith, W., & Sackmant, J. L. (1992). An experimental study of energy absorption in impact on sandwich plates. *International Journal of Impact Engineering*, *12*(2), 241–262.

Guden, M., Yüksel, S., Tasdemirci, A., & Tanoğlu, M. (2007). Effect of aluminum closed-cell foam filling on the quasi-static axial crush performance of glass fiber reinforced polyester composite and aluminum / composite hybrid tubes. *Composite Structures*, *81*, 480–490. https://doi.org/10.1016/j.compstruct.2006.09.005

Gupta, N. K., Mohamed Sheriff, N., & Velmurugan, R. (2008). Analysis of collapse behaviour of combined geometry metallic shells under axial impact. *International Journal of Crashworthiness*, *35*, 731–741. https://doi.org/10.1016/j.ijimpeng.2008.01.005

Gupta, N. K., Prasad, G. L. E., & Gupta, S. K. (1997). Plastic collapse of metallic conical frusta of large semi-apical angles. *International Journal of Crashworthiness*, *2*(4), 349–366. https://doi.org/10.1533/cras.1997.0054

Gupta, N. K., Sheriff, N. M., & Velmurugan, R. (2006). A study on buckling of thin conical frusta under axial loads. *Thin-Walled Structures*, *44*(9), 986–996. https://doi.org/10.1016/j.tws.2006.08.010

Gupta, N. K., & Venkatesh. (2007). Experimental and numerical studies of impact axial compression of thin-walled conical shells. *International Journal of Impact Engineering*, *34*(4), 708–720. https://doi.org/10.1016/j.ijimpeng.2006.02.008

Gupta, P. K. (2017). A study on analysis of collapse of metallic shells having dome-cone shape. *Procedia Engineering*, *173*, 1708–1715. https://doi.org/10.1016/j.proeng.2016.12.202

Hanssen, A. G., Enstock, L., & Langseth, M. (2002). Close-range blast loading of aluminium foam panels. *International Journal of Impact Engineering*, *27*, 593–618. https://doi.org/10.1007/978-1-4020-9404-0_18

Hou, T., Pearce, G. M. K., Prusty, B. G., Kelly, D. W., & Thomson, R. S. (2015). Pressurised composite tubes as variable load energy absorbers. *Composite Structures*, *120*, 346–357. https://doi.org/10.1016/j.compstruct.2014.09.060

Hou, W., Zhu, F., Lu, G., & Fang, D. N. (2010). Ballistic impact experiments of metallic sandwich panels with aluminium foam core. *International Journal of Impact Engineering*, *37*(10), 1045–1055. https://doi.org/10.1016/j.ijimpeng.2010.03.006

Kashani, M. H., Alavijeh, H. S., Akbarshahi, H., & Shakeri, M. (2013). Bitubular square tubes with different arrangements under quasi-static axial compression loading. *Materials and Design*, *51*, 1095–1103.

Kathiresan, M., & Manisekar, K. (2016). Axial crush behaviours and energy absorption characteristics of aluminium and E-glass/epoxy over-wrapped aluminium conical frusta under low velocity impact loading. *Composite Structures*, *136*, 86–100. https://doi.org/10.1016/j.compstruct.2015.09.052

Kathiresan, M., Manisekar, K., & Manikandan, V. (2012). Performance analysis of fibre metal laminated thin conical frusta under axial compression. *Composite Structures*, *94*(12), 3510–3519. https://doi.org/10.1016/j.compstruct.2012.05.026

Kathiresan, M., Manisekar, K., & Manikandan, V. (2014). Crashworthiness analysis of glass fibre/epoxy laminated thin walled composite conical frusta under axial compression. *Composite Structures*, *108*(1), 584–599. https://doi.org/10.1016/j.compstruct.2013.09.060

Kemp, M. (2006). *Leonardo Da Vinci: The Marvellous Works of Nature and Man*. Oxford: Oxford University Press, UK.

Kilicaslan, C., Guden, M., Odaci, I. K., & Tasdmirci, A. (2014). Experimental and numerical studies on the quasi-static and dynamic crushing responses of multi-layer trapezoidal aluminum corrugated sandwiches. *Thin-Walled Structures*, *78*, 70–78. https://doi.org/10.1016/j.tws.2014.01.017

Lau, S. T. W., Said, M. R., & Yaakob, M. Y. (2012). On the effect of geometrical designs and failure modes in composite axial crushing: A literature review. *Composite Structures*, *94*(3), 803–812. https://doi.org/10.1016/j.compstruct.2011.09.013

Lepora, N. F., Verschure, P., & Prescott, T. J. (2013). The state of the art in biomimetics. *Bioinspiration & Biomimetics*, *13001*. https://doi.org/10.1088/1748-3182/8/1/013001

Li, G. (2006). Experimental study of FRP confined concrete cylinders. *Engineering Structures*, *28*(7), 1001–1008. https://doi.org/10.1016/j.engstruct.2005.11.006

Li, G. (2007). Experimental study of hybrid composite cylinders. *Composite Structures*, *78*(2), 170–181. https://doi.org/10.1016/j.compstruct.2005.08.028

Li, G., Maricherla, D., Singh, K., Pang, S. S., & John, M. (2006). Effect of fiber orientation on the structural behavior of FRP wrapped concrete cylinders. *Composite Structures*, *74*(4), 475–483. https://doi.org/10.1016/j.compstruct.2005.05.001

Mahdi, E., Hamouda, A. M. S., Sahari, B. B., & Khalid, Y. A. (2003). Experimental quasi-static axial crushing of cone-tube-cone composite system. *Composites Part B: Engineering*, *34*(3), 285–302. https://doi.org/10.1016/S1359-8368(02)00102-6

Mahdi, E. S., & El Kadi, H. (2008). Crushing behavior of laterally compressed composite elliptical tubes: Experiments and predictions using artificial neural networks. *Composite Structures*, *83*(4), 399–412. https://doi.org/10.1016/j.compstruct.2007.05.009

Mamalis, A. ., Robinson, M., Manolakos, D. E., Demosthenous, G. A., Ioannidis, M. B., & Carruthers, J. (1997). Crashworthy capability of composite material structures. *Composite Structures*, *37*(2), 109–134. https://doi.org/10.1016/S0263-8223(97)80005-0

Mamalis, A. G., Manolakos, D. E., Ioannidis, M. B., & Papapostolou, D. P. (2004). Crashworthy characteristics of axially statically compressed thin-walled square CFRP composite tubes: Experimental. *Composite Structures*, *63*(3–4), 347–360. https://doi.org/10.1016/S0263-8223(03)00183-1

Mamalis, A. G., Manolakos, D. E., Ioannidis, M. B., & Papapostolou, D. P. (2005). On the response of thin-walled CFRP composite tubular components subjected to static and dynamic axial compressive loading: Experimental. *Composite Structures*, *69*(4), 407–420. https://doi.org/10.1016/j.compstruct.2004.07.021

Mamalis, A. G., Manolakos, D. E., Ioannidis, M. B., & Papapostolou, D. P. (2006). The static and dynamic axial collapse of CFRP square tubes: Finite element modelling. *Composite Structures*, *74*(2), 213–225. https://doi.org/10.1016/j.compstruct.2005.04.006

Mckown, S., Shen, Y., Brookes, W. K., Sutcliffe, C. J., Cantwell, W. J., & Langdon, G. S. (2008). The quasi-static and blast loading response of lattice structures. *International Journal of Impact Engineering*, *35*, 795–810. https://doi.org/10.1016/j.ijimpeng.2007.10.005

Milan, R., Viktor, K., Sergii, B., & Vít, S. (2014). Development of composite energy absorber. *Procedia Engineering*, *96*, 392–399. https://doi.org/10.1016/j.proeng.2014.12.108

Mirfendereski, L., Salimi, M., & Ziaei-Rad, S. (2008). Parametric study and numerical analysis of empty and foam-filled thin-walled tubes under static and dynamic loadings. *International Journal of Mechanical Sciences*, *50*(6), 1042–1057. https://doi.org/10.1016/j.ijmecsci.2008.02.007

Mohamed Sheriff, N., Gupta, N. K., Velmurugan, R., & Shanmugapriyan, N. (2008). Optimization of thin conical frusta for impact energy absorption. *Thin-Walled Structures*, *46*(6), 653–666. https://doi.org/10.1016/j.tws.2007.12.001

Moriarty, K., & Goldsmith, W. (1993). Dynamic energy absorption characteristics of sandwich shells. *International Journal of Impact Engineering*, *13*(2), 293–317.

Nia, A. A., & Parsapour, M. (2014). Thin-Walled Structures Comparative analysis of energy absorption capacity of simple and multi-cell thin-walled tubes with triangular , square , hexagonal and octagonal sections. *Thin Walled Structures*, *74*, 155–165. https://doi.org/10.1016/j.tws.2013.10.005

Palanivelu, S., Paepegem, W. Van, Degrieck, J., Vantomme, J., Kakogiannis, D., Ackeren, J. Van, … Wastiels, J. (2011). Crushing and energy absorption performance of different geometrical shapes of small-scale glass/polyester composite tubes under quasi-static loading conditions. *Composite Structures*, *93*(2), 992–1007. https://doi.org/10.1016/j.compstruct.2010.06.021

Parvin, A., & Jamwal, A. S. (2005). Effects of wrap thickness and ply configuration on composite-confined concrete cylinders. *Composite Structures*, *67*(4), 437–442. https://doi.org/10.1016/j.compstruct.2004.02.002

Pope, E. C. (1945). AUSTRALIAN MUSEUM. *Records of the Australian Museum*, *21*(6), 21, 351–372. https://doi.org/10.3853/j.0067-1975.21.1945.550

Rajaneesh, A., Sridhar, I., & Rajendran, S. (2014). Relative performance of metal and polymeric foam sandwich plates under low velocity impact. *International Journal of Impact Engineering*, *65*, 126–136. https://doi.org/10.1016/j.ijimpeng.2013.11.012

Raman, S., & Kumar, R. (2011). Construction and nanomechanical properties of the exoskeleton of the barnacle , Amphibalanus reticulatus. *Journal of Structural Biology*, *176*(3), 360–369. https://doi.org/10.1016/j.jsb.2011.08.015

Rathbun, H. J., Radford, D. D., Xue, Z., He, M. Y., Yang, J., Deshpande, V., … Evans, A. G. (2006). Performance of metallic honeycomb-core sandwich beams under shock loading. *International Journal of Solids and Structureseranational Journal of Sol*, *43*, 1746–1763. https://doi.org/10.1016/j.ijsolstr.2005.06.079

Reid, S. R., & Reddy, T. Y. (1986a). Axial crushing of foam-filled tapered sheet metal tubes. *International Journal of Mechanical Sciences*, *28*, 643–656.

Reid, S. R., & Reddy, T. Y. (1986b). Static and dynamic crushing of tapered sheet metal tubes of rectangular cross-section. *International Journal of Mechanical Sciences*, *28*(9), 623–637. https://doi.org/10.1016/0020-7403(86)90077-9

Reid, S. R., Reddy, T. Y., & Gray, M. D. (1986). Static and dynamic axial crushing of foam-filled sheet metal tubes. *International Journal of Mechanical Sciences*, *28*(5), 295–322. https://doi.org/10.1016/0020-7403(86)90010-X

Reuter, C., Sauerland, K.-H., & Tröster, T. (2017). Experimental and numerical crushing analysis of circular CFRP tubes under axial impact loading. *Composite Structures*, *174*, 33–44. https://doi.org/10.1016/j.compstruct.2017.04.052

Saleh, M. A., Mahdi, E., Hamouda, A. M. S., & Khalid, Y. A. (2004). Crushing behaviour of composite hemispherical shells subjected to quasi-static axial compressive load. *Composite Structures*, *66*(1–4), 487–493. https://doi.org/10.1016/j.compstruct.2004.04.073

Smith, M., Cantwell, W., Guan, Z., Tsopanos, S., Theobald, M., Nurick, G., & Langdon, G. (2011). The quasi-static and blast response of steel lattice structures. *Journal of Sandwich Structures and Materials*, *13*(4), 479–501. https://doi.org/10.1177/1099636210388983

Tasdemirci, A., Sahin, S., Kara, A., & Turan, K. (2015). Thin-Walled Structures Crushing and energy absorption characteristics of combined geometry shells at quasi-static and dynamic strain rates : Experimental and numerical study. *Thin Walled Structures*, *86*, 83–93. https://doi.org/10.1016/j.tws.2014.09.020

Vinson, J. R. (1999). *The Behavior of Sandwich Structures of Isotropic and Composite Materials*. Technomic Publishing Company, Inc. https://doi.org/10.1016/S0029-8018(01)00013-0

Wang, Y., Feng, J., Wu, J., & Hu, D. (2016). Effects of fiber orientation and wall thickness on energy absorption characteristics of carbon-reinforced composite tubes under different loading conditions. *Composite Structures*, *153*, 356–368. https://doi.org/10.1016/j.compstruct.2016.06.033

Xiang, J., & Du, J. (2017). Energy absorption characteristics of bio-inspired honeycomb structure under axial impact loading. *Materials Science and Engineering A*, *696*, 283–289.

Yokozeki, T., Takeda, S. ichi, Ogasawara, T., & Ishikawa, T. (2006). Mechanical properties of corrugated composites for candidate materials of flexible wing structures. *Composites Part A: Applied Science and Manufacturing*, *37*(10), 1578–1586. https://doi.org/10.1016/j.compositesa.2005.10.015

Zarei, H. R., & Kröger, M. (2008). Optimization of the foam-filled aluminum tubes for crush box application. *Thin Walled Structures*, *46*, 214–221. https://doi.org/10.1016/j.tws.2007.07.016

Zhao, H., Elnasri, I., & Girard, Y. (2007). Perforation of aluminium foam core sandwich panels under impact loading-An experimental study. *International Journal of Impact Engineering*, *34*(7), 1246–1257. https://doi.org/10.1016/j.ijimpeng.2006.06.011

Zhu, G., Sun, G., Liu, Q., Li, G., & Li, Q. (2017). On Crushing Characteristics of Different Configurations of Metal-Composites Hybrid Tubes. *Composite Structures*, *175*, 58–69. https://doi.org/10.1016/j.compstruct.2017.04.072